

Investigation of single-photon emission from quantum dots in semiconductor waveguides under non-resonant and resonant excitation

Citation for published version (APA):

Fattahpoor, S. (2014). *Investigation of single-photon emission from quantum dots in semiconductor waveguides under non-resonant and resonant excitation*. [Phd Thesis 1 (Research TU/e / Graduation TU/e), Applied Physics and Science Education]. Technische Universiteit Eindhoven. <https://doi.org/10.6100/IR776342>

DOI:

[10.6100/IR776342](https://doi.org/10.6100/IR776342)

Document status and date:

Published: 01/01/2014

Document Version:

Publisher's PDF, also known as Version of Record (includes final page, issue and volume numbers)

Please check the document version of this publication:

- A submitted manuscript is the version of the article upon submission and before peer-review. There can be important differences between the submitted version and the official published version of record. People interested in the research are advised to contact the author for the final version of the publication, or visit the DOI to the publisher's website.
- The final author version and the galley proof are versions of the publication after peer review.
- The final published version features the final layout of the paper including the volume, issue and page numbers.

[Link to publication](#)

General rights

Copyright and moral rights for the publications made accessible in the public portal are retained by the authors and/or other copyright owners and it is a condition of accessing publications that users recognise and abide by the legal requirements associated with these rights.

- Users may download and print one copy of any publication from the public portal for the purpose of private study or research.
- You may not further distribute the material or use it for any profit-making activity or commercial gain
- You may freely distribute the URL identifying the publication in the public portal.

If the publication is distributed under the terms of Article 25fa of the Dutch Copyright Act, indicated by the "Taverne" license above, please follow below link for the End User Agreement:

www.tue.nl/taverne

Take down policy

If you believe that this document breaches copyright please contact us at:

openaccess@tue.nl

providing details and we will investigate your claim.

Investigation of Single-Photon Emission from Quantum Dots in Semiconductor Waveguides under Non-Resonant and Resonant Excitation

PROEFSCHRIFT

ter verkrijging van de graad van doctor aan de
Technische Universiteit Eindhoven, op gezag van de rector magnificus,
prof.dr.ir. C.J. van Duijn, voor een commissie aangewezen door
het College voor Promoties in het openbaar te verdedigen
op dinsdag 16 september 2014 om 16.00 uur

door

Sartoon Fattah poor

geboren te Sanandaj, Iran

Dit proefschrift is goedgekeurd door de promotoren en de samenstelling van de promotiecommissie is als volgt:

voorzitter: prof.dr.ir. G.M.W. Kroesen

1e promotor: prof.dr. A. Fiore

2e promotor: prof.dr.ir. M.K. Smit

leden: prof.dr. M. Kamp (University of Würzburg)

 dr. G. Şek (Wrocław University of Technology)

 dr. J.J.G.M. van der Tol

 Prof.dr. J. Gómez Rivas

Investigation of Single-Photon Emission from Quantum Dots in Semiconductor Waveguides under Non-Resonant and Resonant Excitation

Sartoon Fattah poor

A catalogue record is available from the Eindhoven University of Technology Library.

ISBN: 978-90-386-3661-0

Investigation of Single-Photon Emission from Quantum Dots in Semiconductor Waveguides under Non-Resonant and Resonant Excitation,

by Sartoon Fattah poor

The work described in this thesis has been carried out in the group of Photonics and Semiconductor Nanophysics, at the Department of Applied Physics of the Eindhoven University of Technology, The Netherlands.

Printed by Ipskamp drukkers.

Contents

Abstract	1
1 Introduction	3
1.1 Photonic quantum information	4
1.1.1 Quantum computing	4
1.1.2 Quantum communication	5
1.1.3 Quantum simulation	6
1.2 Quantum photonic integrated circuits	6
1.3 Quantum dots	8
1.4 Photonic crystals	9
1.5 Cavity quantum electrodynamics	13
1.5.1 Jaynes-Cummings model	13
1.5.2 Coupling to the environment	13
1.5.3 Weak and strong coupling regimes of CQED	15
1.6 Quantum information processing using optical nonlinearities .	17
1.7 Scope and outline of this thesis	18
2 Experimental Methods	21
2.1 Fabrication	21
2.1.1 Material growth	22
2.1.2 Thin film deposition	22
2.1.3 Electron-beam lithography	23
2.1.4 Etching methods	24
2.1.5 Process flow	30
2.2 Measurement setups	31
2.2.1 Micro photoluminescence	32
2.2.2 Waveguide micro photoluminescence	32
2.2.3 Waveguide probe station	32
2.2.4 Superconducting single photon detector	33

2.2.5	Time-resolved photoluminescence and anti-bunching measurements	34
3	Theoretical Investigation of Single-photon Nonlinear Phenomena	37
3.1	Introduction	37
3.2	Dipole-induced reflection	38
3.2.1	Numerical analysis	39
3.2.2	Feasibility study	43
3.3	Stimulated emission	45
3.3.1	Numerical analysis	46
3.4	Conclusion	49
4	Efficient Coupling of Light into a Photonic Crystal	51
4.1	Design of photonic crystal waveguide-nanobeam interface for efficient coupling of light	51
4.2	Design of the photonic crystal cavity as an on-chip filter	52
4.3	Anti-reflection coating for suppression of the reflection at ridge-waveguide cleaved end facets	58
4.4	Grating couplers for efficient coupling of light from the photonic crystal cavity to the top	61
4.5	Conclusion	63
5	Single-Photon Transmission through A Coupled Ridge waveguide-Photonic crystal Cavity System	65
5.1	Funnelling single photons into ridge-waveguide photonic integrated circuits	65
5.2	Progress toward the demonstration of dipole-induced transparency	75
5.3	Conclusion	76
6	Resonance Fluorescence of the Single Quantum Dots inside Semiconductor Ridge Waveguides	79
6.1	Introduction	79
6.2	Polarization properties of the emission of single InAs/GaAs quantum dots	80
6.2.1	Polarization of the emission of single InAs/GaAs quantum dots	81
6.2.2	Fine-structure splitting in single quantum dots	82

6.3	Observation of the resonance fluorescence of single InAs/GaAs quantum dots in a ridge waveguide	84
6.4	Conclusion	90
7	Conclusions and Outlook	91
	Bibliography	95
	Summary	115
	Acknowledgements	117
	List of Publications	121
	Curriculum Vitae	123

Abstract

Single photons are one of the most appealing candidates for the implementation of quantum information due to their low decoherence. Since scaling up of the quantum information systems to tens of qubits requires a large number of optical elements, the integrated generation, control and transport of single photons has emerged as a high priority in this field of research. Quantum Dots (QDs) are nanometer-sized semiconductor heterostructures that show atomic-like behavior making them suitable for single photon generation. These heterostructures can be grown embedded in III-V semiconductor waveguides, and can therefore be used in integrated single-photon sources. This thesis deals with different aspects of integrated single-photon sources based on QDs. In order to control the single photons generated by QDs, they are integrated with photonic crystals (PhCs) which are created by etching a periodic pattern of holes on a suspended slab of semiconductor wafer. The transport of single photons created by QDs in a PhC to other parts of the circuit can be achieved by coupling them to low-loss semiconductor ridge waveguides (RWGs). A difficulty here arises because of the mode mismatch between the narrow and suspended PhC waveguide (PhCWG) and the wide ridge waveguide, which makes the coupling between them very inefficient. In order to overcome this difficulty, in this thesis a novel design based on the adiabatic transition of electromagnetic mode from the PhCWG to the RWG has been demonstrated and 70% coupling efficiency between PhCWG and RWG has been achieved enabling a high 3.5 MHz single photon funneling rate from the QD to the RWG. The properties of emitted single photons depend on the excitation method of the emitter. Resonant pumping of QDs al-

lows background-free and bright emission of single photons and the direct and coherent manipulation of them which is vital for the realization of solid-state qubits. The difficulty of extracting resonance fluorescence in a solid-state system such as a QD comes from the strong scattering of resonant laser pump which dominates the weak single-photon signal of the QD. In this thesis, by exploiting the polarization properties of the light emitted by single QDs integrated in a semiconductor RWG a novel design has been demonstrated which allows filtering of the scattered resonant laser by cross-polarization and detecting resonant emission of single QDs. Finally the two phenomena of dipole induced reflection and stimulated emission which can be used to realize optical quantum gates and single photon transistors have been theoretically studied. The feasibility of their observation in the current state-of-the-art growth and fabrication facility has been investigated and necessary technology for that purpose has been developed. The results obtained in this thesis provide the possibility of resonant generation and coherent manipulation, control and transport of single photons on a semiconductor chip which is a step toward realization of a scalable and fully functional quantum photonic integrated circuit for the future quantum information and quantum computation applications.

Today we live in the information age of the human history which has been created by the digital revolution in the beginning of 50s. The invention of transistors by Bardeen, Brittain and Shockley in 1947 (who received the Nobel prize in physics in 1956) started this revolution, which later came to its turning point with the invention of integrated circuits by Kilby (who received the Nobel prize in physics in 2000) in the late 50s. After this invention, the dimensions of the transistors started to shrink at a very high rate. It is stated by Moore's law that the number of electronic components integrated in a chip doubles every 18 months. This trend has been continued since Moore introduced this law for the first time in 1965 [1]. The corresponding increase in computing power creates a high demand for ever increasing bandwidth for data transfer. The invention of the optical fiber by Kao (Nobel prize in physics in 2009) started the usage of optical signals for data transport. Optical fibers are usually made of silica and operate in the near infrared range of the electromagnetic spectrum. They permit the transmission of the data over larger distances with higher bandwidth, very low loss and high immunity to electromagnetic interference.

The drive for using optical signals in place of the electrical ones created a demand for devices capable of generating and processing of light on a chip. This generated the idea of creating a photonic integrated circuits (PIC) [2]. In these PICs, analogous of the electrical integrated circuits, optical signals are generated and processed with the help of dielectric waveguides [3]. Several functionalities including the arrayed waveguide grating [4] which acts as an optical multiplexer and the externally modulated laser, which combines a distributed feedback laser diode with an electro-absorption modulator on a single InP-based chip [5], have

been demonstrated in PICs.

After the recent development in the realization of the PICs, a considerable amount of attention has been paid to extend the functionality of these circuits to the single photon level where the behaviour of the light at the level of the individual quantum (photon) becomes noticeable. In this regime photons obey the rules of quantum mechanics and their properties can be exploited for the implementation of the quantum information systems [6] which will be reviewed quickly in the following sections before considering the structure of the quantum photonic integrated circuit (QPIC) in more detail.

1.1 Photonic quantum information

The concept of the photon as the quantum of light was developed by Einstein and Planck for explaining the black body spectrum and the photoelectric effect [7]. The later experiments, most notably scattering of single photons by electrons performed by Compton (who received the Nobel prize in 1927) and the measurement of the charge of a single electron performed by Millikan (who received the Nobel prize in 1923) proved that the energy in the electromagnetic field is quantized. In 1926 physicist F. Wolfers and chemist G. N. Lewis used the term "photon" for the first time to name this particle and after that this term was adopted extensively among the scientific community [8].

Photons along with atomic and superconducting systems are one of the candidates for implementation of quantum information protocols. They are considered as one of the most practical candidates due to their low decoherence and fast transmission [9]. These properties have made them suitable for the applications described in the following sections.

1.1.1 Quantum computing

A quantum computer is a device that makes use of the laws of quantum mechanics such as superposition and entanglement to carry out a computational task. Contrary to the classical computers based on transistors, data is encoded in a superposition of 0 and 1 (called qubit) and not in a well-defined state as classical bits. This property gives the quantum computers a powerful advantage due to their inherent parallelism for solving certain type of problems (for example the algorithm of the factorization of a number), where the quantum computer performs exponentially faster than its classical counterpart [10].

There are several proposed platforms for the realization of quantum computers namely solid-state spin systems, trapped ions and atoms, photons and superconducting qubits. It is still an open question which system is the best platform for quantum computation implementation [11]. Photons are very attractive candidate for fast and secure transfer of the information but making a quantum gate with photons is much harder since they don't interact with each other. Later in this chapter the proposed approaches to realize this interaction will be reviewed. Since the other systems provide a better platform for the processing of the qubits, a combination of the storage and processing of the qubits in these platforms and the transmission of the data through photons as a quantum network has been recently proposed [12].

1.1.2 Quantum communication

Quantum communication is the use of quantum mechanics for transferring qubits between two separate locations. One of the most important types of quantum communication is quantum key distribution (QKD) which consists of the process of sharing a secret key between two parties (usually indicated as Alice and Bob) so that an eavesdropper (usually called Eve) can not learn this key even if she can eavesdrop all the communication between Alice and Bob. This is guaranteed by the laws of quantum mechanics (the only restriction is that Eve can not impersonate Alice and Bob). If Alice sends quantum bits to Bob, an eavesdropping attempt by Eve will produce a change in the qubits state that Alice and Bob will notice. This is due to the fact that any measurement, according to quantum mechanics, projects the quantum state which is being measured into the measurement basis. The idea of QKD was first proposed by S. Wiesner in early 70s [13] and a decade later C. Bennett and G. Brassard proposed a famous protocol for secure communication known as BB84 [14].

Practical implementations of QKD (where the 0 and 1 states are encoded into polarization or other degrees of freedom of the photon) faces several challenges including efficient single-photon sources and detectors in the telecom wavelengths which limit the distance and bit exchange rate of QKD protocols [15]. Also the need to realize the so-called quantum repeaters for distribution of the signal through the lossy channel creates more practical restrictions for QKD implementation [16]. Recently QKD over a distance of 300 Km has been demonstrated on an optical fiber system [17].

1.1.3 Quantum simulation

The idea of quantum simulation was first proposed by Feynman [18]. He suggested the use of a control quantum system that can reproduce the behaviour of the original quantum system. In this way one can overcome the inability of the classical computers to simulate the behavior of quantum systems, since they can't solve problems involving superposition and entanglement efficiently. To date quantum simulators have been realized in a variety of platforms including trapped ions, atoms, superconducting circuits and photons and are expected to outperform classical computers very quickly [19].

1.2 Quantum photonic integrated circuits

Implementing quantum information protocols with free-space optics faces the problem of loss and tremendous complexity with an increased number of optical elements. One proposed solution to this problem is the quantum photonic integrated circuit (QPIC) [6]. In this platform single photons are generated, processed, transported and detected on a chip. Recently quantum optics experiments with photons have been conducted on an integrated platform based on silica. Although this platform creates a suitable framework for coupling low-loss silica waveguides to silica fibers at telecom wavelengths [20, 21, 22], this approach does not include the sources and detectors on the chip. In order to have a fully functional QPIC all the aforementioned components should be integrated on a chip. This makes a direct bandgap III-V material like InP or GaAs a very suitable candidate since they can emit on-demand single photons on-chip at telecom wavelengths (1300 and 1550 nm) [23, 24, 25, 26]. In this work our focus is on the GaAs technology for generation of single photons.

A sketch of a QIPC can be seen in figure 1.1 where different parts of the circuit are being depicted.

In this sketch several types of components are distinguishable:

- Single-photon sources generate on-demand single photons. This is usually achieved when an atom brought to its excited-state decays to the ground-state by a process called spontaneous emission. Single atoms are difficult to integrate into semiconductor materials, therefore semiconductor heterostructures are used instead which show atomic-like behaviour (known as quantum dots) [27] and can be epitaxially grown and embedded into III-V wafers.
- Cavities enhance the emission of the single-photon emitter and facili-

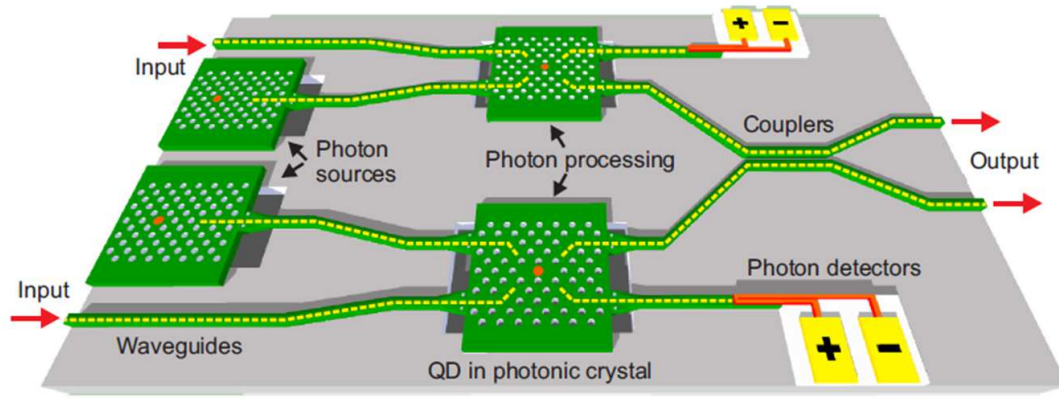


Figure 1.1: Sketch of a quantum photonic integrated circuit, where single photons can be generated by QDs inside the PhC cavities and the emission can be transported by RWGs toward other parts of the circuit or the on-chip detector. Design by Dr. R. Johne.

tate its coupling to the waveguides and couplers which are used to transport and split the light on the chip. In- and output couplers are used for connection to the outside by coupling to a fiber.

- Single-photon processors are devices made of a cavity and a single QD where the effective interaction between individual single photons is realized by means of exploiting inherent nonlinearities of the system. An example of such nonlinear devices is a single-photon switch where the presence of a single photon switches the transmission of another one through the system. Two of such nonlinear phenomena will be reviewed in this chapter and have been investigated theoretically in detail in this thesis in chapter 3.

- Single photon detectors are used to detect single photons by means of converting a single photon pulse to an electrical pulse. Recently fast and efficient single photon detectors have been made with superconducting nanowires biased close to their superconducting critical current [28]. Upon the absorption of a single photon a hot-spot is formed and the superconductivity breaks down for a few tens of picoseconds. The increased resistance of the detector area creates a measurable electric pulse. Recently waveguide-based single photon detectors

have been demonstrated by three groups [29, 30, 31].

In the next section of this chapter we introduce the quantum dots which are single-photon emitters in our circuit and of fundamental importance for their performance.

1.3 Quantum dots

With advances in modern semiconductor growth techniques such as molecular beam epitaxy (MBE), precise deposition of semiconductor material layers is now possible, which paves the way for fabrication of modern nano-scale devices. When semiconductor layers of different bandgap are grown on top of each other a heterostructure is formed. The development of semiconductor heterostructures has led to a revolution in semiconductor industry and started a myriad of inventions like SOAs, LEDs and lasers. The Nobel prize in physics in 2000 was awarded to Z. I. Alferov and H. Kroemer for the development of these structures.

When a semiconductor material layer is embedded in a semiconductor with a higher bandgap a potential well for the charge carriers is formed. If the dimension of the well is smaller than de Broglie wavelength of the charge carriers, they are spatially confined in the potential well and quantum mechanical effects start to govern the physics of the structure. In this situation the energy of the system is quantized and according to the dimensionality of the confinement different heterostructures can form (for 1D, 2D and 3D confinements, quantum wells, quantum wires and quantum dots, respectively). In the case of 3D confinement the density of the states will show a delta function behaviour similar to an atom.

By depositing layers of lattice-mismatched semiconductor materials on top of each other it is possible to create QDs embedded in the semiconductor material layer, which is known as Stranski-Krastanov method (for QDs in this work a layer of InAs is deposited on top of GaAs). The lattice mismatch creates strain which leads to the formation of self-assembled 3D islands as shown in figure 1.2a.

As it is indicated in figure 1.2b, an electron can be excited and brought to the conduction band leaving an available state in the valence band. It is usually convenient to consider the valence band as having a hole instead of missing an electron. The interaction of an electron and a hole creates a bound state which is called an exciton. Generation of an electron-hole pair can be achieved electrically or optically (for example by pumping the electron by an off-resonant

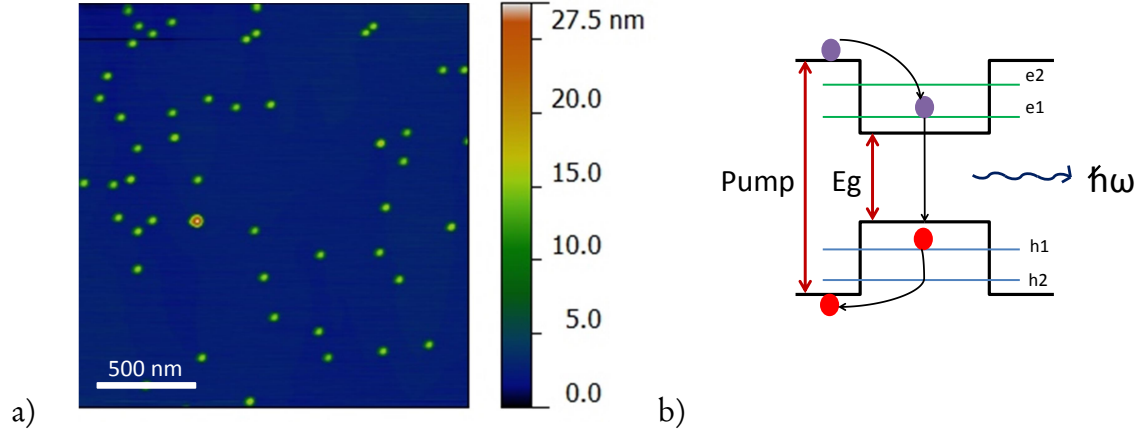


Figure 1.2: (a) Atomic Force Microscope image of InAs QDs grown on GaAs (measurement performed by T. Xia). (b) Typical energy diagram of the QD heterostructures, where the pumped electron recombines with the hole in valance band and emits a photon with a frequency equal to the bandgap frequency.

laser to a higher energy state which decays quickly to the excited state). In this picture a QD shows sharp atomic-like emission lines when an electron from the conduction band recombines with a hole in the valence band and emits a single photon (with the same frequency as the energy of the exciton). The observation of sharp atomic-like (single QD) lines (with linewidth $< 200 \mu\text{eV}$) can be achieved only at low temperatures ($< 50 \text{ K}$) since at higher temperatures the linewidth broadening of the QDs due to their increased interaction rates with the phonons, makes the observation of the sharp QD lines impossible [32].

The density, linewidth and the wavelength of the QDs can be controlled by the growth condition. In this work InAs/GaAs QDs with a density of $\sim 10 \mu\text{m}^{-2}$, low temperature emission wavelengths between 1200-1300 nm and linewidths between 20-180 μeV have been used.

1.4 Photonic crystals

Photonic crystals (PhC) are structures where the refractive index of the dielectric is modulated periodically. The term "photonic crystal" was first introduced

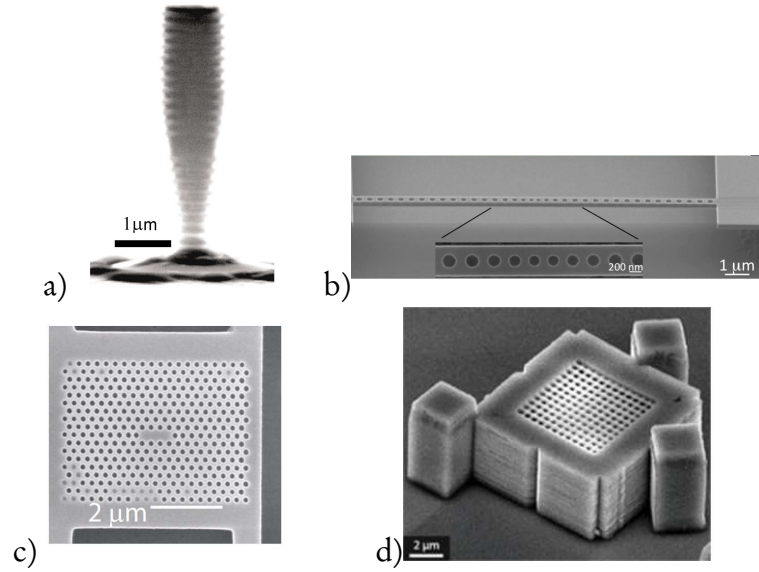


Figure 1.3: Scanning Electron Microscope images of photonic crystals fabricated in 1, 2 and 3D. (a) Bragg mirror inside a micropillar [42], (b) Nanobeam cavity [43], (c) triangular PhC in InP slab [44] and (d) GaAs woodpile structure [45].

by Yablonovitch (it is also called photonic bandgap material) to be used for inhibition of spontaneous emission in solid state systems [33]. In this structure interference effects create a range of forbidden wavelengths where the light cannot propagate in the structure. The concept is analogous to the semiconductor energy bandgap where the periodic electronic potential creates an energy bandgap where electronic states cannot exist. The refractive index periodicity can exist in 1, 2 and 3 dimensions (as shown in figure 1.3). The 3D PhC is very demanding to fabricate and was first realized by the Yablonovitch group [34]. After the first demonstration of the 2D PhC slab [35], a variety of PhC devices such as cavities, splitters, waveguides and filters have been realized with them [36, 37, 38, 39, 40, 41].

In order to investigate the optical properties of PhCs we start from solving Maxwell equations for an environment without any loss and any sources (no isolated charges and currents): [46]

$$\nabla \cdot \mathbf{H}(\mathbf{r}, t) = 0 \qquad \nabla \times \mathbf{E}(\mathbf{r}, t) + \mu_0 \frac{\partial \mathbf{H}}{\partial t} = 0 \qquad (1.1)$$

$$\nabla \cdot [\epsilon(\mathbf{r})\mathbf{E}(\mathbf{r}, t)] = 0 \quad \nabla \times \mathbf{H}(\mathbf{r}, t) - \epsilon_0 \epsilon(\mathbf{r}) \frac{\partial \mathbf{E}}{\partial t} = 0 \quad (1.2)$$

where \mathbf{H} and \mathbf{E} are magnetic field strength and electric field vectors, ϵ , ϵ_0 and μ_0 indicate relative permittivity of the material, permittivity of the vacuum and magnetic permeability of the vacuum, respectively. Relative magnetic permeability has been considered to be unity (non-magnetic material). These equations can describe the propagation of the light in the medium. If we assume a harmonic solution, then our fields can be written as the product of a spatial function (which is our mode profile) and a harmonic time-dependent component:

$$\mathbf{E}(\mathbf{r}, t) = \mathbf{E}(\mathbf{r})e^{i\omega t} \quad (1.3)$$

$$\mathbf{H}(\mathbf{r}, t) = \mathbf{H}(\mathbf{r})e^{i\omega t} \quad (1.4)$$

With this assumption we obtain an eigenvalue equation for $\mathbf{H}(\mathbf{r}, t)$ known as master equation:

$$\nabla \times \left(\frac{1}{\epsilon(\mathbf{r})} \nabla \times \mathbf{H}(\mathbf{r}, t) \right) = \left(\frac{\omega}{c} \right)^2 \mathbf{H}(\mathbf{r}) \quad (1.5)$$

The linearity of the operator acting on $\mathbf{H}(\mathbf{r}, t)$ on the left hand side of the equation guarantees that any linear combination of the solutions of the equation is also a solution of this equation.

If we introduce a periodic profile of the refractive index

$$\epsilon(\mathbf{r}) = \epsilon(\mathbf{r} + \mathbf{R}_i), \quad (1.6)$$

where \mathbf{R}_i is the lattice vector of the crystal we can apply the Bloch theorem and obtain solutions of the form [47]:

$$\mathbf{H}_{\mathbf{k}}(\mathbf{r}) = \mathbf{u}_{\mathbf{k}}(\mathbf{r})e^{i\mathbf{k} \cdot \mathbf{r}}, \quad (1.7)$$

where \mathbf{k} is the wave vector spanning the first Brillouin zone of the reciprocal lattice. The solutions are plane waves modulated by periodic functions called Bloch functions. In this way it is possible to construct a band diagram which provides the dispersion relation between the frequency and the wave vector $\omega(\mathbf{k})$. For each \mathbf{k} the range of accepted frequencies can be extracted from this band diagram. Depending on the parameters of the lattice (refractive index, lattice constant and so on), there might be a range of frequencies where the

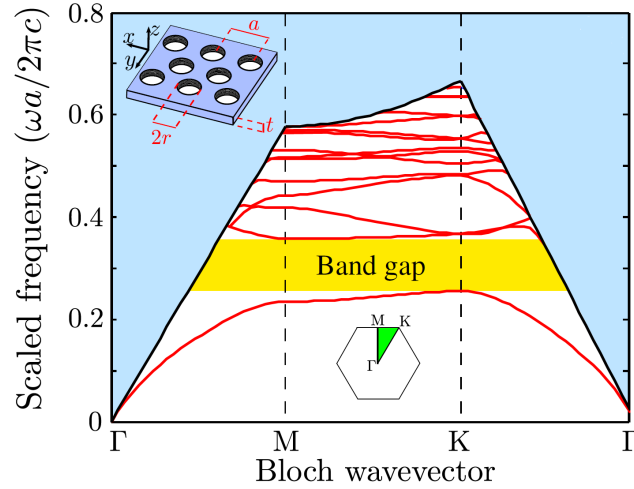


Figure 1.4: Calculated band diagram of a triangular PhC made of holes etched in a GaAs slab for the TE-like mode, with thickness $t = \frac{2a}{3}$ and hole radius $r = \frac{a}{3}$. The blue shading shows the continuum of radiation inside the light cone and the yellow area indicates the photonic bandgap [48]. The inset shows the high symmetry points of the first Brillouin zone.

light cannot propagate within the crystal. These frequencies are called photonic bandgaps. An example of band diagram calculations which are carried out numerically is shown in figure 1.4.

By introducing defects in the crystal structure of a photonic bandgap material (for example by removing some holes in a 2D PhC), localized modes (with frequencies within the photonic bandgap) will be allowed to exist in that defect while forbidden to propagate within the crystal. In this way it is possible to create optical confinement and a range of photonic crystal cavities (PhCCs) and waveguides (PhCWGs) can be realized.

1.5 Cavity quantum electrodynamics

1.5.1 Jaynes-Cummings model

The study of the interaction of an atom with an electromagnetic mode inside a cavity, where the quantum nature of electromagnetic radiation is not negligible, is called cavity quantum electrodynamics (CQED). Although the theoretical formulation of CQED dates back to the work of Jaynes and Cummings in the 60s [49], the first experimental realizations of these systems have been realized around 30 years ago with the work of S. Haroche (who has been awarded the Nobel prize in physics in 2012 with D. Wineland for their work on controlling quantum systems). In the following we briefly introduce the simplest formulation of CQED.

When a two-level system is coupled to a quantized monochromatic electromagnetic field the interaction between them is described by the Jaynes-Cummings Hamiltonian:

$$H = \hbar\omega_a\sigma_+\sigma_- + \hbar\omega_c a^\dagger a + \hbar\Omega(a^\dagger + a)(\sigma_+ + \sigma_-). \quad (1.8)$$

Here $\sigma_+(a^\dagger)$ and $\sigma_-(a)$ indicate raising and lowering operators of atom (cavity mode), respectively. ω_a , ω_c and $\Omega = \mu E_1$ indicate the frequency of the atom, cavity and the interaction rate of atom and the cavity mode where:

$$\mu = \langle g | \mathbf{D} \cdot \epsilon | e \rangle \quad E_1 = \sqrt{\frac{\hbar\omega}{2\epsilon_0 V}} \quad (1.9)$$

μ and E_1 are dipole moment of the atom and electric field per photon respectively, where \mathbf{D} is the dipole operator of the atom, ϵ indicates the unit vector in the direction of the electric field and V is the volume of the mode. $|g\rangle$ and $|e\rangle$ are the ground and excited states of the atom. By decreasing the volume of the mode in a cavity the interaction between the atom and the cavity can be made very strong.

1.5.2 Coupling to the environment

While the Hamiltonian 1.8 allows calculating the evolution of the wavefunctions of an isolated quantum system, the loss and decoherence rates due to the coupling to the environment are best studied by the evolution of the density

matrix. The density matrix is a matrix that describes a quantum system in a statistical mixture of several different quantum systems. If a quantum system is in state $|\psi_i\rangle$ with the probability p_i the density matrix of the system is defined as:

$$\rho = \sum_i p_i |\psi_i\rangle\langle\psi_i| \quad (1.10)$$

where:

$\sum p_i = 1$ and $p_i > 0$. In order to describe a physical state a density matrix operator should be Hermitian, positive and $Tr(\rho) = 1$, where Tr indicates the trace of the matrix. The diagonal and off-diagonal terms of the density matrix indicate the population and the coherence of the eigenstates of the system. The expectation value for a given observable can be calculated as:

$$\langle A \rangle = \langle A \rangle_\rho = \sum_i p_i \langle \psi_i | A | \psi_i \rangle = Tr(\rho A) \quad (1.11)$$

Equation of motion for the density matrix:

The Schrödinger equation gives the dynamics of a quantum state which is not being driven by any external interaction is given as:

$$\frac{\partial}{\partial t} |\psi\rangle = \frac{-i}{\hbar} H |\psi\rangle, \quad (1.12)$$

where the Hamiltonian of the system is time-independent. From this we can drive an equation of the motion for the density matrix:

$$\frac{\partial \rho}{\partial t} = \frac{\partial}{\partial t} \sum_i p_i |\psi_i\rangle\langle\psi_i| = \frac{-i}{\hbar} \sum_i p_i (H |\psi_i\rangle\langle\psi_i| + |\psi_i\rangle\langle\psi_i| H), \quad (1.13)$$

which finally leads to:

$$\frac{\partial \rho}{\partial t} = \frac{-i}{\hbar} [H, \rho], \quad (1.14)$$

This equation is known as Liouville-von Neumann equation. In order to extend this result to the case of a quantum system interacting with the environment and derive the Lindblad form of the Master equation, we only introduce the fundamental assumptions involved in the derivation. The mathematical details of the derivation can be found elsewhere [50].

The first approximation which is also known as Born approximation, assumes that the interaction between system and environment is weak such that

the effect of the system on the environment is negligible, which can be summarized as:

$$\rho(t) \approx \rho_S(t) \otimes \rho_E, \quad (1.15)$$

here $\rho_S(t)$ and ρ_E indicate the density matrix of the system and the environment.

The second important approximation is the Markov approximation which assumes that the time scale over which the state of the system varies appreciably (τ_S) is much larger compared to the time scale corresponding to the environment's decay functions (τ_E) [50]. In other words the dynamics of the system cannot be resolved in the time scales in the order of τ_E , which means the system's evolution is described in a coarse-grained time scale. Finally the rapidly oscillating terms as compared to τ_S have been neglected which is known as rotating wave approximation.

The aforementioned approximations lead to the Lindblad form for the Master equation of the system:

$$\dot{\rho}_S = \frac{-i}{\hbar}[H, \rho_S] + \sum_i \Gamma_i \mathcal{L}_{A_i}(\rho_S) \quad (1.16)$$

where

$$\mathcal{L}_{A_i}(\rho_S) = A_i \rho_S A_i^\dagger - \frac{1}{2}(A_i^\dagger A_i \rho_S + \rho_S A_i^\dagger A_i), \quad (1.17)$$

here A_i and E_i are the operators of the system and the environment that define the interaction of the system with environment in the form:

$$H_I = \sum_i A_i \otimes E_i, \quad (1.18)$$

and Γ_i is the corresponding interaction rate.

1.5.3 Weak and strong coupling regimes of CQED

In a CQED system the interaction of the two-level system (atom) and the cavity with the environment can be described by Lindblad formalism where we define γ and κ as the interaction rates between the atom and the cavity with the environment (i.e. the decoherence rates). Two distinct regimes can be distinguished:

If coupling between the cavity and the atom dominates the other lossy channels γ and κ ($g \gg \kappa, \gamma$), then we are in the strong coupling regime. In this

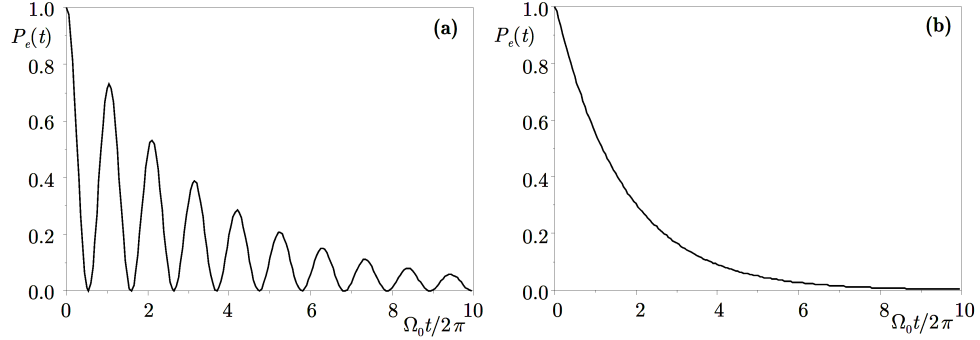


Figure 1.5: Probability of finding two-level system in the excited state versus time (in units of vacuum Rabi period) in an atom-cavity system for (a) strong coupling regime $\kappa = 0.1\Omega_0$ and (b) weak coupling regime $\kappa = 10\Omega_0$ from Ref. [51]. Ω_0 and κ indicate the atom-cavity coupling and cavity loss rate, respectively.

regime Rabi oscillations in the population dynamics of the atom can be observed which after sometime smear out due to dissipation (indicated in figure 1.5a). This regime is also characterized by the "dressing" of the atomic levels by the cavity excitation and formation of mixed eigenstates of the atom-cavity system [52]. When the loss rate of the cavity is higher than the atom-cavity interaction we are in the weak coupling regime where the excited-state population of the atom decay exponentially and no oscillations is observed (figure 1.5b). In this regime the main effect of the cavity is to modify the decay rate of the atom by a factor of F_P , named as Purcell factor [53]:

$$F_P = \frac{3}{4\pi^2} \frac{Q\lambda^3}{V}, \quad (1.19)$$

where $Q = \frac{\omega}{\kappa}$ is the quality factor of the cavity, λ is the wavelength of the cavity mode (assumed to be in resonance with the atom) and V is the volume of the cavity.

CQED systems have been demonstrated first in atomic systems in weak and strong coupling regimes and used to create an entangled state between the atom and the cavity [51]. In solid-state structures, CQED systems consisting of semiconductor QDs coupled to micropillar and PhC cavities in weak and strong coupling regimes have been realized and used as efficient sources of single photons [54, 55].

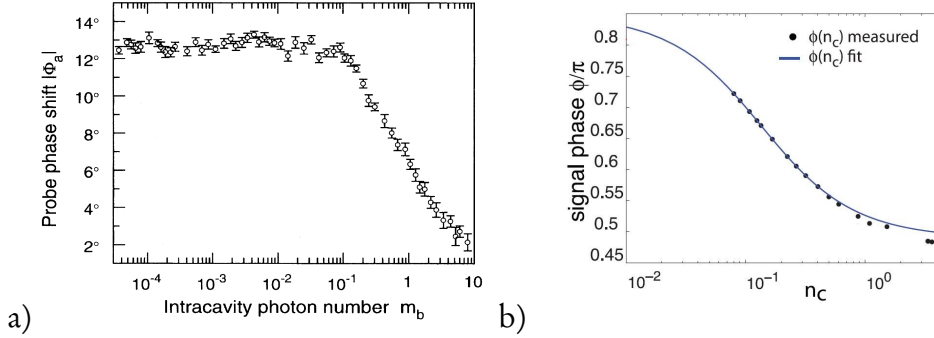


Figure 1.6: (a) Conditional phase shift of the probe beam as a function of the intracavity photon number in a (a) cesium atom-optical cavity system [56] and (b) a QD-PhCC system [57].

1.6 Quantum information processing using optical nonlinearities

As mentioned earlier there are several proposals for implementation of quantum information including CQED based systems (superconducting qubits [58], trapped ions and Rydberg atoms [59]) and solid-state spin systems [60]. There has been rapid progress in the implementation of quantum information protocols in all these platforms but no system shows a clear practical edge over the others indicating the long road ahead towards the maturity of quantum information technology. Another approach for realization of QIP is the optical approach. The first proposal for optical realization of the QIP is known as KLM proposal where by combining linear optics and nonlinear detection, QIP algorithms have been implemented [61]. In this approach, the number of required optical components scales very quickly with the number of qubits which makes it very demanding to realize. Another interesting optical approach is based on single-photon nonlinearities. In this approach the realization of a two-qubit gate is demanding due to the weak interaction between photons. There have been different proposals for strengthening this interaction. In this section we briefly review the state-of-the-art in the investigation of single-photon nonlinearities and their application to photonic quantum information processing.

The first proposal for implementing quantum information with optical nonlinearities was based on using cross-Kerr nonlinearity [62], where the refractive

index of a material changes proportionally to the intensity of the light applied to it. Despite myriad of proposals in the theoretical side [63, 64], the progress in experiments was hampered by the fact that natural nonlinearities produced by the Kerr effect are extremely weak and noisy [65]. Later Schmidt and Imamoglu [66] proposed that the media showing electromagnetically-induced transparency [67] can show stronger optical nonlinearity which can be in the range of practical values for realizing an optical quantum gate.

The idea that a single quantum emitter inside a cavity (waveguide) can induce a giant optical nonlinearity has been studied extensively [68]. The first experimental realization was in a cavity containing cesium atoms, where a pump and probe beam were sent through the atom-cavity system and their relative induced phase shift was measured [56]. The value of phase shift obtained in that experiment was still not enough ($\delta \approx 16^\circ$) for realizing an optical gate (see figure 1.6a). Later a modified version of this configuration and a new scheme of implementing optical quantum gates in atom-cavity systems were proposed theoretically [69, 70, 71]. Furthermore the CQED nonlinearity was exploited recently for realization of single-photon optical switches and transistors in atomic systems [72, 73].

In the solid-state CQED systems there has been progress for realization of nonlinearities in the strong coupling regime where by using the nonlinearity of Jaynes-Cummings energy ladder in a strongly coupled QD-PhC cavity system, different functionalities like optical switching [74, 75, 76], strong photon correlation [77], conditional reflectivity [78] and phase shift [57] (see figure 1.6b) have been demonstrated. The use of giant optical nonlinearities in weakly coupled QD-photonic cavities, where the nonlinearity originates from the saturation of the QD with one photon, has been theoretically investigated [68, 79, 80]. Another nonlinear phenomenon that has recently attracted attention is stimulated emission whose demonstration in a CQED system and its applications have been studied theoretically recently [81, 82, 83, 84]. We note however that a single-photon nonlinearity does not automatically guarantee the possibility of applications in a quantum gate [85].

1.7 Scope and outline of this thesis

The general goal of this thesis is the generation and efficient extraction of single-photons from the QDs inside QPICs. For achieving QIP with single photons in an integrated platform this goal has very high importance. In this work, by

proposing new design and fabrication methods, the issue of the efficient transfer of single photons between different components of the QPIC and the problem of the extraction of single-photons from QDs generated by resonant pumping (filtering of the scattered laser) has been addressed and solved.

Chapter 2 focuses on experimental methods used in this work including fabrication, (time-resolved) micro-photoluminescence spectroscopy and single photon detection methods.

Chapter 3 includes a theoretical investigation of two single-photon nonlinear phenomena by using a Master equation based numerical approach and the conditions for their experimental realization in our system.

Chapter 4 concentrates on different technological advances made during this work for efficient coupling of light in the single photon level into a PhC cavity. These methods include design and fabrication of a RWG-PhC interface for efficient coupling, a PhC-based integrated filter, thin film deposition for the suppression of Fabry-Perot reflections by RWG cleaved end facets and integrated gratings for coupling to the top.

Chapter 5 addresses the efficient coupling of single photons generated in PhC cavity into ridge waveguides. In the second part the progress toward demonstration of dipole-induced reflection in our system and the outlook of its feasibility have been discussed.

Chapter 6 introduces a novel method based on k-vector and polarization filtering used for successful suppression of resonant driving laser and detection of resonance fluorescence of QDs inside RWGs. Finally the conclusion of present work and possible directions for future progress and applications are presented in **Chapter 7**.

This chapter explains the experimental methods used in this work. The first part describes the fabrication methods and in the second part the measurement methods and experimental setups used for optical measurements are explained.

2.1 Fabrication

Recently tremendous progress has been achieved in the field of nanofabrication. This progress is originated and motivated by the fabrication methods needed for the realization of the electronic circuitry [86] but nowadays has found numerous applications in the fields of medicine, defence, space and communication. The fabrication of structures with smaller dimensions (below $1\ \mu m$) has attracted a two fold interest: at the fundamental scientific level these structures provide suitable tools for the study of the effects where quantum mechanics plays the major role due to the low dimensions of the system, while at the application level reduced dimensions can provide more sensitivity for example in biosensors and more computation and communication power in semiconductor devices [87].

Usually the two main approaches for nanofabrication are the top-down and the bottom-up approaches. In the first approach the fabrication starts with a bulk material and continues with transferring designs on the surface of the material and subsequent transfer of the pattern by etching techniques. The second approach mostly relies on self assembly of smaller units of material like molecules for realization of the nanostructures.

2.1.1 Material growth

The growth of the material used in this work is done by Molecular Beam Epitaxy (MBE) method. This method is performed in high or ultra-high vacuum which results in much better purity and growth control comparing to other growth methods. On the other hand the process is rather slow which makes its industrial application more difficult. The mechanism of the working of the MBE is as follows: The III-V materials (e.g. Ga and As) in ultra pure form are heated in effusion cells where the sublimation occurs and the resulting vapors ("beams", due to their long mean free path) condense on the wafer and react with each other to create the desired combination. A sacrificial layer of AlGaAs (1.5 μm thickness) is deposited on the GaAs substrate which is followed by the Stranski-Krastanov growth [88] of the InAs QDs in the middle of a thin GaAs (320 nm) layer. The density of the dots is around 10-20 μm^{-2} which emit around 1300 nm wavelength [89].

2.1.2 Thin film deposition

The deposition of thin films plays an important role in nanofabrication. In this work SiN has been used as hard mask for realization of PhCs and RWGs and also as a thin anti-reflection (AR) coating layer for the suppression of the reflection at the two cleaved end facets of the RWGs. Deposition of SiN is done by plasma enhanced chemical vapor deposition (PECVD) using an Oxford Plasmalab System 100 machine. Here silane (SiH_4) and ammonia (NH_3) gasses are injected into the reaction chamber with gas flows of 17 and 13 sccm, respectively. The sample in the reaction chamber is heated up to 300°C, where the two gasses react on the hot surface of the sample to form SiN. The reaction rate of the two gasses is enhanced by generating a plasma of the two reactant gasses by using a RF generator. This reaction generates a layer of SiN on the sample surface which has a thickness that can be controlled by knowing the deposition rate (around 15 nm/s).

For SiN deposition as AR coating layer we lowered the temperature of the reaction chamber to 100°C with gas flow rates of 15.7 and 14.3 sccm for (SiH_4) and (NH_3), respectively. This resulted in SiN layer with refractive index of 1.806 (measured with ellipsometry), with a deposition rate of around 17 nm/s. The SiN layer has good adhesion to the GaAs surface and follows the shape of the sample.

2.1.3 Electron-beam lithography

In order to transfer the mask pattern to the surface of the sample the electron-beam lithography (EBL) technique has been employed in this work. In this machine a beam of electrons generated by a filament is focused on the surface of the sample which is coated by the electron resist. Electrons change the solubility of the resist in exposed areas, thereby enabling the removal of the exposed (unexposed) parts of the sample for positive (negative) resists when immersed in the developer solvent. This method has higher resolution but lower throughput in comparison with photolithography.

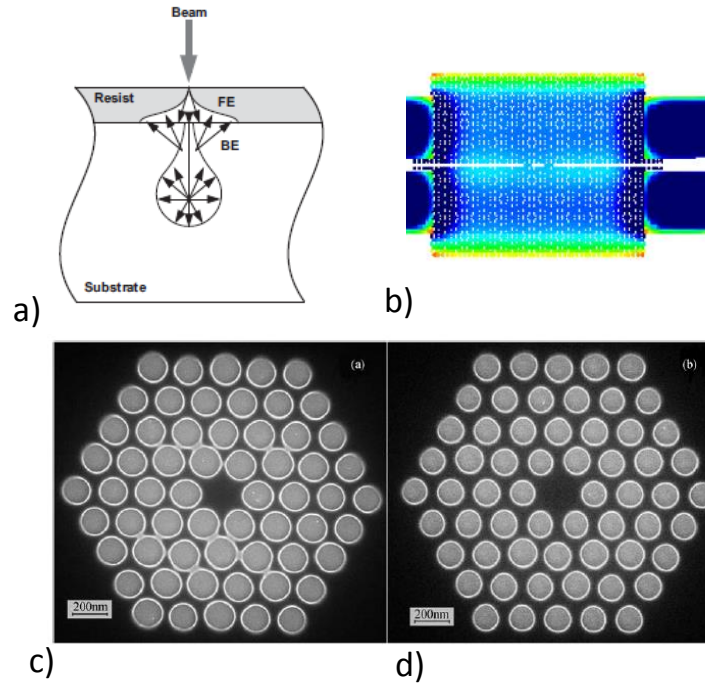


Figure 2.1: (a) Different scattering processes during the electron beam exposure [90]. (b) A sketch of the proximity effect corrected mask used for fabricating PhCs. A PhC structure after exposure with EBL and development (c) without and (d) with proximity effect correction [91].

In this work a 30 kV EBL (RAITH150-TWO) has been employed where the mask pattern on the sample surface is generated by an advanced electronic system which controls the position of the electron gun. The position of the sample on the stage is controlled by the motorized stage and is precisely detected

by laser interferometry. After transfer of the sample to the vacuum chamber and alignment, the exposure is done automatically by the help of a computer program. In the normal exposure mode the machine divides the exposure area to $100 \times 100 \mu m^2$ exposure fields and performs the exposures sequentially. For exposing long features ($\approx mm$) like RWGs another mode of exposure (fixed beam moving stage (FBMS), where the electron beam is fixed and the stage moves) has been employed.

One of the main problems encountered in EBL is the phenomenon of proximity effect. This effect is generated by the collisions between electrons with lighter atoms in resist and cross electron collisions (forward scattering) and also by collision between electrons and heavier atoms in the substrate (backward scattering) as indicated in figure 2.1a. The final result is that each feature receives more dose than assigned in the design which manifests itself in a PhC structure by the fact that the holes close to the borders of the structure are smaller than the ones in the center (figure 2.1c and d).

In order to compensate for this effect a proximity effect correction (PEC) software (RAITH NanoPECS) has been used to adjust the doses and create a homogeneous energy distribution. Monte Carlo simulations for the electron trajectory in our structure were performed and the results were fitted with the spread function: [92]

$$f(r) = \frac{1}{\pi(\eta + \nu + 1)} \left(\frac{1}{\alpha^2} e^{-\frac{r^2}{\alpha^2}} + \frac{\eta}{\beta^2} e^{-\frac{r^2}{\beta^2}} + \frac{\nu}{2\gamma^2} e^{-\frac{r}{\gamma}} \right), \quad (2.1)$$

where the first and second (Gaussian) terms ($\alpha = 30 \pm 10$ nm and $\beta = 1.86 \pm 0.01 \mu m$) are related to forward and backward scattering, respectively and the third term ($\gamma = 930 \pm 10$ nm) is related to the collision of electrons with high atomic number atoms of the GaAs substrate and the weights are $\nu = 0.57 \pm 0.02$ and $\eta = 0.35 \pm 0.02$. The EBL system calculates the right dose distribution to compensate the proximity effect which results in a better exposure pattern. A typical PhC mask after PEC can be seen in figure 2.1b.

2.1.4 Etching methods

Etching is the process of the transfer of the pattern exposed on the resist to the material where the parts not exposed is protected against the etchants. Usually there are two vastly used categories of etching in the nanofabrication: wet and dry etching. Dry etching is performed without any liquid etchant and is mostly

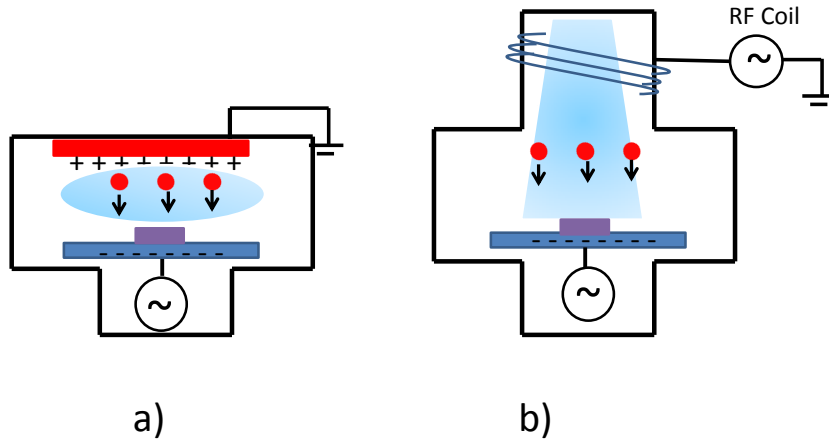


Figure 2.2: (a) A sketch of the RIE chamber where the electrons are accelerated toward the the bottom electrode after generation of the plasma. The accumulation of the electrons creates a bias voltage that accelerates the heavy ions toward the sample. (b) A sketch of the ICP chamber where the plasma is generated with a magnetic coil at a higher temperature.

done by creating a plasma in the vacuum environment where the reactive materials in the form of gasses are introduced. The plasma is generated by a RF field which ionizes the gasses and accelerates the ions toward the sample. In wet etching the sample is immersed in a liquid etchant which is able to solve and corrode the target layer of the material with a high selectivity.

Dry etching

Depending on the needed isotropy different methods of etching have been employed in this work. First etching method is reactive ion etching (RIE) (see figure 2.1a) where a strong (13.56 MHz) RF electric field by creating a plasma ionizes the etchant gasses and dissociates the electrons off them. The lighter electrons (compared to the ions) are accelerated more toward the grounded bot-

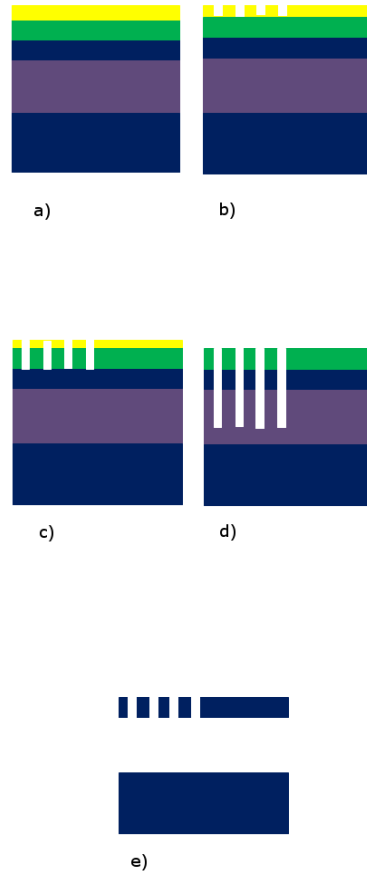


Figure 2.3: Process flow for the fabrication of the single PhC structures. (a) deposition of SiN (green) and ZEP (yellow) layers, (b) exposure and development of the ZEP, (c) etching SiN layer in opened areas with RIE, (d) removal of the ZEP with the O_2 and etching with ICP and (e) wet etching with HF 10%. Dark blue and violet colors indicate GaAs and AlGaAs layers, respectively.

tom electrode of the chamber and get absorbed by it. This creates a negative self bias in the order of few hundred volts which accelerates the plasma (which now has higher concentration of positive ions due to the removal of the electrons) and makes the positive ions collide with the sample and etch it. For etching SiN a CHF_3 (etching rate ≈ 20 nm/s) and for etching GaAs a methane/hydrogen

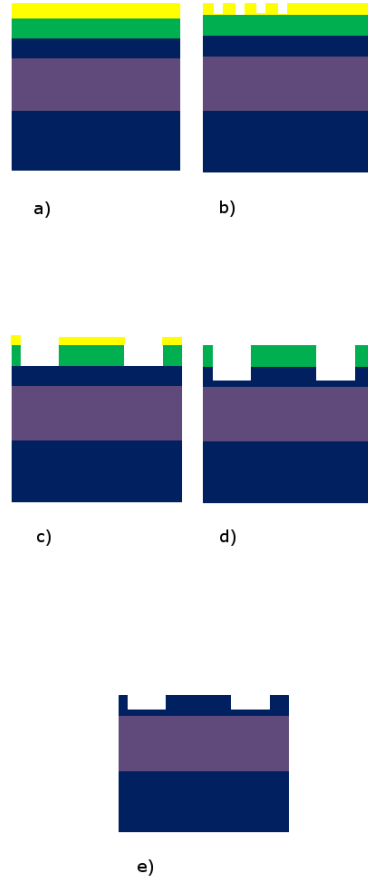


Figure 2.4: Process flow for the fabrication of single RWG structures. (a) deposition of SiN (green) and ZEP (yellow) layer, (b) exposure and development of the ZEP, (c) etching SiN layer in opened areas with RIE, (d) removal of ZEP with O_2 and etching of the GaAs layer with RIE and (e) removal of SiN with HF 10%. Dark blue and violet colors indicate GaAs and AlGaAs layers, respectively.

(etching rate ≈ 70 nm/s) based plasma (Oxford Plasmalab 100) have been used.

For etching high aspect ratio holes in PhCs deeply and with a vertical profile an inductively coupled plasma (ICP)RIE has been employed. In ICP a high density chlorine based plasma is generated at high (200°C) temperature with the help of a magnetic field created by a coil (see figure 2.1b). Etching rates

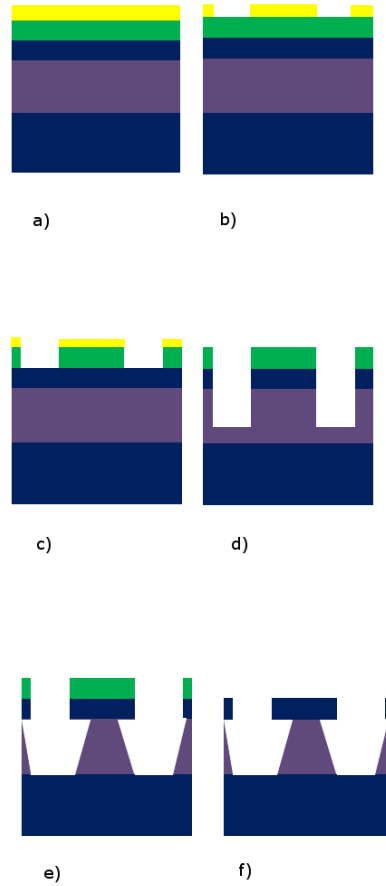


Figure 2.5: Process flow for the fabrication of the coupled RWG-PhC structures. (a) deposition of SiN (green) and ZEP (yellow) layer, (b) exposure and development of the ZEP, (c) etching SiN layer in opened areas with RIE, (d) removal of the ZEP with the O_2 plasma and etching with ICP, (e) wet etching with HCl 36% and (f) removal of SiN with CF_4 plasma and final surface cleaning with H_3PO_4 10%. Dark blue and violet colors indicate GaAs and AlGaAs layers, respectively.

around 400 nm/s for GaAs and $Al_{0.7}Ga_{0.3}As$ layers have been measured with this etching method.

Lastly, when wet etching is not possible and high isotropy is required a barrel etcher (TePla 100) is used. In this machine a microwave source generates

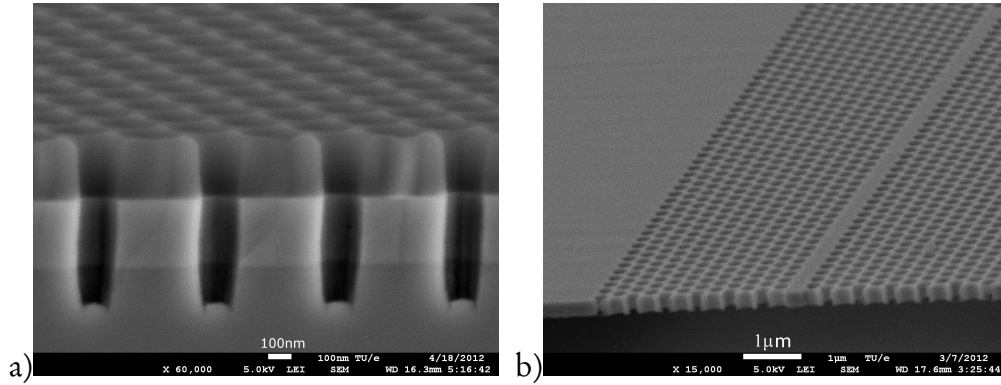


Figure 2.6: (a) A SEM picture of the PhC structure after etching by the ICP. The sample is cleaved to observe the profile of the holes after the etching. (b) A SEM picture of a PhCWG realized by the recipe mentioned in section 2.1.5 and cleaved after the process.

the plasma inside an isolated chamber. This reduces the anisotropy since there is no DC bias and ion bombardment. The barrel etcher is used with O_2 for cleaning the surface of the sample and with CF_4 gas for the removal of the SiN.

Wet etching

In the realization of single, free-standing PhC structures hydrofluoric acid (HF 1-10%) has been employed for isotropic etching of SiN and $Al_{0.7}Ga_{0.3}As$ with an etching rate of 30-200 nm/s. This method of etching is fast and harder to control geometrically.

During the course of this work it has been experimentally found that cold ($2^\circ C$) HCl can etch an $Al_{0.7}Ga_{0.3}As$ layer with strong anisotropy. This anisotropy originating from different etching rates along different crystallographic orientations, results in a tilted profile which makes a $\approx 55^\circ$ angle with the substrate and has been used with other material previously [93, 94]. Depending on the crystallographic orientation, this etching technique can be used to create a trapezoidal support for the RWGs (see figure 2.7b). If the waveguide is fabricated along [011] crystallographic direction a trapezoidal support can be realized where the short base is connected to rectangular (GaAs) waveguide. We realized that the undercut in thick ($> 1 \mu m$) $Al_{0.7}Ga_{0.3}As$ layers is stopped

after $0.8 \mu\text{m}$, making the control of the size of the trapezoidal base possible by changing the waveguide width (it can also be concluded that the waveguides with $< 1.6 \mu\text{m}$ width will be suspended). The proposed etching method makes the fabrication of the coupled PhC-RWG system much easier by enabling the fabrication of this system in a single lithographic step without the need to align them with respect to each other, thus avoiding alignment errors and reducing process time dramatically.

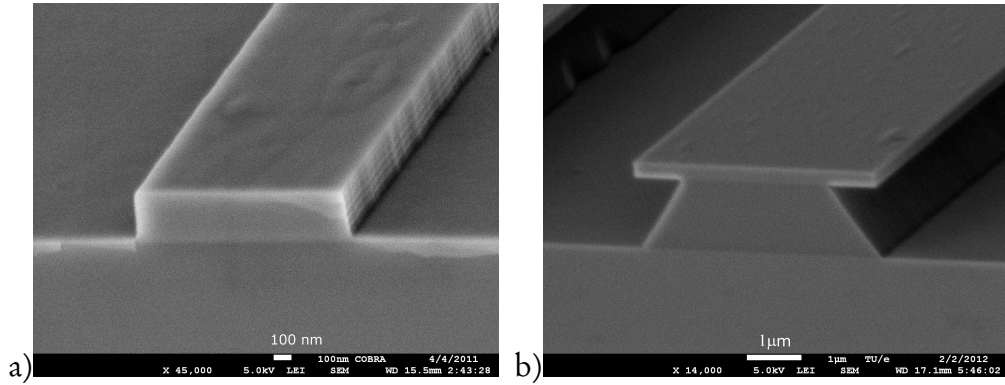


Figure 2.7: (a) A SEM picture of a rectangular RWG where the etching of GaAs layer has been stopped before reaching AlGaAs (sacrificial) layer. (b) a RWG realized by etching of the sacrificial layer with HCl resulting in formation of a trapezoidal support.

2.1.5 Process flow

In this section the fabrication recipes for the realization of the single PhC and RWG structures and coupled RWG-PhC system are explained. As indicated our material system is composed of a 320nm GaAs layer (with a layer of low density InAs QDs embedded in its middle) on top of $1.5 \mu\text{m}$ thick sacrificial AlGaAs layer which is in turn on top of a GaAs substrate. In all these cases the first steps are as follows (the schematic of these recipes have been shown in figures 2.3-5):

1. After preliminary cleaning of the surface of the sample (10 minutes O_2 plasma in barrel etcher and 2 minutes immersion in HCl 1:1 H_2O solution), a 400 nm thick layer of SiN is deposited (≈ 28 min deposition time) on the surface of the sample.

2. A 360 nm thick layer of polymer electron beam resist (ZEP 520A) is deposited on the surface of the sample by spin coating. The ZEP coated

sample is baked for 4 minutes with a hot plate whose temperature is gradually increasing from 100 to 150 °C and subsequently 2 minutes at 200 °C. After baking, the sample is placed inside the EBL and the design is exposed on the resist coated surface. After the EBL, the sample is developed in n-amyl acetate for 1 minute and rinsed for 40 seconds in methyl isobutyl ketone (MIBK) / isopropanol solution to stop the development.

3. The exposed design is further transferred into the sample by etching the SiN layer for ≈ 20 minutes with CHF_3 plasma based RIE. This process etches simultaneously SiN in open (developed) areas of the design and the protecting ZEP layer in unexposed areas with a lower rate (≈ 10 nm/s). After etching with RIE, the ZEP layer will be removed by 10 minutes etching with O_2 plasma in the barrel etcher.

From this stage the fabrication steps are different for different structures. First we consider the fabrication of simple PhCs:

4. In the final step the pattern is further transferred into the sample layer by 2.5 minutes etching at 200°C in ICP, which will etch GaAs/AlGaAs layer down to the middle of the AlGaAs layer (see figure 2.3d and figure 2.6a). The remaining SiN and the sacrificial layer will be removed by 2 minutes etching with HF 10% (see figure 2.3e and figure 2.6b).

The fabrication of the simple RWGs continues as follows:

4. The GaAs layer in open areas is etched by a methane/hydrogen based plasma RIE for 3 minutes. The remaining SiN layer is removed by 2 minutes wet etching with HF 10% (see figure 2.4d,e and figure 2.7a).

Finally the fabrication of the coupled PhC-RWG system continues as follows:

4. The sample is etched in ICP as in the case of simple PhC structure and subsequently wet etched in a concentrated (36%) HCl solution for 8 minutes. After wet etching the SiN layer is removed by etching in barrel etcher for 10 minutes with O_2 and subsequently 2.5 minutes with CF_4 plasma. Finally the surface of the sample is cleaned with 10% H_3PO_4 for 2 minutes (figure 2.5d,e and figure 2.7b).

2.2 Measurement setups

In this section the different optical setups used for characterization and measurement of the fabricated devices are described. One general micro photoluminescence (PL) setup has been used for characterization of the different QD samples

and cavity designs. Two other micro PL setups used in this work have the possibility of accessing emission from the top and side at low temperatures. Finally our single-photon detector and the time-resolved measurement technique are introduced.

2.2.1 Micro photoluminescence

The micro PL setup is shown in figure 2.8. The sample is kept inside a helium flow cryostat that can be cooled down to 5 K and is moved by a piezoelectric XY stage. In this setup, light can be focused on the sample by the use of a near-infrared objective (100 \times , numerical aperture (NA) = 0.6). The resulting emission is separated from the laser by a dichroic mirror and is sent to a spectrometer (Horiba-Jobin Yvon FHR 1000). The light dispersed by the spectrometer is detected by an InGaAs nitrogen cooled detector array. The sample is illuminated by a white light source and a near-infrared CCD is used to observe the surface [95].

2.2.2 Waveguide micro photoluminescence

The transmission measurements and the measurements performed in chapter 6 are done with a waveguide micro PL setup (shown in figure 2.9) where the light is coupled from the fibers (whose positions can be controlled by XYZ translational stages) via a lens (NA=0.15) to an objective (50 \times , NA=0.42) for focusing the light to the sample and vice versa, from the two sides. The top excitation and collection is done with an objective (100 \times , NA=0.5), where the excitation and collection paths are separated with the help of a beam splitter and coupled to two different fibers controlled by XYZ translational stages.

The objectives are moved by piezoelectric stages in XYZ directions. In order to investigate the sample a green light LED can illuminate the sample and the reflected light is detected by a CCD camera. The sample is kept inside a helium flow cryostat window that can be cooled down to 12 K and its temperature can be controlled.

2.2.3 Waveguide probe station

The time-resolved photoluminescence (TRPL) and antibunching measurements shown in chapter 5, are performed with an end-fire setup where lensed fibers (NA=0.33) are moved by piezoelectric positioners and can be coupled to the

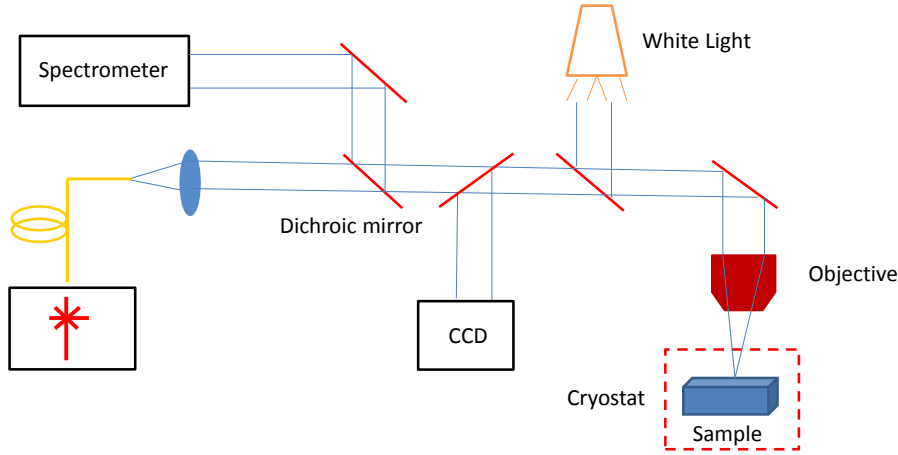


Figure 2.8: A sketch of the micro photoluminescence setup used for the characterization of the QD emission and sample designs.

sample from the two sides inside the helium flow cryostat which can be cooled down to 2 K. Top excitation can be done by an objective (100 \times , NA=0.5) and the temperature of the setup can be controlled by a temperature controller. The setup has also a RF probe and provides the possibility of the electro-optical measurements (not used in this work).

2.2.4 Superconducting single photon detector

The single-photon detector used in this work is a superconducting single photon detector (SSPD). The detection mechanism of the SSPD is as follows [28]: Upon the absorption of a photon in a superconducting nanowire a Cooper pair breaks, creating a lot of quasi particles. The generated "hot spot", perturbs the supercurrent flow in the nanowire, resulting in the transition to the resistive state and production of a voltage pulse. The single photon detection system used in this work is made of two SSPDs installed at the bottom of a cryogenic

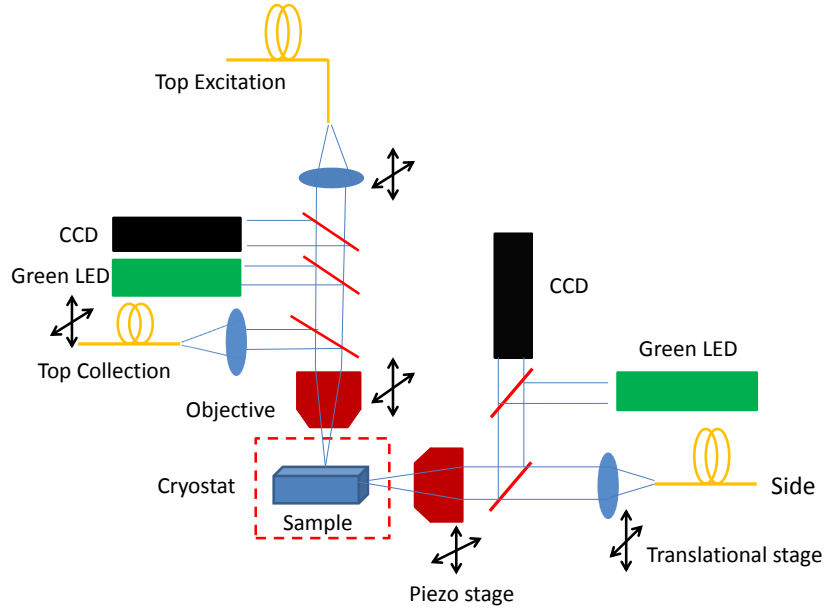
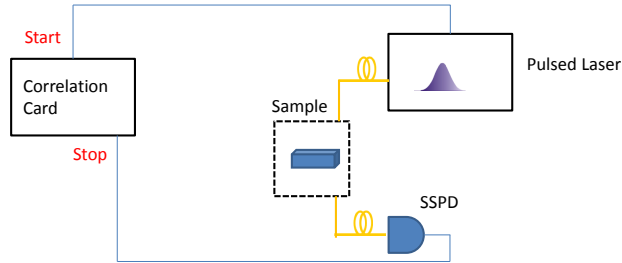


Figure 2.9: A sketch of the waveguide micro photoluminescence setup, where the optical emission of the samples can be accessed via three axis.

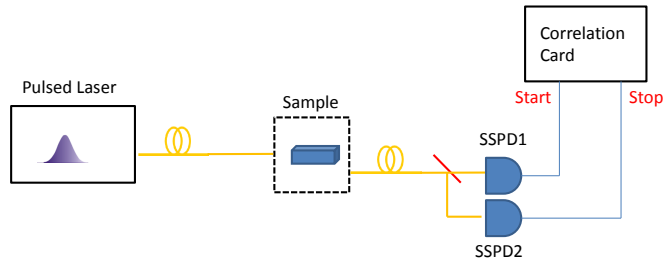
stick which is placed inside a helium dewar to be cooled down to 1.6 K [96]. The applied bias current can be controlled and is set to a value which ensures the best trade-off between the dark count rate and the detection efficiency (in this work these values were typically around hundreds of Hz and 10%, respectively).

2.2.5 Time-resolved photoluminescence and anti-bunching measurements

The TRPL measurements performed in this work are done by time-correlated single-photon counting using a fast correlation card (PicoHarp 300 with 4 ps temporal resolution). In order to perform TRPL a pulsed laser provides the start transistor-transistor logic (TTL) signal and the arrival of the electric pulse from SSPD (generated by the incidence of single photons) provides the stop signal. By repeating this cycle many times one can reconstruct the single decay profile (histogram) from single photon collection events over a large number



a)



b)

Figure 2.10: Schematic of the experimental arrangement for (a) time-resolved PL, where the pulsed laser sends the start signal for the correlation card and the electric pulse coming from the SSPD after the photon detection event provides the stop signal, and (b) anti-correlation measurements, where the emission of the sample is sent through a fiber-based beam-splitter to the two channels of the SSPD and the subsequent electric pulses provide the start and the stop signal for the correlation card.

of cycles [97]. The trigger level of the counter is set to a value which ensures the elimination of the electrical noise in our SSPD. In the anti-bunching measurements the signal is sent to a 50-50 beamsplitter. The two outputs of the beamsplitter are connected to the two SSPDs where one of them provides the start and the other one provides the stop signal. The schematic of the experiments for TRPL and antibunching measurements performed in this work are drawn in figure 2.10.

Theoretical Investigation of Single-photon Nonlinear Phenomena

3.1 Introduction

Single photons are one of the best candidates for quantum information and computation since they can travel long distances without strong interaction with their environment [9, 98]. The difficulty of the implementation of quantum computation with photons comes from the fact that they hardly interact with each other. This makes it very hard to build all-optical devices at the single-photon level, where presence of a single control photon can control the behavior of another target photon. This difficulty has made the single-photon nonlinearity a long-standing goal in the field of quantum optics.

One of the most promising systems for realization of the strong nonlinearity at the single photon level is the cavity quantum electrodynamics (CQED) system, where a single two-level emitter is embedded in a cavity, whose presence enhances the interaction of the emitter with the electromagnetic field. CQED systems have been realized in different platforms including Rydberg atoms in microwave cavities [99], single atoms in optical cavities [100, 101], superconducting qubits [102], and solid-state systems [103].

In this chapter we theoretically investigate the feasibility of two low-photon-number nonlinear phenomena in our system of a single quantum dot (QD) coupled to a photonic crystal cavity (PhCC). The first phenomenon is dipole induced-reflection (DIR) where the presence of a single photon changes the transmission of the second photon through the system. The second phenomenon

is the stimulated emission at the single photon level where the presence of a photon stimulates the emission from an inverted two-level system and creates two identical photons in the output.

The numerical simulations in this chapter are performed by using the Quantum Optics Toolbox based on MATLAB [104]. The initial design of the numerical code for the stimulated emission phenomenon was developed by Dr. R. Johne.

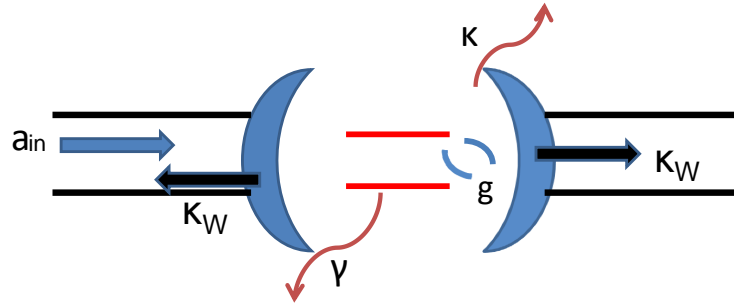


Figure 3.1: Sketch of the CQED system where a single two-level system coupled to a cavity, which is in turn coupled from the two sides to input and output waveguides.

3.2 Dipole-induced reflection

The system considered here is a two-level atomic-like emitter coupled to a cavity, which is coupled to one-dimensional continua of the modes (waveguides on the two sides), as indicated in figure 3.1. Sending light in resonance with the atom (atom and cavity are assumed to be in resonance for simplicity) with very low power (much less than one photon per emitter's lifetime in the cavity) will result in total reflection from the system where the optical system behaves like a mirror. This phenomenon is called dipole-induced reflection (DIR) and it is

the result of the destructive interference of the incoming light with the light radiated from the two-level system in the cavity [105, 68, 106]. By increasing the incoming light power to the order of one photon per emitter's lifetime in the cavity the light will saturate the atom and the system becomes transparent and transmits the photon, thus realizing an optical nonlinearity at the single-photon level. This phenomenon has applications in the realization of single- and low-photon-number optical switches and transistors [107, 57, 76, 72]. This effect has been demonstrated in solid-state systems including a single QD inside a PhCC at the edge of the strong coupling regime [75, 108, 78], where the coupling between the two-level system and the cavity mode dominates all the other loss channels. This regime of CQED is very demanding to realize in solid-state systems. In the following discussion, in view of its easier implementation, we focus on weak coupling regime where the coupling rate of the cavity to the environment is stronger than the interaction between the two-level system and the cavity mode. This regime of CQED has been previously studied theoretically and experimentally for realization of a quantum phase gate [56].

3.2.1 Numerical analysis

In this section the experimental system depicted in figure 3.1 has been studied theoretically. This system can be realized with our state-of-the-art fabrication technology by fabricating a PhCC coupled to a photonic crystal waveguide (PhCWG) which is coupled from the sides to ridge waveguides (RWGs). The two-level system is a single QD which can be embedded inside the PhC slab.

The Hamiltonian of the system reads:

$$H = \hbar\omega_a\sigma_z + \hbar\omega_c a^\dagger a + i\hbar g(\sigma_+ a - \sigma_- a^\dagger) + i\hbar(\Omega(t)a^\dagger + \Omega(t)^* a) \quad (3.1)$$

where ω_a and ω_c are the frequencies of the QD and the cavity respectively, g is the QD-cavity coupling rate, $a^\dagger(a)$ and $\sigma_+(\sigma_-)$ are creation (annihilation) operator for the cavity (QD), σ_z is the atomic inversion operator and $\Omega(t) = \sqrt{\kappa_w} E e^{-i\omega_d t}$ describes the coupling of the continuous wave (CW) input laser light to the cavity.

In order to describe the interaction of the system with the environment, the Lindblad Master equation [109] formalism for the density matrix of the system has been used. The equation of the motion for the density matrix can be written as:

$$\dot{\rho} = \frac{-i}{\hbar}[H, \rho] + \gamma L(\sigma_-)\rho + \gamma_d L(\sigma_z)\rho + \kappa L(a)\rho + \kappa_w L(a)\rho$$

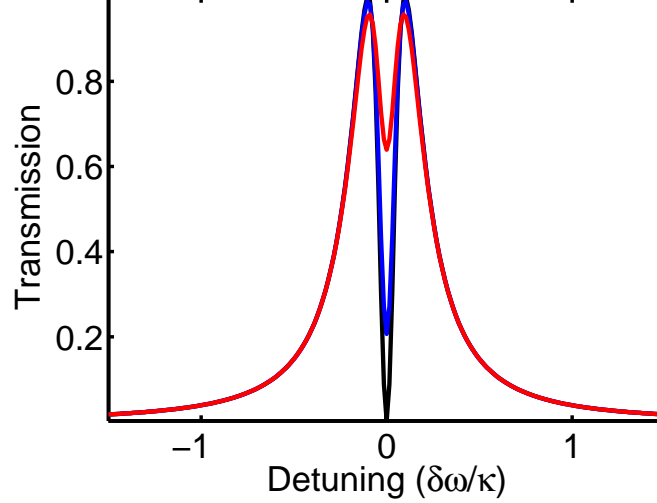


Figure 3.2: Calculated transmission of the incident light through the system as a function of the detuning of the input beam with the atom for different intensities of the input beam. The decay time of the cavity to the waveguide has been assumed to be around 10 ps, $g = \frac{\kappa_w}{2}$ and all other lossy channels have been neglected. Black: 0.04, blue: 0.1 and red: 0.3 photon per emitter's lifetime in the cavity power of the input beam. QD and cavity has been assumed to be in resonance.

where

$$L(c)\rho = c\rho c^\dagger - \frac{1}{2}(c^\dagger c\rho + \rho c^\dagger c),$$

and the coupling strength of the cavity to 1D quasi-continua of modes (waveguides in the both sides) and the dissipative environment is described by κ_w and κ , respectively. γ and γ_d indicate the coupling strength of the QD to the environment and its dephasing rate, respectively.

The equation of the motion of the density matrix has been solved in a frame rotating with the QD frequency to obtain the steady-state density matrix of the system. The transmission of the incident light as a function of its detuning from the atomic frequency is calculated as:

$$T = \frac{\langle \kappa_w a^\dagger a \rangle_{ss}}{|E|^2}, \quad (3.2)$$

where E is the amplitude of the input beam as previously described and $\langle \dots \rangle_{ss}$ indicates the expectation value of the quantity in the bracket at the steady-state.

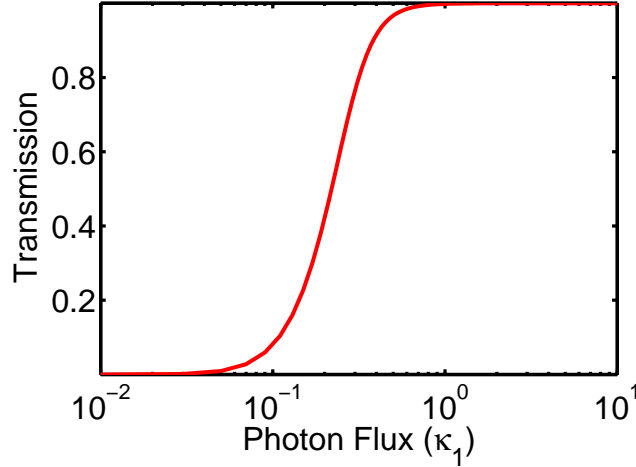


Figure 3.3: Calculated transmission of the incident beam through the system in resonance with the atom as a function of the input photon flux. The decay time of the cavity to the waveguide has been assumed to be around 10 ps, $g = \frac{\kappa_w}{2}$, $\kappa_1 = \frac{2g^2}{\kappa_w}$ is the linewidth of the emitter inside the cavity and all other lossy channels have been neglected. QD and cavity has been assumed to be in resonance.

The result of the calculations is shown in figure 3.2. Here the decay time of the cavity to the waveguide ($\tau = \frac{1}{\kappa_w} = \frac{Q}{\omega_c}$) has been assumed to be around 10 ps which indicates a $Q \simeq 10000$ for the coupling to the waveguides, $g = \frac{\kappa_w}{2}$ and the three powers of the incident light are 0.04, 0.1 and 0.3 photons per emitter's lifetime in the cavity and QD and cavity has been assumed to be in resonance. and $\kappa_1 = \frac{2g^2}{\kappa_w}$ is the linewidth of the emitter inside the cavity. All the other lossy channels have been neglected.

Here we clearly observe a dip in the transmission at the resonance frequency which is a clear indication of the DIR. As the power of the incidence light is increased, the minimum value of the transmission increases due to the saturation of the two-level system. This point becomes more clear when we plot the transmission of the incident light through the system as a function of its intensity at the resonance condition as depicted in figure 3.3. All the other parameters are the same as figure 3.2. Here a jump in the transmission of the system is observed when the power of the incident light is in the order of one photon per emitter's lifetime in the cavity which indicates a giant optical nonlinearity achieved by a very low intensity of light. These results are in agreement with

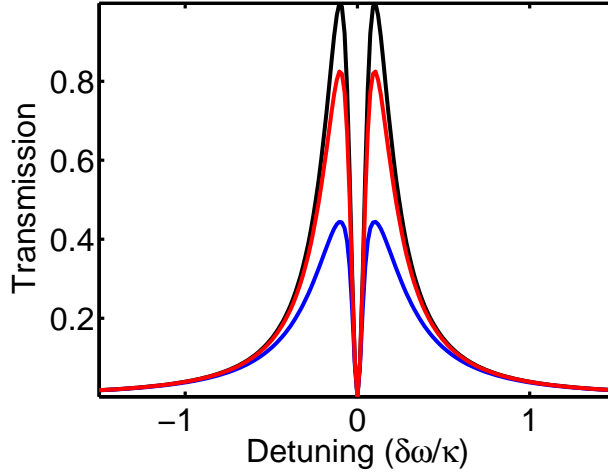


Figure 3.4: Calculated transmission of the incident light through the system as a function of the detuning of the input beam with the atom with different values of the leakage rate of the cavity. The decay time of the cavity to the waveguide has been assumed to be around 10 ps, $g = \frac{\kappa_w}{2}$ and all other lossy channels have been neglected. The power of the input light is around 0.04 photon per emitter's lifetime in the cavity. Black: $\kappa = 0$, red: $\kappa = \frac{\kappa_w}{10}$ and blue: $\kappa = \frac{\kappa_w}{2}$. QD and cavity has been assumed to be in resonance.

previous analytical calculations [68].

The effect of the dissipative interactions with the environment is also noteworthy. First we consider the effect of the cavity leakage to the environment (κ) on the signal, as it can be observed from figure 3.4. Here $\kappa = (0, \frac{\kappa_w}{10}, \frac{\kappa_w}{2})$, $g = \frac{\kappa_w}{2}$ and the QD decay and dephasing have been neglected for simplicity (the power of the input light is around 0.04 photon per emitter's lifetime in the cavity). QD and cavity has been assumed to be in resonance. When the rate of the cavity leakage to the environment increases the amount of light coupled to 1D continuum (waveguide) that will be collected as the transmitted light decreases. The same behavior is observed (not shown here) when we increase the dissipative coupling of the QD to the environment (γ).

One of the most interesting features of our system is the effect of the dephasing rate of the QD (originating from its interaction with the phononic bath and from the carrier-carrier interactions), on the transmission dip in resonance. Assuming that there are no other dissipative channels, increasing the dephasing rate increases the transmission at resonance which reduces the signal visibility. This effect can be clearly observed from figure 3.5 where the transmission of

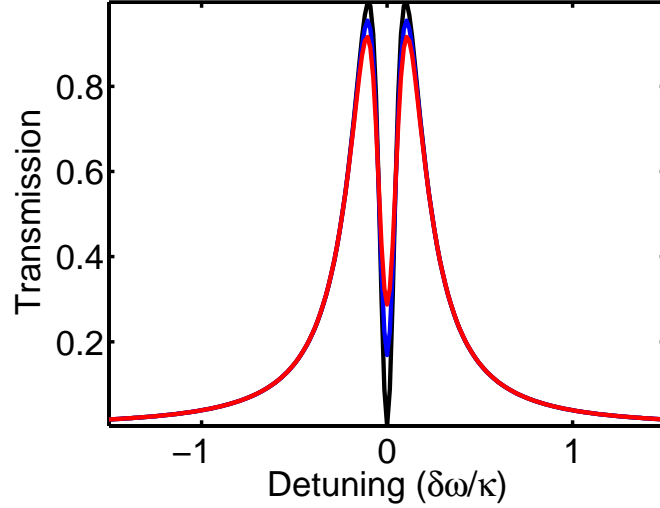


Figure 3.5: Calculated transmission of the incident light through the system as a function of the detuning of the input beam with the atom with different values of the dephasing rate of the QD. The power of the input light is around 0.04 photon per emitter's lifetime in the cavity. Black: $\gamma_d = 0$, blue: $\gamma_d = \frac{\kappa_w}{10}$ and red: $\gamma_d = \frac{\kappa_w}{5}$. QD and cavity has been assumed to be in resonance.

the incident light through the system as a function of the detuning of the input beam with the atom with different values of the dephasing rate of the QD has been calculated, where $\gamma_d = (0, \frac{\kappa_w}{10}, \frac{\kappa_w}{5})$, $g = \frac{\kappa_w}{2}$ and $\gamma = 0$ (the power of the input light is around 0.04 photon per emitter's lifetime in the cavity and QD and cavity has been assumed to be in resonance). This effect is due to the fact that acquiring higher degree of dephasing creates an undefined value of quantum phase for the radiated field from the QD, hence washing out the signature of the interference between it and the incident field.

3.2.2 Feasibility study

In this section, for a systematic study of the effect of dephasing, we use an analytical formula for the transmission of the input light as a function of the parameters of the system which has been derived by solving the Heisenberg equations of the motion [68]. The visibility of the signal defined as $\frac{T_{max} - T_{min}}{T_{max}}$ as a function of the dephasing time of the QDs and the Purcell factor of the

CQED system has been calculated and the required range of the parameters for observing DIR effect has been discussed.

By rewriting the Hamiltonian of the system to include the coupling to the 1D quasi-continua we have:

$$H = \hbar\omega_a\sigma_z + \hbar\omega_c a^\dagger a + i\hbar g(\sigma_+ a - \sigma_- a^\dagger) + \hbar\sum_m \omega_m b_m^\dagger b_m + \hbar\sum_n \omega_n c_n^\dagger c_n \\ + i\hbar\sum_m g_m(b_m^\dagger a - a^\dagger b_m) + i\hbar\sum_n g_n(c_n^\dagger a - a^\dagger c_n),$$

where the b_m and c_n represent the two quasi-continua of modes (input and output ports of the waveguide) and the last two terms describe the coupling of the cavity mode to the input and output ports of the waveguide. Writing Heisenberg equations of the motion and including the leaky channels for the coupling to the environment leads to the following analytical expression for the transmission of the incident light through the system [68]:

$$T = T_{max} \left(\frac{\beta}{1 + \beta^2 x} - 1 \right)^2.$$

Here $T_{max} = 1 + \frac{\kappa}{2\kappa_1}$, $\beta = \frac{f}{1+f}$ and f is defined as:

$$f = \frac{\gamma_f}{\gamma_a + 2\gamma_d} F_p.$$

Where γ_f , γ_a and γ_d are the spontaneous emission rate of the atom into the bulk, emission rate of the atom into the leaky modes corresponding to the out-of-plane losses, and the dephasing rate of the atom, respectively and F_p indicates the Purcell factor [53] of the QD, defined as the ratio of the spontaneous emission rate of the QD in resonance with the cavity mode over the emission rate in the bulk. κ and κ_1 are the same as defined previously. x is the saturation parameter defined as: $\frac{2P_{in}\kappa}{g^2}$, where g is the coupling rate of the cavity to the QD, P_{in} is the power of the input beam and $T \rightarrow T_{min}$ for $x \rightarrow 0$ and $T \rightarrow T_{max}$ for $x \rightarrow \infty$

Based on this formula by putting experimental values of our system for γ_f and γ_a (1 and 5 ns respectively), we obtain the feasibility plot shown in figure 3.6 which shows the contrast of the experimental signal as a function of the Purcell factor and the QD dephasing time.

From this figure it can be deduced that in order to acquire a visible signal we need to increase the Purcell Factor or dephasing time of the QD. With the best

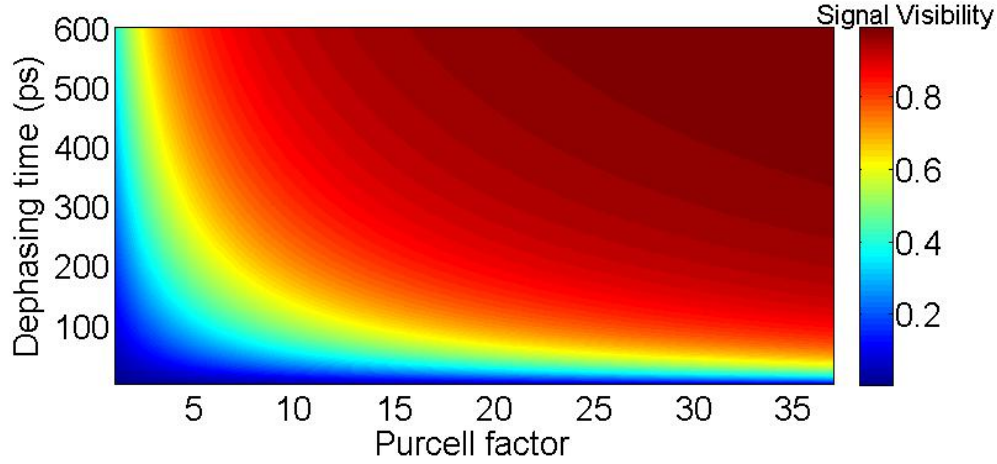


Figure 3.6: Visibility of the signal (defined in the text) as a function of the Purcell factor of the system and dephasing time of the quantum dots.

purcell factors obtained in our cavities (see chapter 5), we require a dephasing time longer than 170 ps to obtain a signal visibility of at least 30%. This depends critically on the quality of the QD growth and is hardly feasible in our InAs QDs as it will be discussed in chapter 5.

3.3 Stimulated emission

Stimulated emission was first theoretically proposed by Einstein [110]. This phenomenon was initially used to explain optical amplification in case of many emitters and electromagnetic modes and is the underlying phenomenon for the realization of lasers. Stimulated emission occurs when an incident photon interacts with an excited atom where the presence of the incident photon stimulates the inverted atom to emit a second photon identical to the first one [111]. This nonlinear behaviour can be exploited at the single-photon level for realization of the single-photon optical transistors [112] and two-photon optical gates [113] and for the investigation of quantum cloning [114, 115, 116]. In the recent years stimulated emission in single emitters has been realized in a variety of systems including surface plasmons [117], superconducting transmission lines [118] and single molecules [112] and the attention to its theoretical investigation in solid-state cavities and waveguides has been increased tremendously [84, 81, 82].

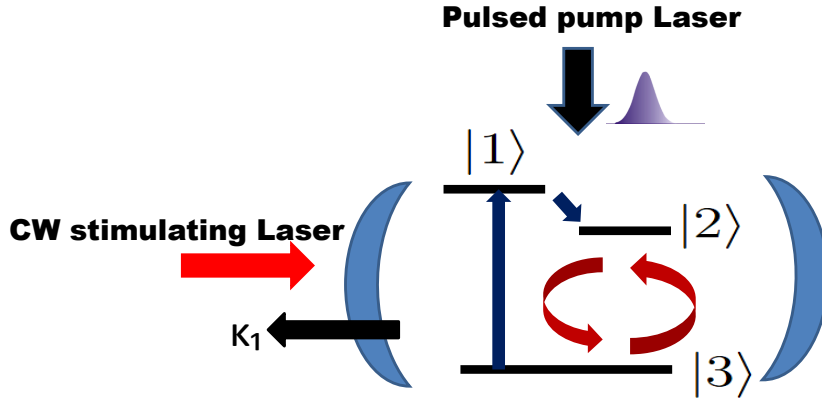


Figure 3.7: Sketch of the system considered for numerical analysis of the stimulated emission. The stimulating CW resonant laser is applied from the side and a quasi-resonant pulsed laser will put QD in the excited state.

3.3.1 Numerical analysis

In order to study the time-resolved dynamics of the stimulated emission at the single-photon level we consider an experimental system similar to the one considered in section 3.2. In this system the QD is incoherently pumped by a quasi-resonant pulsed laser from the top to an intermediate level, which quickly decays to the excited state (figure 3.7). A resonant CW laser is applied from the side via a waveguide to stimulate the transition. The reversible dynamics of the system is described by the Hamiltonian:

$$H = \hbar\omega_{23}\sigma_{23}^z + \hbar\omega_{13}\sigma_{13}^z + \hbar\omega_c a^\dagger a + i\hbar g(\sigma_{23}^+ a - \sigma_{23}^- a^\dagger) + i\sqrt{\kappa_1}(f(t)a^\dagger + f(t)^*a),$$

where ω_{23} and ω_{13} and ω_c are the frequency of the excitonic line, the intermediate level and the cavity mode and $f(t)$ describes the incident resonant (stimulating) beam (as described in section 3.2.1), $g = 0.1\kappa_1$ is the coupling strength between the cavity and the QD and

$$\sigma_{23}^z = |2\rangle\langle 2| - |3\rangle\langle 3| \text{ and } \sigma_{13}^z = |1\rangle\langle 1| - |3\rangle\langle 3|.$$

$|1\rangle$, $|2\rangle$ and $|3\rangle$ indicate the three atomic levels as depicted in figure 3.7.

The Master equation of the system can be written as:

$$\begin{aligned} \dot{\rho} = & \frac{-i}{\hbar}[H, \rho] + \Gamma_{12}L(\sigma_{12}^-)\rho + \Gamma_d L(\sigma_{23}^z)\rho + \Gamma_{23}L(\sigma_{23}^-)\rho \\ & + \Gamma_{31}L(\sigma_{31}^+)\rho + \kappa L(a)\rho + \kappa_1 L(a)\rho \end{aligned} \quad (3.3)$$

where κ and κ_1 indicate the coupling rate of the cavity to the dissipative environment and the waveguide, respectively. Γ_d and Γ_{23} are the atomic dephasing and decay rates, $\Gamma_{12} = 5\kappa_1$ is the fast decay term from the intermediate level and Γ_{31} is the incoherent pumping rate of the intermediate level described by a Gaussian pulse with 20 ps temporal width and an amplitude of $0.1\kappa_1$.

In the first series of simulations the time-resolved dynamics of the expectation value of the excited state population of the QD has been calculated by solving the time-dependent equation of the motion for the density matrix of the system and the results are shown in figure 3.8. We assume that the QD is in state $|3\rangle$ in $t = 0$. 2-3 transition and cavity mode has been assumed to be in resonance. At first, applying the CW resonant laser drives the 2-3 transition and we see the corresponding Rabi oscillations, which after some time damp and bring the population to an equilibrium value that depends on the intensity of the resonant laser and on the decay channels present in the system. In this calculation we only considered one dissipative channel, namely the coupling of the cavity to the waveguide. When the quasi-resonant pulse is sent to the system (after 3 ns), the system is brought to the excited state and with higher power of the CW resonant laser it experiences a faster ($n + 1$ times, where n is the number of photons per cavity lifetime sent via resonant laser) initial decay and subsequent Rabi oscillations which is the result of increased interaction between the CW resonant laser field and the atom and indicates the stimulated emission (the decay time has been defined as the time needed for the population of the excited state to decrease to 20% of its maximum value).

The black plot in this figure shows a situation where the incident stimulating power is very low (0.05 photons per cavity lifetime) and the atomic decay is close to its value when no resonant field drives the cavity. By increasing the power of the resonant laser (blue: 0.5 photons per cavity lifetime) we observe a faster initial decay and appearance of the Rabi oscillations. By increasing the resonant stimulating power (red: 1 photons per cavity lifetime) the initial decay time decreases more and more Rabi fringes appear. This regime can be best described by the coherent exchange of photons between atom and the stimulating field.

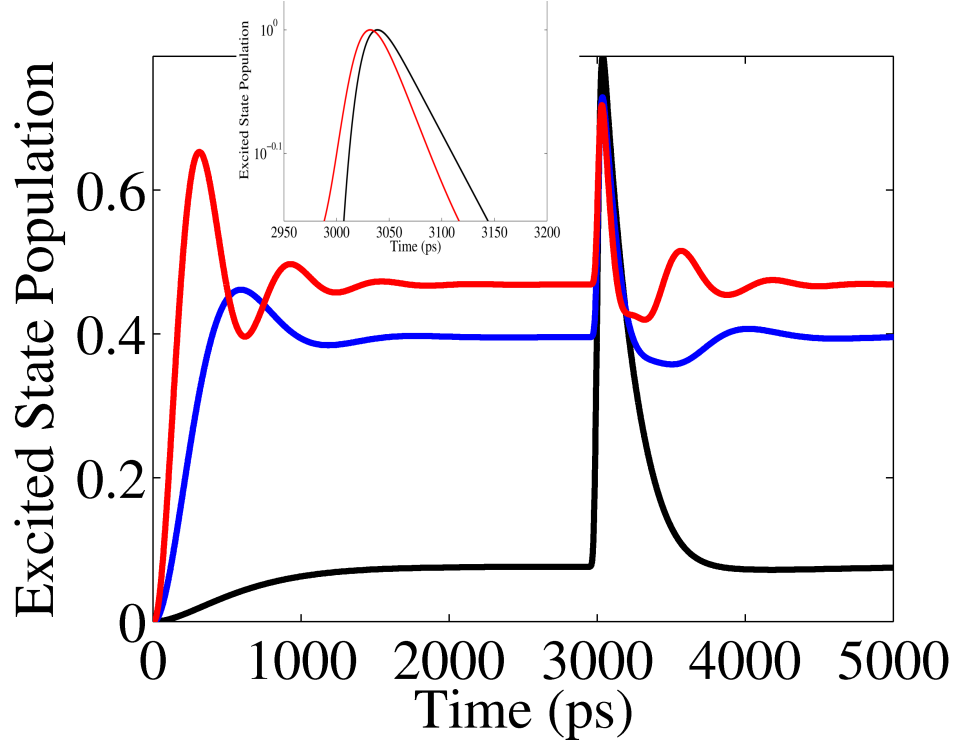


Figure 3.8: Time-resolved dynamics of emission of the QD when stimulated by a low intensity CW laser. The decay time of the cavity to the waveguide has been assumed to be around 10 ps, $g = 0.1\kappa_1$, $\Gamma_{12} = 5\kappa_1$ and all other lossy channels have been neglected. 2-3 transition and cavity mode has been assumed to be in resonance. Different colors indicate different intensities of the resonant laser applied to the system. Inset: the logarithmic plot of the black and red plot which shows the decrease in initial decay time better. (Black: 0.05, blue: 0.5 and red: 1 photons per cavity lifetime intensity of the stimulating CW laser)

In order to have a realistic simulation of the phenomenon as it happens in our solid-state system we include the term responsible for the dephasing of the QD (figure 3.9), which is usually present in solid-state systems due to the electrostatic fluctuations and interaction with the phononic bath. In these simulations the power of the CW resonant laser is one photon per cavity lifetime and the only dissipative channels are coupling of the cavity to the waveguide and the dephasing channel ($\Gamma_d = \kappa_1$ (black), $\Gamma_d = 0.1\kappa_1$ (blue) and $\Gamma_d = 0.01\kappa_1$ (red)). As it is expected the presence of the dephasing washes out the coherent oscillation between stimulating field and the atom and increases the required

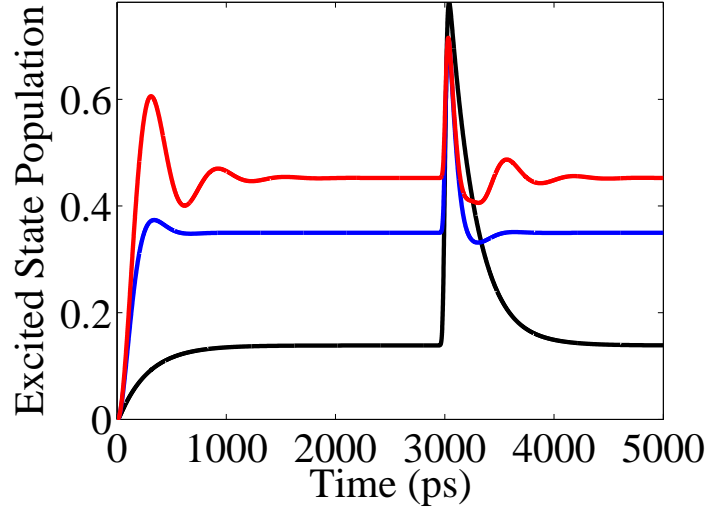


Figure 3.9: Effect of the dephasing of the QD on the observed dynamics. Different colors indicate different values of the dephasing rate. The decay time of the cavity to the waveguide has been assumed to be around 10 ps, $g = 0.1\kappa_1$, $\Gamma_{12} = 5\kappa_1$ and atomic decay to the environment (Γ_{23}) has been neglected. ($\Gamma_d = \kappa_1$ (black), $\Gamma_d = 0.1\kappa_1$ (blue) and $\Gamma_d = 0.01\kappa_1$ (red), and κ_1 is the coupling rate of the cavity to the waveguide. 2-3 transition and cavity mode has been assumed to be in resonance. The stimulating laser has an average photon number of one per cavity lifetime.)

power of incident field for the stimulation. For realistic best values of the dephasing time in our QDs (around 100 ps which corresponds to the blue plot) we have calculated the first initial decay time for different powers which shows the reduction of the initial atomic lifetime by increasing the CW resonant laser power, hence the possibility of observing time-resolved signature of stimulated emission in our system as indicated in figure 3.10.

3.4 Conclusion

In this chapter the Master equation has been solved numerically in order to get insights into the dynamics and feasibility of nonlinear effects at the single-photon level, namely two phenomena of dipole-induced reflection and stimulated emission. It has been shown that achieving dipole-induced reflection with our current system is demanding. By assuming realistic values for the parame-

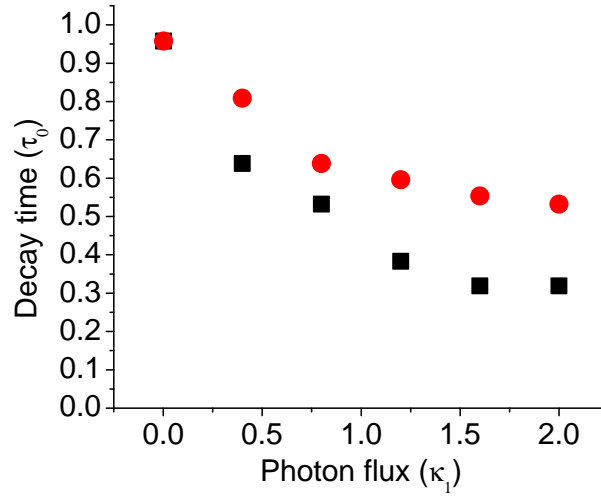


Figure 3.10: Plot of the initial decay time of the QD normalized to unstimulated decay time as a function of the photonic flux. The decay time of the cavity to the waveguide has been assumed to be around 10 ps, $\Gamma_d = 0.3\kappa_1(0)$ for red circles (black squares), $g = 0.1\kappa_1$, $\Gamma_{12} = 5\kappa_1$ and the atomic decay to the environment (Γ_{23}) has been neglected. κ_1 indicates the coupling rate of the cavity to the waveguide. 2-3 transition and cavity mode has been assumed to be in resonance.)

ters of the system the feasibility of the observation of the stimulated emission effect in our system has been demonstrated.

Efficient Coupling of Light into a Photonic Crystal

For the successful realization of the quantum photonic integrated circuit (QPIC), efficient coupling of light into the circuit and between different units of the circuit is of paramount importance. As discussed previously photonic crystals are one of the best candidates for control of the emission from single-photon emitters and realization of processing units in a QPIC, but they typically suffer from high propagation losses. This indicates the necessity of efficient coupling of light between PhC and conventional low-loss waveguides, and with the outside world. In this chapter some techniques which have been used to achieve this goal during the course of this work are discussed. They include an interface between a nanobeam and a photonic crystal waveguide (PhCWG), grating couplers for efficient coupling of PhCWG to the top and anti-reflection (AR) coatings for the suppression of the Fabry-Perot (FP) oscillations at the two end facets of a ridge waveguide (RWG). The use of a PhC cavity as an on-chip filter of the single QD emission is also presented.

4.1 Design of photonic crystal waveguide-nanobeam interface for efficient coupling of light

PhCWGs are one the most versatile photonic elements for the realization of the QPIC and a variety of their applications has been theoretically anticipated and experimentally demonstrated [119, 120, 36]. Another important element of a QPIC is a RWG that can be realized with low losses for efficient transport of light inside the QPIC and coupling of light to the outside world. In this section

we consider the design of an interface between a PhCWG and a nanobeam to achieve efficient coupling of the light between them. Coupling of light from the nanobeam to RWG will be discussed in chapter 5. The simulations performed in this section are 2D finite element method simulations performed with the COMSOL 3.5a software and are carried out by J. F. P. Schouwenberg as a part of his Bachelor thesis work.

The structure considered here is a triangular PhC structure of GaAs where by removing the middle row of holes we create a PhCWG and this PhCWG is coupled to a GaAs nanobeam. Direct coupling of the two structures will result in considerable loss due to scattering and reflection at the interface. This is due to the spatial mode profile mismatch related to the difference in the width. In order to reduce this mismatch and consequently the losses we proposed a design based on adiabatic theorem [121, 122, 123] which states that a system can remain in its eigenstate in the presence of a perturbation only if the perturbation is introduced gradually. Based on this strategy [124] we propose a solution based on two main ideas: first choosing the same waveguide width for the two structures and second gradually increasing the air contribution of the PhCWG in the transition region between the PhCWG and the nanobeam.

The result of the transmission of the TE-mode of the light versus its wavelength for different proposed designs is plotted in figure 4.1. While with the direct coupling a transmission below 50% is obtained in the considered frequency region, introducing air holes in a funnelled way increases this value up to 60%. By applying a tapering in the radii of the holes in the transition region the transmission increases to 80%. By optimizing the tapering almost unity transmission is obtained. The optimized parameters of this tapering are as follows: 7 holes have been introduced into the transition region, the radius of each hole is successively reduced in steps of $0.115r_0$, where r_0 is the radius of the holes in PhC and finally the width of the nanobeam is chosen equal to $2a\sqrt{3}$, where a is the lattice constant of the PhC.

4.2 Design of the photonic crystal cavity as an on-chip filter

One of the most important functionalities needed for the realization of the QPICs is the ability to perform on-chip filtering of the emission of a single-photon emitter which can be used for variety of applications including on-chip

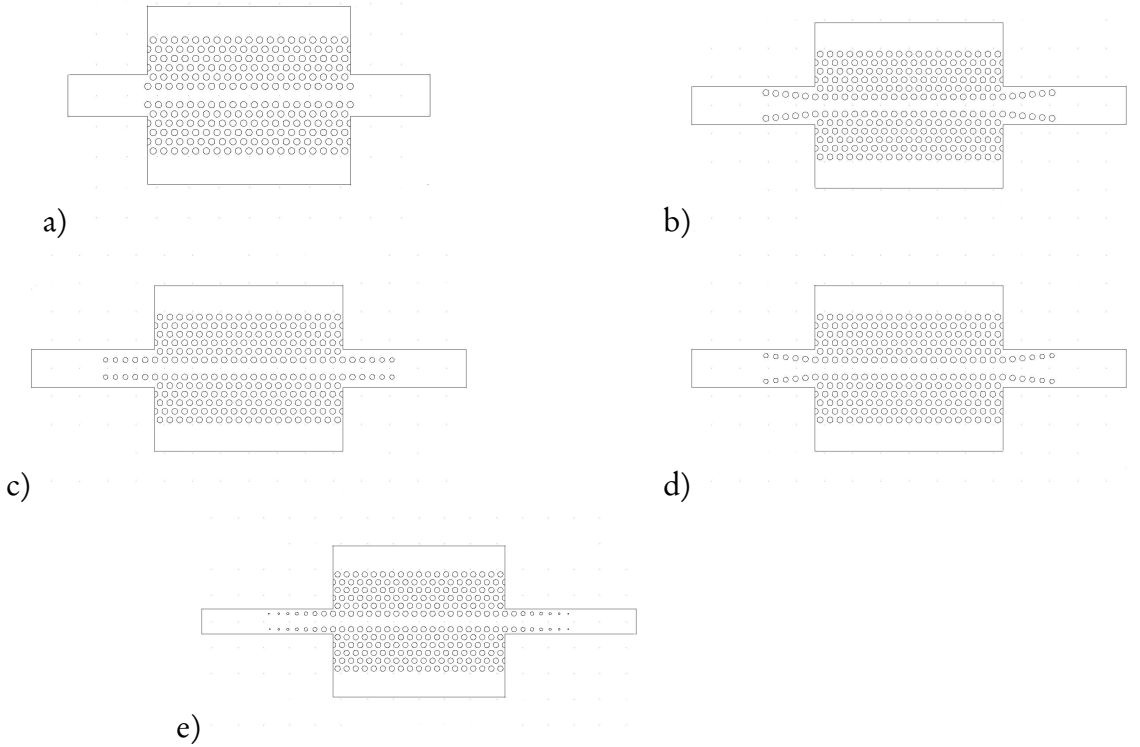
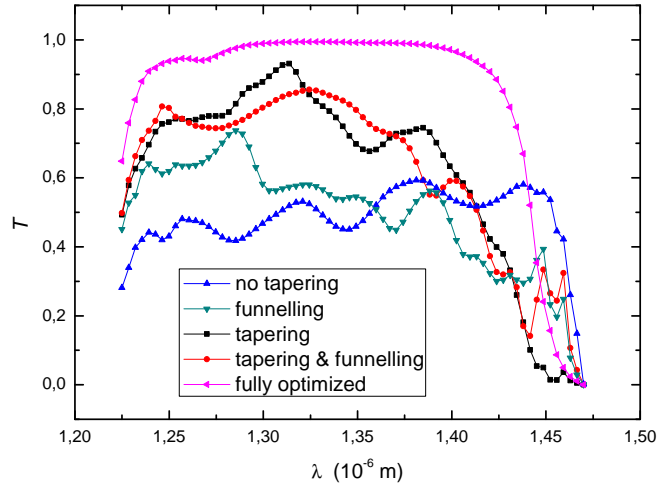


Figure 4.1: Transmission of light through coupled PhCWG-nanobeam device versus wavelength for different design structures: (a) normal, (b) funnelling, (c) tapering, (d) funnelling tapering, (e) optimal tapering

interference of single photons. A coupled PhCC-PhCWG system has been theoretically and experimentally investigated and proposed as a system capable of realizing the filtering functionality [125, 126, 127, 128, 129]. Here we use a configuration known as direct (in-line) coupling between a L3 PhCC (obtained by removing the first three holes from the center of the PhC) and a PhCWG. Two holes have been left as connecting barriers between the PhCC and the input and the output PhCWGs. When the wavelength of the input light matches the wavelength of the cavity, light can pass through the cavity by resonant tunnelling. This filter is called two-port resonant tunnelling transmission filter.

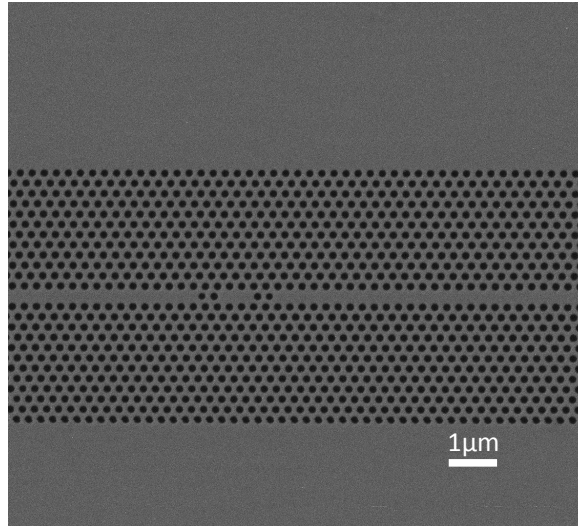


Figure 4.2: SEM picture of the realized on-chip filter, where a L3 cavity is coupled to a PhCWG and consequently coupled to a RWG.

The performance of this filter can be described by coupled-mode theory [46, 105]. The coupling of the cavity to the PhCWG and to the leaky radiation modes can be characterized by quality-factors Q_{wg} and Q_r , where the total quality factor Q_T is obtained as:

$$\frac{1}{Q_T} = \frac{1}{Q_{wg}} + \frac{1}{Q_r}. \quad (4.1)$$

This results in the following equation for the transmission of light from the

input to the output PhCWG [127]

$$T = \left(\frac{Q_T}{Q_{wg}} \right)^2 = \left(\frac{1}{1 + \frac{Q_{wg}}{Q_r}} \right)^2. \quad (4.2)$$

This formula indicates that for a fixed Q_r (which depends on the design and fabrication of the cavity), increasing the transmission requires a decrease of the Q_{wg} , which will increase the bandwidth of the filter thus deteriorating the filtering functionality. Thus for achieving the optimum performance a trade-off between the transmission and bandwidth should be achieved.

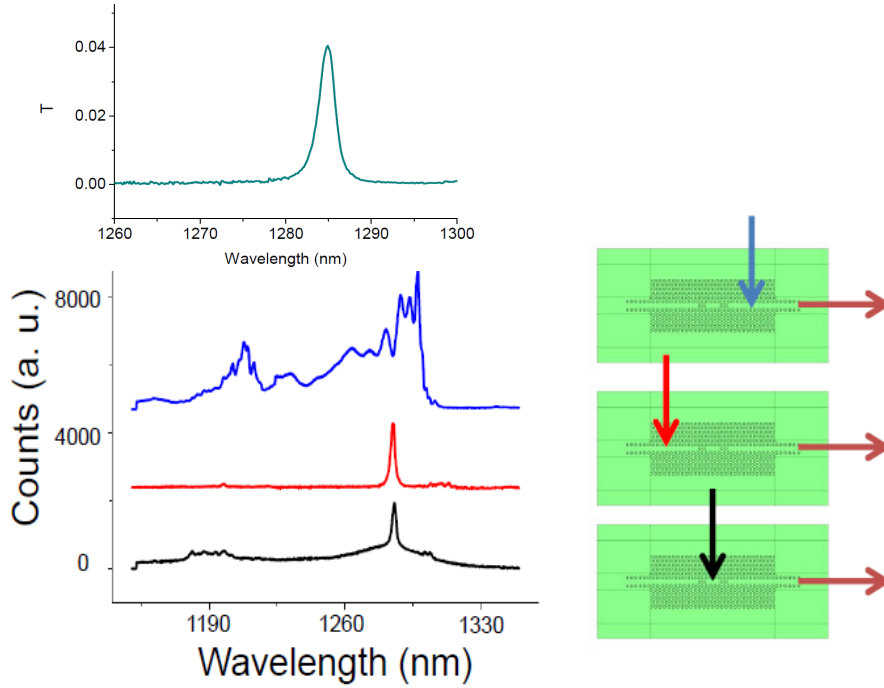


Figure 4.3: Demonstration of the filtering with the cavity mode by applying non-resonant laser (780 nm) from the top and collecting from the side (with $10 \mu\text{W}$ power and 1, 5 and 10 seconds acquisition times for the blue, black and red plots). Blue: after, red: before and black: inside PhCC. Green (top) plot shows the transmission through the filter (from the input to the output PhCWG in the spectral region around the cavity mode) obtained by dividing the red curve by the blue curve. Offset is for clarity.

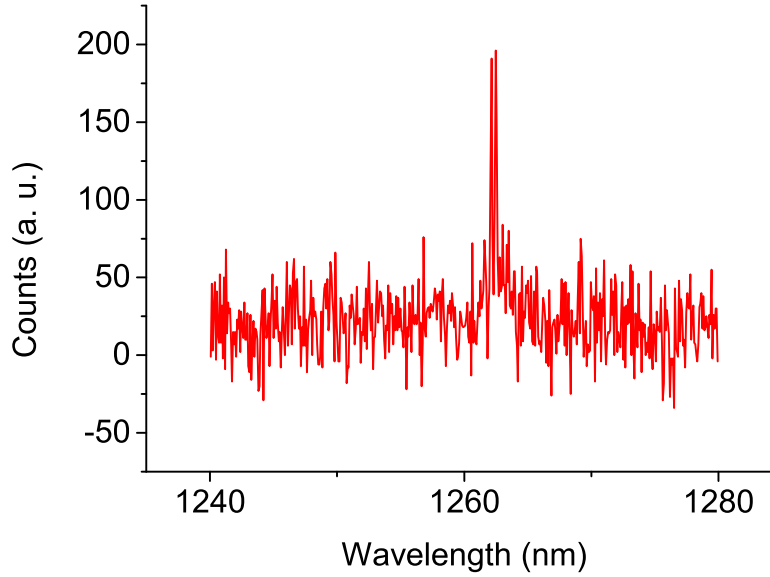


Figure 4.4: Filtering of single QD lines by applying laser before the PhCC and collecting from the side. Non-resonant CW laser (780 nm) with 20 nW power has been applied before the cavity for 120 seconds. Measurement performed by Dr. T. B. Hoang.

An example of the structures realized with aforementioned design can be observed in figure 4.2. Here the radius of the second hole of the in-line L3 cavity is reduced 10% with respect to the first hole [130]. In figure 4.3 the filtering functionality has been demonstrated where by applying a non-resonant laser (780 nm) from the top, on the two sides of the cavity (blue and red) and on top of it (black) the photoluminescence collected from the side has been recorded. Here our PhCC-PhCWG system is coupled to a RWG and the signal is collected from the cleaved end facet of the RWG. The details of this coupling will be given in chapter 5. The blue curve shows the slow light mode of the PhCWG and in the black and red plot we observe the filtered cavity mode which is located close to the slow light mode of the PhCWG. When the light is applied inside the PhCC, the cavity wavelength shows a slight shift (~ 0.2 nm) due to the heating effect of the laser which redshifts the PhCC wavelength. Also, more background emission compared to the case where the laser is applied before the PhCC (red plot) is observed due to the excitation of PhCWG section around the cavity (since our laser spot is bigger than the area of the cavity). The

Q-factor of the cavity is around 1300 which indicates a filter bandwidth of ~ 1 nm.

Here considering the experimental values of the Q-factors ($Q_{loaded} \simeq 1300$ and $Q_{unloaded} \simeq 2000$) and by using equation 4.2, transmission through the cavity can be estimated to be around 4% which is in good agreement with the measured value shown in the figure 4.3. This value can be improved by better fabrication quality and optimized design [131].

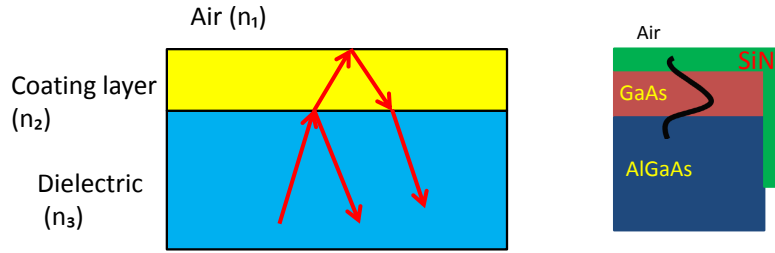


Figure 4.5: Schematic of the AR coating method where a thin layer of dielectric (yellow) is deposited between the dielectric material and the air (left) and material layers in our AR coated samples, where a layer of SiN (green) is deposited on top of the devices (GaAs (brown)/AlGaAs (dark blue) RWGs) to suppress the reflections at the cleaved facet (right).

Finally in order to show the applicability of the on-chip filter for filtering the single-photon emission of the QDs used for on-chip single-photon experiments we demonstrated the filtering of single QDs by our device. In figure 4.4 we see the filtering of the single QDs (by exciting the PL from the top before the cavity with a non-resonant (780 nm) laser with 20 nW power and 120 seconds acquisition time and collecting from the side). In this case two single QD lines were observed which indicates the relatively high density of QDs in this sample.

4.3 Anti-reflection coating for suppression of the reflection at ridge-waveguide cleaved end facets

When light is sent through a cavity with reflecting mirrors the transmission as a function of the wavelength shows peaks of high transmission for certain wavelengths. This phenomenon, which is due to the interference of the light reflected from the mirrors, is known as Fabry-Perot (FP) oscillations and can have detrimental effect in many cases for example in optical amplifiers. In the framework of this thesis, FP oscillations are a source of problem in that they may mask the spectral features related to dipole-induced reflection effect (see chapter 5). A couple of different methods including tilting of the RWGs and deposition of anti reflection (AR) coating materials [132, 133] have been proposed to suppress these reflections. In this work we used AR coating as the solution to overcome FP oscillations, since the multi-mode nature of our RWGs (typically with $5 \mu m$ width) makes the determination of the parameters needed for the tilting solution very difficult [134].

Figure 4.5 (left) illustrates the function of the AR coating layer where a layer of material with refractive index n_2 and thickness of d is deposited between the two dielectric materials of refractive index n_1 (here $n_1 = 1$ is considered to be air) and n_3 (the right figure shows the schematic of AR coated samples used in this work). By writing the boundary conditions in the interfaces and after some algebra [135], for the case of normal incidence, for the reflection coefficient at the interface of the materials with refractive indices n_2 and n_3 we have:

$$R = \frac{n_2^2(n_1 - n_3)^2 \times \cos^2(k_0 b) + (n_1 n_3 - n_2^2)^2 \times \sin^2(k_0 b)}{n_2^2(n_1 + n_3)^2 \times \cos^2(k_0 b) + (n_1 n_3 + n_2^2)^2 \times \sin^2(k_0 b)}, \quad (4.3)$$

where k_0 is the wavenumber in free space and $b = 2n_2 d \cos(\theta)$, where θ is the propagation angle in the AR coating layer with respect to the normal and d is the thickness of the coating layer.

This formula can be simplified when $k_0 b = \frac{\pi}{2}$ which means $d = \frac{\lambda_0}{4n_2}$:

$$R = \frac{(n_1 n_3 - n_2^2)^2}{(n_1 n_3 + n_2^2)^2}, \quad (4.4)$$

and interestingly reflection goes to zero when $n_2^2 = n_1 n_3$. The AR coating layer causes destructive interference between the reflected and constructive

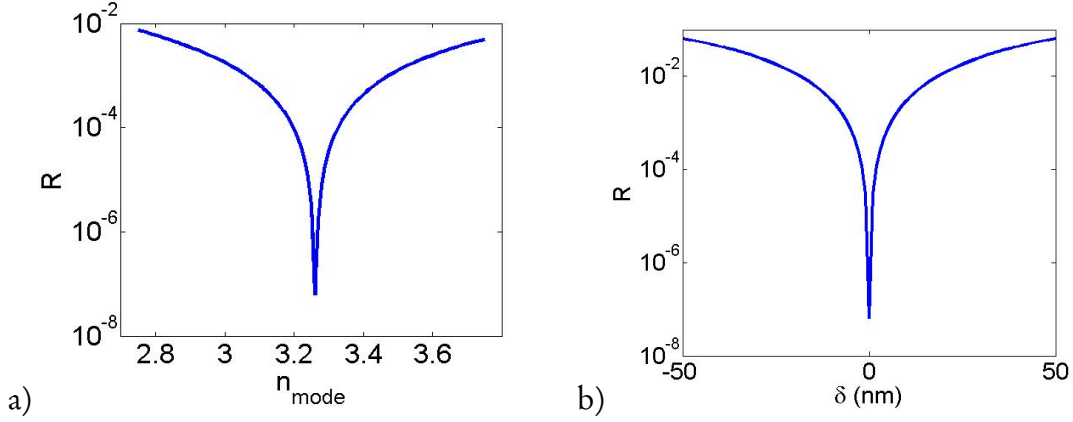


Figure 4.6: Plot of the reflection coefficient versus (a) refractive index of the first order mode of the RWG with $t_{AR} = \frac{\lambda_0}{4n_{AR}}$ and $n_{AR} = 1.806$, (b) deviation of the thickness of the coating layer from the optimized value ($\delta = t - \frac{\lambda_0}{4n_{AR}}$) where $n_{AR} = 1.806$ and $n_{mode} = 3.26$.

interference between the transmitted beams. While our physical system is constituted by a ridge waveguide with a layer of SiN deposited on the facet (see right part of the figure 4.5), we approximate it as a tri-layer system using the effective-medium approach (a more precise calculation may be realized by 3D finite-element simulations). Based on formula 4.3 by considering the optimal value of the AR coating layer thickness ($d = \frac{\lambda_0}{4n_2}$, where $\lambda_0 = 1300$ nm and $n_2 = n_{SiN} = 1.806$ which is the effective refractive index of our SiN as AR coating layer, measured by ellipsometry), we have plotted the reflection coefficient as a function of the n_{mode} (effective refractive index of the fundamental RWG mode) shown in figure 4.6a. By fixing the n_{mode} at the optimum value obtained from this figure ($n_{mode} = 3.26$) we have plotted the reflection coefficient versus the deviation of the AR coating thickness from the optimized value ($\frac{\lambda_0}{4n_2}$, where $\lambda_0 = 1300$ nm) in figure 4.6b. As it can be evidenced from this figure the reflection coefficient has a value of $R < 10^{-2}$ for errors around 30 nm which is within the precision that can be obtained by PECVD deposition (≈ 10 nm).

As mentioned our AR coating material is a layer of SiN deposited by PECVD at 100°C (due to uniform deposition of SiN in every direction, it follows the shape of the sample and is deposited also on the cleaved facets) with $n = 1.806$, which has a good value for satisfying the relation between refractive indices for

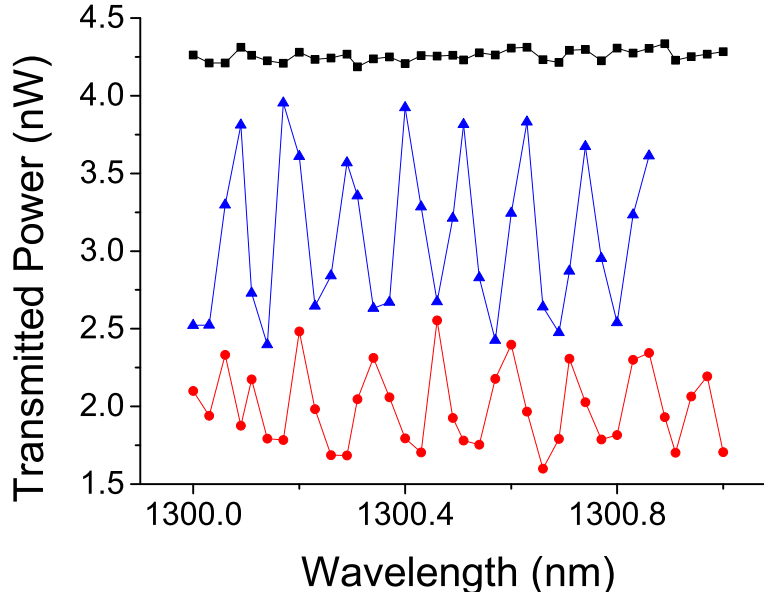


Figure 4.7: Plot of the transmission versus wavelength through a (320 nm) GaAs / (1.5 μm) RWG (with width equal to $w = 4 \mu\text{m}$) without AR coating (blue), with 77 nm SiN layer (red) and with 168 nm SiN layer (black). The length of the RWGs is equal to $L = 1.8 \text{ mm}$. The SiN layer thicknesses have been measured with focused ion beam microscopy. Offset is for clarity.

the suppression of the reflection. Figure 4.7 shows the result of the transmission measurement versus the wavelength of the light through RWGs where no AR coating was applied (blue), with 77 nm (red) and 168 nm (black) SiN layer thickness which is close to the value of $\frac{\lambda}{4n} = 180 \text{ nm}$.

As it can be observed the reflection at the two cleaved end facets and consequently the contrast of the FP fringes has been reduced noticeably comparing to the case where no AR coating was applied. It is possible to calculate the reflection coefficient from the contrast of the fringes by knowing the length $L = 1.8 \text{ mm}$ and typical loss of our RWGs $\alpha = 5 \text{ cm}^{-1}$ (detailed calculation is discussed in chapter 5) [136] which will lead to $R = 28\%$ for the case with no AR coating (blue) and $R = 20\%$ for the case with 77 nm thick SiN layer and $R < 7 \times 10^{-3}$ for the case with 168 nm thick SiN layer (calculated by considering the contrast to be equal to the difference between the highest and the lowest transmission). It is also possible to extract the effective refractive index of the mode from the

spectral distance between the fringes (more explanation given in section 5.1) which in this case gives a value equal to $n_{mode} \simeq 3.35$.

4.4 Grating couplers for efficient coupling of light from the photonic crystal cavity to the top

As mentioned earlier the coupling of the light from the QPIC to the outside world is an important issue to be addressed for realization of QPICs. While in most of this thesis end-fire coupling from the side is used, another possible approach is the use of grating couplers to couple light from a photonic structure to the top and vice versa [137, 138, 139]. The grating coupler is basically a Bragg grating which is used to couple light from free space into a waveguide and from the waveguide into free space.

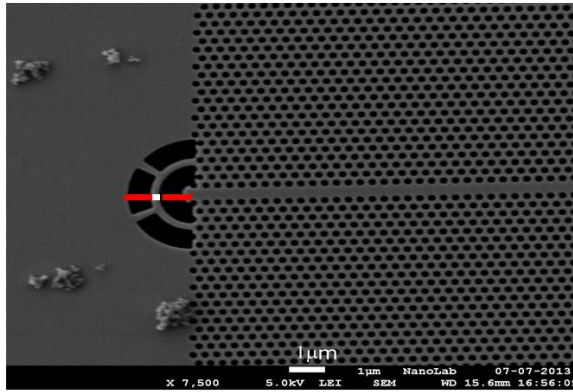


Figure 4.8: SEM picture of the grating coupler realized for coupling light from the PhCWG to the top. The length of the red lines and the white line is chosen equal to $\frac{\lambda}{2}$ and $\frac{\lambda}{2n}$ in design, respectively. $\lambda = 1300$ nm is the wavelength of the incident light and n has been considered to be equal to the refractive index of GaAs.

In this part of the work, following [107], we used a circular grating cou-

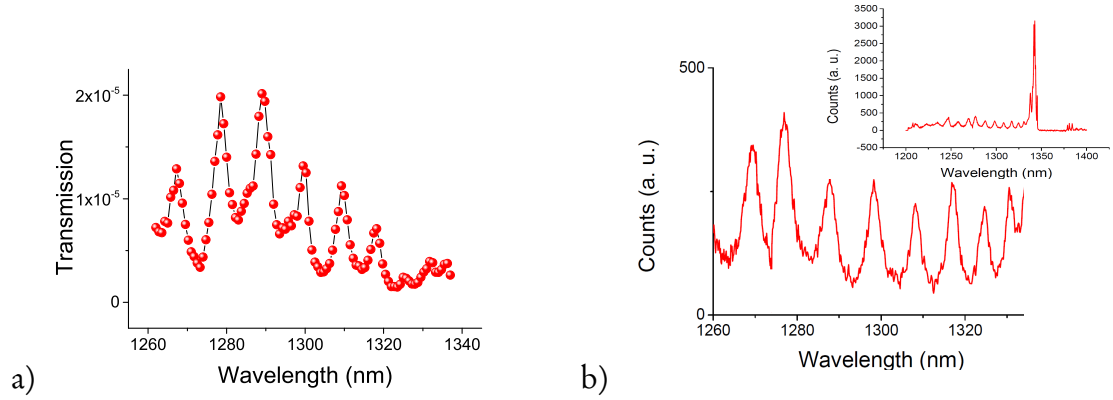


Figure 4.9: (a) Transmission from a PhCWG coupled to a grating coupler from the top, (b) microPL generated by applying non-resonant laser (780 nm with $10 \mu W$ power for 2 seconds) to the PhCWG from the top and collected from the cleaved end facet of the PhCWG. Inset shows the entire range of the acquired spectrum.

pler to couple the light from a PhCWG to the top. This grating is made of a $\frac{\lambda}{2n} = 190$ nm wide circular nanobeam (where λ is the wavelength of the incident light assumed to be $\lambda = 1300$ nm and $n = 3.4$ has been considered to be equal to the refractive index of GaAs) spaced by $\frac{\lambda}{2} = 650$ nm from the end of the PhCWG and from the other GaAs facet. A SEM picture of the realized grating is shown in figure 4.8. Next we coupled the light from the side by the help of an objective with $NA=0.42$ to the cleaved end facet of the PhCWG and collected the light coupled to our objective ($NA=0.5$) from the top. The result of this measurement is presented in figure 4.9a. Here we see the fiber to fiber transmission where the input fiber is coupled from the side (via an objective) to the cleaved facet of the PhCWG and the output fiber collects the light coupled to the top objective as a function of the wavelength. The observed FP fringes correspond to the reflection at the cleaved end facet of PhCWG and the facet terminated by the grating coupler. In figure 4.9b the result of the microPL measurement (obtained by applying the 780 nm laser from the top and collecting the PL from the cleaved end facet) is recorded. A qualitative agreement can be seen between the PL and transmission measurement, where the peaks on the blue side of the slow light mode of the PhCWG correspond very well between the two measurements. Close to the slow light mode of the PhCWG, increased losses [140, 141] reduce the intensity detected by the coupler.

In order to calculate the coupling efficiency of our grating coupler (figure 4.10-top), in the same fabrication process we realized two other different structures: RWG-PhCWG-RWG and RWG-PhCWG systems (where one facet is cleaved in RWG and the other in PhCWG). The schematic of these two kinds of design is drawn in figure 4.10 (middle and bottom). The transmission for each kind of structure is calculated by integrating the transmission over a wavelength interval far from slow light region (1260-1320 nm) of the PhCWG averaged for 4 nominally identical devices. In this way we obtained transmission values (fiber to fiber) for these two kinds of structures as: $\overline{T}_{RP} = \overline{\eta}_R^2 \times \overline{\eta}_{RP}^2 = (4.23 \pm 0.06) \times 10^{-4}$ and $\overline{T}_P = \overline{\eta}_R \times \overline{\eta}_P \times \overline{\eta}_{RP} = (1.7 \pm 0.1) \times 10^{-5}$, where $\overline{\eta}_R$, $\overline{\eta}_P$ and $\overline{\eta}_{RP}$ indicate the coupling efficiency from the fiber to the center of the RWG, the coupling efficiency from the center of the PhCWG to the fiber and the coupling efficiency between the center of the RWG and the center of the PhCWG, respectively (see figure 4.10). By measuring the spectral average of the fiber to fiber transmission in the structures with grating couplers over the same spectral range and averaging it over 4 nominally identical devices we obtained $\overline{T}_G = \overline{\eta}_G \times \overline{\eta}_P = (8.52 \pm 0.09) \times 10^{-6}$ ($\overline{\eta}_G$ is the coupling efficiency between the center of the PhCWG (via grating coupler) to the fiber coupled to the top objective) which gives the coupling efficiency from the center of the PhCWG to the fiber coupled to the top objective equal to $\overline{\eta}_G = \frac{\overline{T}_G \times \sqrt{\overline{T}_{RP}}}{\overline{T}_P} \simeq 0.0100 \pm 0.0005$ which is close to the coupling efficiency obtained for similar structures [107]. We note that theses relatively small error bars do not take into account possible variations from chip to chip and should not be taken as an indication of the reproducibility of the efficiency value. By similar procedure the coupling efficiency from the center of the PhCWG to the fiber coupled from the side (cleaved PhCWG end facet) can be estimated to be around 2×10^{-3} which indicates the efficiency of the grating coupler approach.

4.5 Conclusion

In this chapter several methods for coupling light efficiently from and to the PhC structures have been investigated. An optimal design for the efficient coupling of light between a nanobeam and a PhCWG has been proposed and almost unity theoretical efficiency with the proposed design has been obtained. By coupling a L3 PhCC coupled in-line to a PhCWG an on-chip filter has been realized and filtering of single QD lines through it has been observed. By depositing SiN

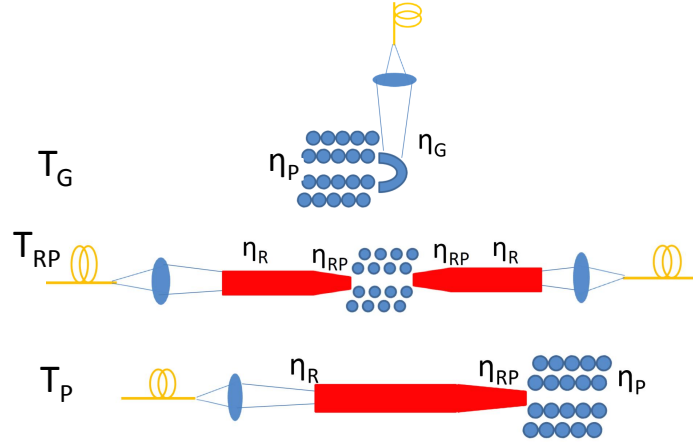


Figure 4.10: Sketches of the three different structures measured for determining grating coupler's efficiency. η_R , η_P , η_G and η_{RP} indicate the coupling of the fiber (yellow) to the center of the RWG (red), the coupling of the center of the PhCWG (blue) to the fiber, the coupling of the center of the PhCWG coupled to the fiber via grating coupler and the coupling between the center of the RWG and the center of the PhCWG, respectively. Transmission through the first, second and the third system are denoted as T_G , T_{RP} and T_P in the text.

layer as an AR coating layer at the RWG facet the contrast of the FP fringes in the transmission has been reduced which has important applications for obtaining a visible signal in dipole-induced reflection measurement (discussed in chapter 3). Finally a circular grating coupler for the efficient coupling of the light between the PhCWG and the top objective has been proposed, realized and the transmission through PhCWG coupled to the top by this grating has been measured. The results presented in this chapter are important technological progresses toward the successful realization of a QPIC.

Single-Photon Transmission through A Coupled Ridge waveguide-Photonic crystal Cavity System

In this chapter the efficient coupling of single photons emitted by single quantum dots (QDs) in a photonic crystal cavity (PhCC) to a ridge waveguide (RWG) are demonstrated. Using a single-step lithographic process with an optimized tapering, up to 70% coupling efficiency between the photonic crystal waveguide (PhCWG) and the RWG was achieved. The emission enhancement of single QDs inside an in-line PhCC coupled via the RWG to a single-mode fiber was observed. Single-photon funnelling rates around 3.5 MHz from a single QD into the RWG were obtained. This result is a step toward the realization of a fully functional quantum photonic integrated circuit. In the second part of the chapter the feasibility of the demonstration of dipole induced transparency and technological progress toward that goal has been discussed. Section 5.1 of this chapter has been published in [142].

5.1 Funnelling single photons into ridge-waveguide photonic integrated circuits

As mentioned previously, single photons are one of the most promising candidates for the implementation of quantum computation and quantum simulation, due to their low decoherence [9, 98, 69]. On-demand and on-chip generation and control of single photons are the main issues to be addressed for this purpose. Semiconductor quantum dots (QDs) have attracted consider-

able attention as single-photon sources because of their potential for integration with a semiconducting photonic integrated circuit [27]. The integration of QDs with photonic crystal (PhC) structures has been previously addressed and important functionalities such as efficient coupling of the emission of single QDs into PhC cavities (PhCCs) and waveguides (PhCWGs) have been demonstrated [143, 106, 144, 145, 146, 147, 148, 26, 25]. Recently, approaches to reproducibly control the exciton and cavity energy on chip, as needed to realize a scalable circuit, have been developed [149, 23, 150]. However, quantum photonic integrated circuits cannot be practically implemented with these suspended structures due to their low mechanical stability and high optical loss. Although ridge waveguides (RWG) are widely used for low-loss, on-chip transmission [151], and their coupling with photonic nanostructures has been studied [152, 153, 154], the efficient coupling of single photons from a single QD in a PhCC to a RWG has not been addressed. In this chapter a design to overcome the mode mismatch between the RWG and the suspended PhC structure has been proposed and its efficiency has been demonstrated by transmission measurement and the detection of single photons at the end of the RWG.

Our approach is shown in figure 5.1a and consists of a first transition between the PhCWG and a suspended nanobeam (SNB), whose width is then adiabatically increased to the typical width ($3 - 5 \mu\text{m}$) of a RWG. The PhCWG and the SNB are fabricated from a GaAs/AlGaAs heterostructure by reactive ion etching of the AlGaAs sacrificial layer. When the width of the SNB exceeds twice the lateral extent of AlGaAs etching, a supporting post is left and the structure evolves towards a conventional RWG [152] (see the cross-sectional scanning-electron microscope (SEM) image in figure 5.2a). In order to maximize the coupling efficiency between the PhCWG and the SNB [124], the width of the SNB is chosen equal to $2a\sqrt{3}$ where a is the lattice constant of the PhC, five more holes are inserted in the SNB in continuation of the two inner hole rows of the PhCWG and their radii are tapered down in 10nm steps (figure 5.1a). As discussed in 4.1 this design provides a calculated 97% coupling efficiency between PhCWG and SNB.

We then calculated the coupling efficiency between SNB and RWG. Our RWG consists of a $4 \mu\text{m}$ wide and 320 nm thick slab of GaAs on top of a $\text{Al}_{0.7}\text{Ga}_{0.3}\text{As}$ sacrificial layer with $2.7 \mu\text{m}$ width and $1.5 \mu\text{m}$ thickness. The shape of the AlGaAs sacrificial layer in the simulation is considered according to the measured etching profile. We assume a SNB with 320 nm thickness and $2a\sqrt{3}$ width (with $a = 320 \text{ nm}$). The fundamental transverse electric guided

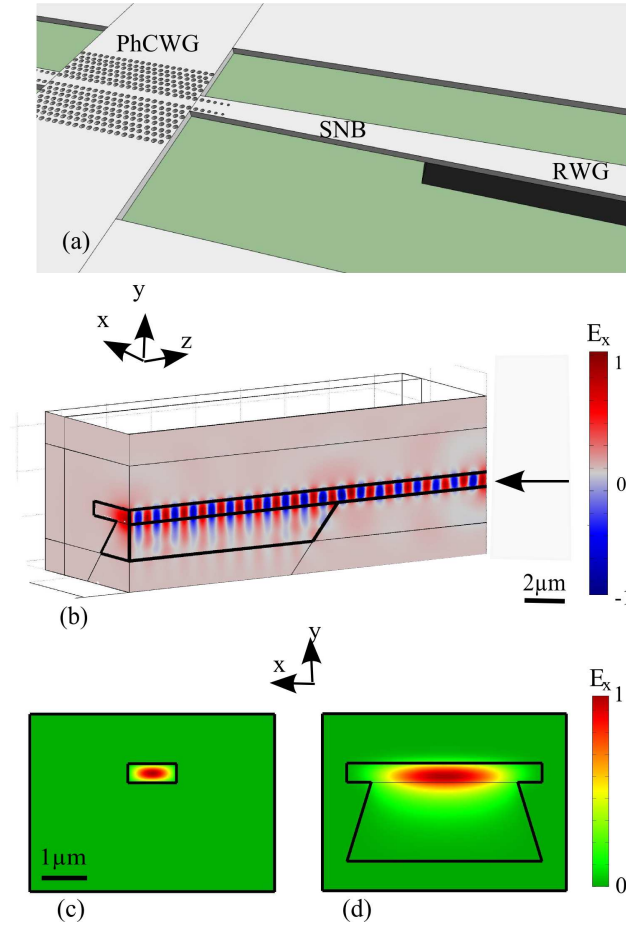


Figure 5.1: (a) A sketch of the design where the interface between SNB, PhCWG and RWG is shown, (b) Evolution of the normalized transverse-electric guided mode at the interface between SNB and RWG. The arrow indicates the input port used for calculation of the transmission in the structure, (c) and (d) Normalized transverse-electric guided mode profile at the entrance of the SNB and RWG respectively.

modes of the RWG and the SNB have been simulated (figure 5.1c,d). A clear mode mismatch between the two modes is observed in both the lateral and vertical directions which would result in poor coupling efficiency if the two structures were coupled directly. Instead the tapering of the SNB width and of the supporting post ensures an adiabatic transition. Figure 5.1b illustrates the evolution of the transverse electric guided mode at the interface between the SNB and the RWG. The parameters considered here are the same as in figure

5.1c,d except that the length of the taper and the initial width of the RWG are $10\ \mu\text{m}$ and $3\ \mu\text{m}$ respectively, due to computational limitations. These calculations show that about 98% of the power is transmitted from the SNB to the RWG. We note that this tapered transition can be realized with a single step of lithography and etching, without the need for a critical realignment.

The layer stack and fabrication of the devices is done according to the recipe introduced in chapter 2. The resulting devices are shown in figure 5.2a and b. In all the experiments described below, the initial width of the SNB is set to $2a\sqrt{3}$ and it is tapered to a RWG width of $4\ \mu\text{m}$ at the cleaved facet.

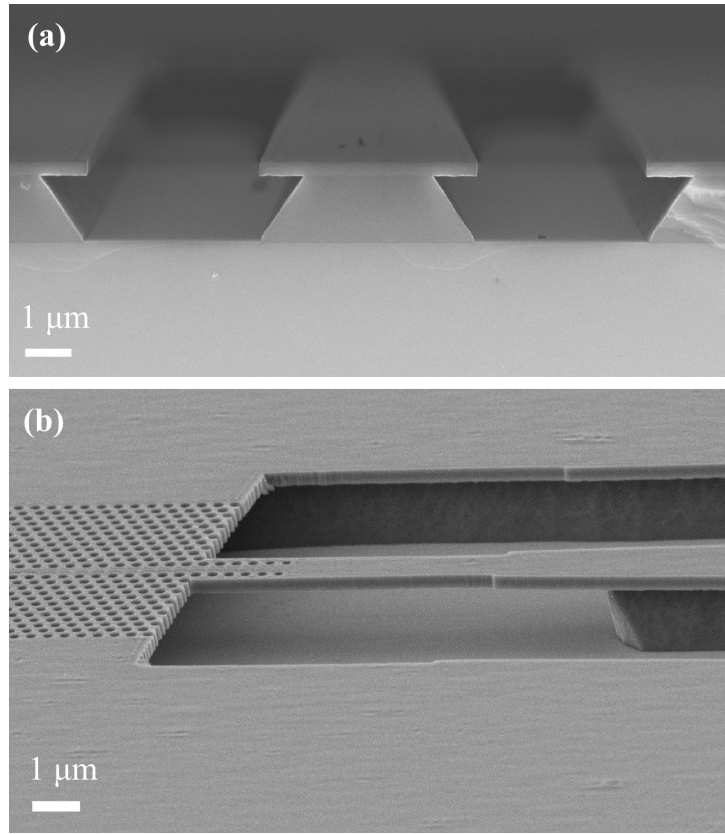


Figure 5.2: Scanning electron microscope (SEM) image of the fabricated devices at (a) entrance of a RWG with $4\ \mu\text{m}$ width and (b) interface of the suspended and ridge structures.

To measure the coupling efficiencies in our system we started by measuring the transmission through a simple RWG with $4\ \mu\text{m}$ width and 1.6 mm length at

room temperature. A tunable continuous wave laser is sent through an end-fire transmission measurement set-up which has two 50× objectives (NA=0.4) for side collection and excitation. The plot of the transmission as a function of the wavelength for the RWG is shown in figure 5.3a where the Fabry-Perot (FP) fringes due to the reflections at the two cleaved facets are evident. The period of these fringes corresponds very well the length of the RWG ($\Delta\lambda = \frac{\lambda^2}{2n_g L}$, where L is the distance between two cleaved facets, n_g is the effective group index of the RWG mode, assumed to be equal to the effective refractive index of the RWG mode ($n_g \simeq n_{eff}$) and λ is the wavelength of the incident light). By fitting the transmission function for the RWG which is given by:

$$T = \eta_C^2 \times \frac{e^{-\alpha L}}{1 + R^2 e^{-2\alpha L} - 2R e^{-\alpha L} \cos(2kL)}, \quad (5.1)$$

where $k = \frac{2n\pi}{\lambda}$ (λ is the wavelength of light in vacuum), α is the loss per unit length, L is the length of the RWG, n is the refractive index of the material, η_C is the coupling efficiency between the fiber and the RWG and R is the reflectivity at the facet calculated by numerical simulations to be around 0.276, we extract [155] the value of the loss per unit length $\alpha \approx 4 - 5 \text{ cm}^{-1}$. This is a rather small loss considering the tight optical confinement in our RWG design. From the fit it is also possible to extract [155] the coupling efficiency between the fiber and the RWG, which for this measurement is $\eta_C \simeq 4\%$.

In the following we use the spectrally-averaged fiber-to-fiber transmission \overline{T}_1 (indicated by horizontal solid red line in figure 5.3a) to give an approximate value of the coupling efficiency \overline{C}_{RWG} : $\overline{T}_1 \simeq \overline{C}_{RWG}^2$, where \overline{C}_{RWG} represents the coupling from the fiber to the center of the RWG including the loss. The value of the transmission (fiber-in, fiber-out power ratio), averaged over the spectral region shown in figure 5.3a, was measured on four nominally identical RWGs, giving a value of $\overline{T}_1 = 0.138 \pm 0.005\%$ and $\overline{C}_{RWG} = 3.72 \pm 0.07\%$ which agrees well with the value obtained from the fitting $\eta_C e^{-\alpha \frac{L}{2}} \simeq 3\%$.

The transmission through a symmetric RWG-PhCWG-RWG system was then measured. The PhCWG here is a triangular PhC with $L = 20 \mu\text{m}$ length (filling factor $FF = 31\%$, lattice constant $a = 320 \text{ nm}$) and the two SNB-PhCWG transitions are tapered as described previously. The spectral transmission of the RWG-PhCWG-RWG system shown in the inset of figure 5.3b over a large range, shows a clear signature of the dispersion edge of the even mode of the PhCWG around $1.32 \mu\text{m}$. A high-resolution wavelength scan is shown in

the main panel of the figure 5.3b around $1.29 \mu\text{m}$, in the high transmission spectral region of the PhCWG. Similar FP fringes were observed in four nominally identical waveguides. The system considered here can be described as a three-layer Fabry-Perot etalon with the corresponding multiple Fourier components which make a reliable fitting of the experimental data difficult, motivating our use of the spectrally-integrated transmission. The average transmission in this spectral range was measured to be $\bar{T}_2 = 0.067 \pm 0.004\%$ on the four waveguides. Denoting the coupling efficiency at the interface between RWG and PhCWG as \bar{C}_{PWG} , we have: $\bar{T}_2 \simeq \bar{C}_{PWG}^2 \times \bar{C}_{RWG}^2$. From the values of \bar{T}_1 and \bar{T}_2 we find $\bar{C}_{PWG} = 0.696 \pm 0.008$ meaning that $\sim 70\%$ of power from the PhCWG is coupled to the RWG. This high value shows the effectiveness of our tapering method. Also we conclude that a fraction $\bar{C}_{PWG} \times \bar{C}_{RWG} = 2.60 \pm 0.08\%$ of the power in the center of the PhCWG is coupled to the single mode fiber.

The final series of measurements are performed on a sample which is composed of a L3 cavity [130] coupled in-line to a PhCWG with two holes (the radius of the second hole is reduced by 10% with respect to the first one) as connecting barriers. The PhCC-PhCWG system is subsequently coupled to the RWG with $400 \mu\text{m}$ length and $4 \mu\text{m}$ entrance width (lattice constant of PhC $a = 330 \text{ nm}$). The sample is cooled down to 5 K in a different end-fire set-up with lensed-fibers (NA=0.33) mounted on piezo-electric positioners for side collection and excitation and an objective (NA=0.5) for top pumping. First a pulsed laser emitting at $\lambda = 757 \text{ nm}$ (repetition rate=80 MHz, pulse width=70 ps) is applied with $0.5 \mu\text{W}$ average power to the cavity from the top and the resulting photoluminescence (PL) coupled to the single-mode fiber via the RWG is collected from the side, dispersed by a $f = 1 \text{ m}$ spectrometer and detected by an InGaAs array detector. A peak at $\lambda = 1309.7 \text{ nm}$ (figure 5.4- black spectrum) is observed which corresponds to the cavity mode ($Q \simeq 1000$) and is pumped by the QD multiexcitonic background [156, 157]. This peak is modulated by FP fringes due to reflections at the cleaved facet and at the interface between RWG and SNB ($L = 400 \mu\text{m}$).

By applying a pulsed quasi-resonant laser ($\lambda = 1064 \text{ nm}$, repetition rate=62 MHz, pulse width=6 ps) the cavity mode was not observed anymore. Reducing the power to 30 nW resulted in the observation of single dot lines (colored spectra in figure 5.4). The temperature of the sample was increased from 5 K to 38 K and the spectral evolution of the single QD indicated by the arrow was recorded. The QD red-shifted by around 1.6 nm in this temperature range. The PL of the QD in and out of resonance with cavity mode (at 25 and 38

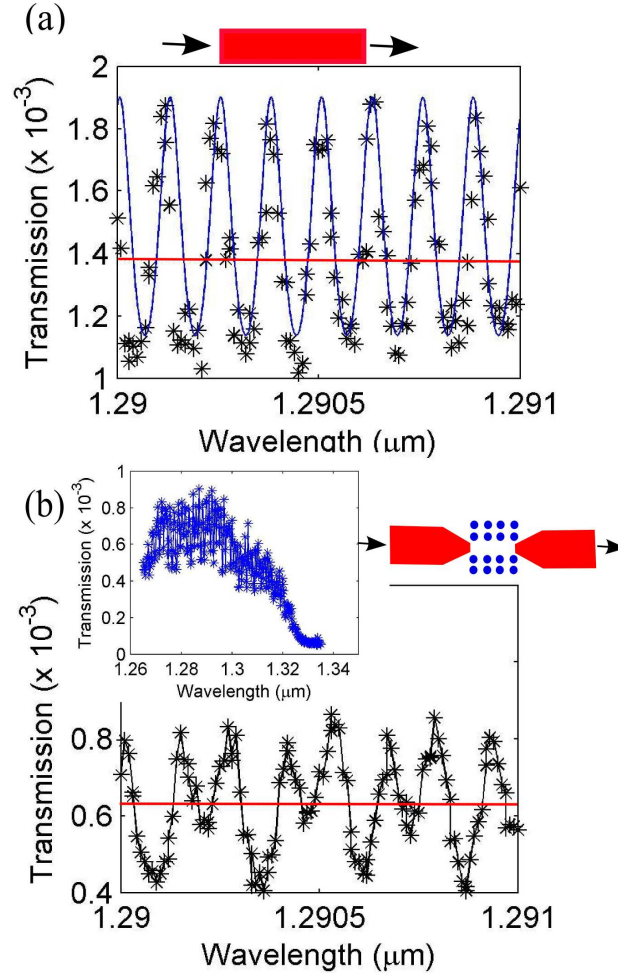


Figure 5.3: Plot of the transmission versus wavelength for a (a) RWG. (the blue and the red horizontal lines are the fit to the experimental data and the average transmission for the measured RWG, respectively). The inset illustrates a sketch of the system measured and (b) RWG-PhCWG-RWG system. The left inset shows the RWG-PhCWG-RWG transmission over a broader spectral range and the right inset illustrates a sketch of the system measured. The red horizontal line indicates the average transmission for the measured RWG-PhCWG-RWG system.

K) was filtered by a tunable filter and sent to a superconducting single photon detector (SSPD) [28], whose output was sent to a correlation card with 4 ps timing resolution. The obtained time-resolved PL spectra showed a change of the lifetime of the QD from $\tau_{on} = 0.67 \pm 0.02$ ns where it was in resonance

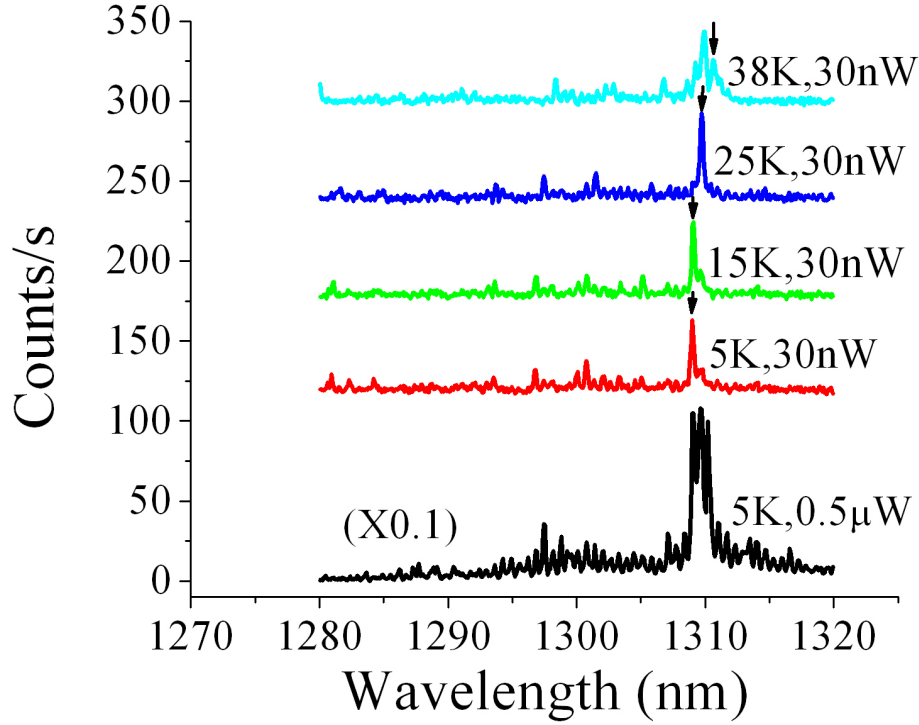


Figure 5.4: PL spectra of a QD in an L3 cavity coupled in-line to a PhCWG and then to a RWG, recorded at different temperatures. The curves are offset for clarity.

with the cavity mode (25 K) to $\tau = 1.47 \pm 0.03$ ns for the situation where it was detuned 1.0 nm from the center of the cavity mode (38 K) (figure 5.5). This change of the spontaneous emission rate is due to the change of the optical density of states and is here limited by the impossibility to tune this QD more than 1.0 nm away from the cavity wavelength. On QDs in the RWG but outside of the PhC region we measured a lifetime $\tau_{bulk} = 1.11 \pm 0.06$ ns (figure 5.5) while for the QDs in the PhC but out of resonance in similar PhC structures we previously measured decay times of $\tau_{off} = 3 - 6$ ns [23]. Based on this, we estimate a Purcell enhancement factor of $F_p = \tau_{bulk} \times (\frac{1}{\tau_{on}} - \frac{1}{\tau_{off}}) \simeq 1.5$ and a coupling efficiency of $\beta = 1 - \frac{\tau_{on}}{\tau_{off}} \simeq 84\%$ of the QDs into the cavity mode.

Ultimately the non-classical (single-photon) nature of the emission from the single QDs into the RWG was investigated. The emission of the aforementioned

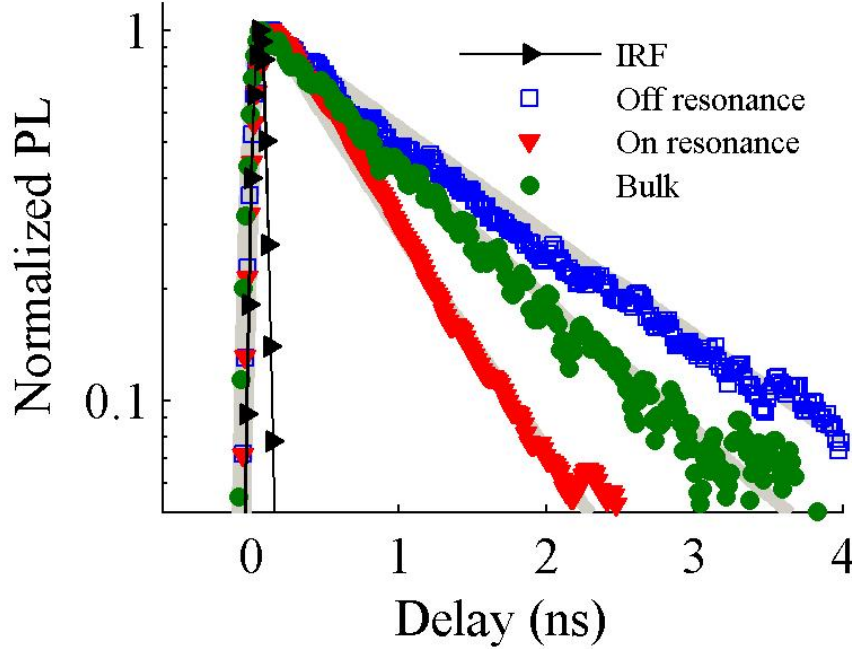


Figure 5.5: Time-resolved PL of the dot indicated by the arrow at 25 K (on-resonance, red triangles) and 38 K (off resonance, blue rectangles) collected from the side. The PL decay of a dot in the bulk (green circles, measured from the side) is shown for comparison. The decay curves have been normalized and the fits (grey lines) are obtained by convolving a mono-exponential decay with the measured instrument response function (IRF) (black triangles).

dot at 25 K, under pumping with the pulsed quasi-resonant laser with the same power as in figure 5.4, is coupled from the side by RWG to the single mode fiber and filtered by the tunable filter and consequently sent to a fiber-based Hanbury Brown-Twiss interferometer based on two SSPDs [158]. A clear dip can be observed at zero delay $\tau = 0$ ns in the corresponding coincidence rate (figure 5.6b) and from the ratio of the coincidence counts at zero delay (integrated over a 6 ns time window) to the average of the counts at the multiples of the repetition period, we estimate a $g^{(2)}(0) \simeq 0.42$. The discrepancy between the experimental value and the perfect single-photon case can be attributed to the residual background emission not completely filtered due to the limited bandwidth (0.8 nm) of our tunable filter (see figure 5.6a).

To estimate the funneling rate of single photons into the RWG (R_{RWG}),

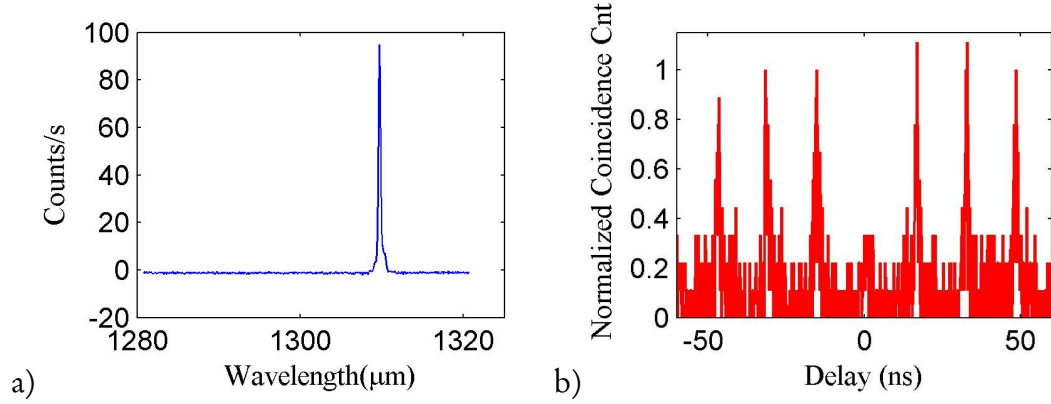


Figure 5.6: (a) MicroPL emission of the QD indicated by arrow in figure 4 obtained at $T = 25$ K, where a tunable filter has been used to detect the emission in QD wavelength, (b) Normalized coincidence counts of the aforementioned QD at 25 K coupled from the side to a Hanbury Brown-Twiss set-up.

we measured the combined detection rate from both SSPDs during the anti-bunching measurement to be around 10 kHz. Taking into account the coupling efficiency from the center of the RWG to the single-mode fiber in the set-up with lensed-fibers, which was measured to be $C'_{RWG} = 7\%$, the transmission of our tunable filter which is equal to 40% and the quantum efficiency of the SSPD $QE = 10\%$, we determine $R_{RWG} = 3.5$ MHz. When compared to the 62 MHz repetition rate of the laser, this indicates a probability of around 6% to produce a single photon in the RWG for each laser pulse. This value is partly limited by the coupling efficiency between PhCC and PhCWG, estimated as $\frac{1}{2} \times Q_{\text{loaded}} \times (Q_{\text{loaded}}^{-1} - Q_{\text{unloaded}}^{-1}) \approx 0.2$, where Q_{loaded} and Q_{unloaded} are the quality factors of the PhCC with and without the PhCWG respectively, as measured on a similar PhCC. An additional limitation is given by the competing emission channels from charged and multi-exciton states in the QD, which prevent reaching the saturated emission rate. The PhC coupling efficiency can be improved by optimized design and fabrication, while the QD charge state may be controlled by the application of an electric field [156], which would also be beneficial for controlling the QD-PhCC spectral coupling [23].

5.2 Progress toward the demonstration of dipole-induced transparency

In order to demonstrate the phenomenon of dipole-induced reflection (DIR) a RWG-PhCWG-PhCC-PhCWG-RWG system with the design mentioned in the previous section has been realized. One of the main technological difficulties for observation of this effect in the aforementioned system is the presence of the FP fringes caused by the reflections at the two end cleaved facets. This problem has been solved by deposition of SiN (with the conditions mentioned in chapter 2) on top of the sample, while the PhC part of the sample is covered by putting a very narrow (1mm) cleaved piece of InP on top of it. With this method the reflection of the cleaved end facets has been reduced. We studied the transmission through many RWG-PhCWG-PhCC-PhCWG-RWG systems (with embedded low density QDs) with Q-factors between 1000-2000. A typical spectrum of the coupled QDs to the cavity mode in these devices (measured at 15 K) can be observed in the figure 5.7a, where a QD coupled to cavity can be distinguished. Figure 5.7b shows the transmission through the same device (at 25 K where the QD and cavity mode has been brought to resonance), where the cavity peak can be clearly observed but no evidence of the DIR was found, which would appear as a dip in the cavity transmission peak (see chapter 3 for more detailed discussion).

As discussed in chapter 3, the phenomena of dipole-induced reflection can be observed in a regime with high Purcell factor and long dephasing times of the QD. As it was also mentioned in this chapter the Q-factors of the PhCCs used for realization of the RWG-PhCWG-PhCC-PhCWG-RWG is not very high ($\approx 1000-2000$). Although the theoretical F_P for this Q value is high for L3 cavities, experimentally observed values are around $F_P \approx 2$ (see section 5.1). This can be due to very limited range of our ability to tune the wavelength of the QDs and inability to grow QDs in a site controlled way to ensure spatial overlap with the PhCCs.

The linewidths of our QDs have been measured by high-resolution photoluminescence spectroscopy and the statistics is presented in figure 5.8. It can be observed that around 4% of the QDs have the linewidth which is resolution limited ($< 30 \mu\text{eV}$ corresponding to a coherence time longer than 45 ps). This is due to the problem of spectral wandering in our QDs. As it has been discussed in chapter 3, with such a coherence time Purcell factors higher than 7 are needed for observing a visible signal (with at least 30% signal visibility, as

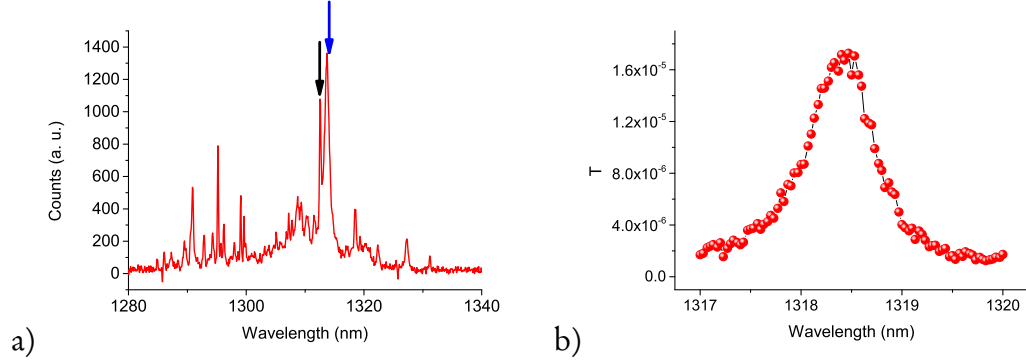


Figure 5.7: (a) MicroPL spectrum of a typical cavity in 15 K (obtained by excitation and collection from the top with a 780 nm exciting laser with $1 \mu\text{W}$ excitation power and 30 seconds acquisition time) where a QD (black arrow) is coupled to the cavity (blue arrow) mode, (b) Transmission of light as a function of wavelength through RWG-PhCWG-PhCC-PhCWG-RWG system measured in 25 K where QD and cavity have been brought to resonance. The FP oscillations have been eliminated by the deposition of SiN as anti-reflection coating layer on two cleaved facets of RWG.

defined in chapter 3). This renders the possibility of the observation of DIR phenomenon in our samples negligible. In order to increase the possibility of the observation of the DIR, better design and fabrication for increasing Q and improved growth conditions for reduction of linewidth in our QDs are needed. DIR has been recently reported in literature [75, 106] in different experimental configurations in strong coupling regime with spectrally narrower QDs.

5.3 Conclusion

In this chapter a design has been proposed for the efficient coupling between a PhC structure and a RWG. The devices fabricated with this design have shown a high value of around 70% for the coupling efficiency between PhCWG and RWG. The emission of single QDs coupled to the RWG has been collected from the side and its rate enhancement with tuning in and out of resonance has been observed. The single photon nature of the detected emission has also been proven. These results represent a step towards the realization of a fully functional quantum photonic integrated circuit, including single photon detectors [29]. Also the technological progress toward fabrication of a system where

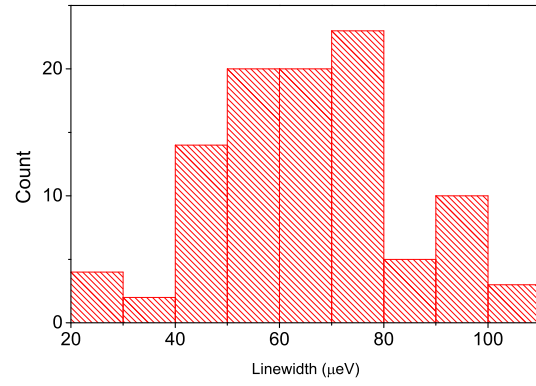


Figure 5.8: Histogram of the distribution of the measured linewidth of the QDs in the best sample available for DIR measurement.

the DIR effect can be observed has been presented and the feasibility of the demonstration of this phenomenon with our present fabrication and growth technology has been investigated.

Resonance Fluorescence of the Single Quantum Dots inside Semiconductor Ridge Waveguides

6.1 Introduction

The phenomenon of resonance fluorescence is a central topic in modern quantum optics. This phenomenon was first theoretically studied by Mollow [159] and was later observed in atomic systems [160, 161]. It describes a situation where a single two-level system is driven by a resonant monochromatic beam and the two-level system emits at the same wavelength as the driving field.

When the Rabi frequency corresponding to the resonant driving field is much bigger than the atomic linewidth, two peaks appear in the two sides of the resonance frequency, where the central peak has twice the intensity of the two side peaks. These three peaks form the so-called Mollow triplet which can be best described by the "dressed" picture. The splitting between these side-bands is proportional to the applied resonant electric field amplitude and therefore to the square root of the laser intensity. This regime has been realized in different platform including solid-state system [162], atomic systems [161], and superconducting qubits [163].

In the very weak Rabi frequency regime, the scattered light imitates the properties of the excitation laser and shows high coherence, known as the Heitler regime [164], which has been experimentally demonstrated in trapped ion systems, and solid-state emitters [165, 166, 167].

Since the properties of the single-photons emitted from an atomic system depend on the method of its excitation, resonance fluorescence has attracted

tremendous attention for the realization of quantum information schemes in the recent years. It allows for direct and coherent access and excitation of two-level systems and generation of brighter and back-ground free single-photon emission.

6.2 Polarization properties of the emission of single InAs/GaAs quantum dots

Semiconductor quantum dots (QDs) show atomic-like sharp transitions and can be integrated inside semiconductor microcavities and waveguides, which can be used to realize many quantum optical phenomena in a scalable solid-state system including Rabi oscillations [168, 169, 170, 171, 55, 172] and anti-bunching [173]. They are also very good candidates for the generation of indistinguishable single photons for applications in quantum cryptography and computation [174, 175, 176, 177]. Incoherent excitation of the QDs lacks the ability to access and manipulate the excitonic transition and creates additional excitation of the continua of the modes of the environment, enhancing the spectral diffusion [178]. In order to fully use the capabilities of QDs for quantum information applications, simultaneous resonant manipulation and detection of their emission, similar to what has been achieved in atomic systems, is required. Although different schemes such as four-wave mixing [179] and differential transmission and reflection [169, 180] for the coherent manipulation of the two-level systems have been demonstrated, these schemes cannot simultaneously manipulate the two-level system coherently and collect the generated single-photons, indicating the importance of the resonance fluorescence for applications in quantum information and computation. The main difficulty here arises from the strong scattering of the resonant laser beam off the defects in the solid-state system which dominates the weak single-photon signal. Recently approaches based on coupling of laser scattering to a planar distributed Bragg reflector (DBR) [162, 181] and cross polarization techniques [182, 183, 184] have been used to suppress the laser scattering in planar structures. However, in micro- and nanophotonic structures such as waveguides and cavities the scattering is a more critical issue and so far resonant fluorescence of QDs in waveguides has not been demonstrated.

In this chapter of this thesis a novel technique has been used to detect the resonance fluorescence of the QDs in a ridge waveguide and the properties of

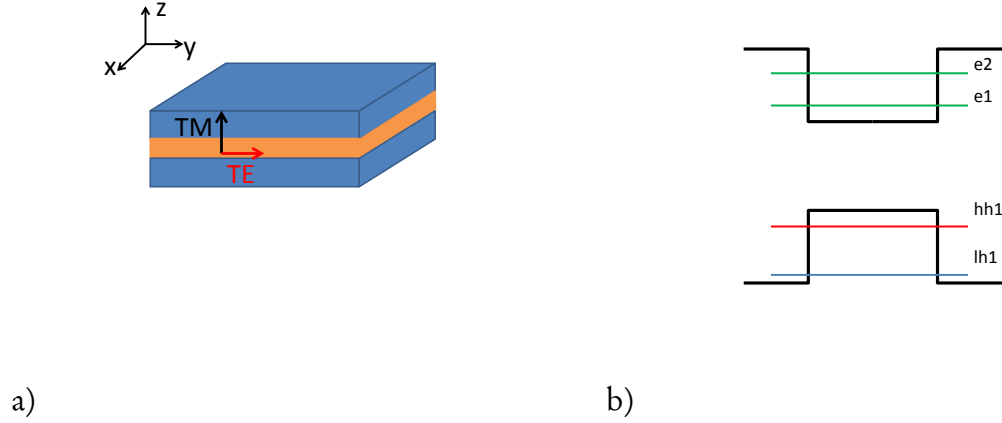


Figure 6.1: (a) Sketch of a quantum well heterostructure, where the growth direction has been assumed to be z direction. (b) Typical energy diagram of the QD heterostructures, where different electron and hole energy levels have been depicted.

this emission have been investigated.

6.2.1 Polarization of the emission of single InAs/GaAs quantum dots

The wavefunction of the electrons in a heterostructure is described by the envelope function formalism. The detailed derivation of this formalism is beyond the scope of this thesis and can be found somewhere else [185]. In order to have an understanding of the electronic wavefunction in the QDs used in this work, first we consider the wavefunction of an electron in a quantum well (QW). In this case the electronic wave function can be described by the product of a periodic function and an envelope function, where the envelope function satisfies the Schrödinger equation with the heterojunction's potential. If we consider the growth direction to be the z direction (figure 6.1a), the presence of the heterojunction will remove the degeneracy between the light and heavy holes and pushes the light holes away toward lower energies (figure 6.1b) (Light and heavy holes are the eigen-states of the \hat{J}^2 ($\hat{J} = \hat{L} + \hat{S}$) operator with quantum-numbers (J, J_z) equal to $(\frac{3}{2}, \pm\frac{1}{2})$ and $(\frac{3}{2}, \pm\frac{3}{2})$, where \hat{L} and \hat{S} indicate the angular momentum and spin of the electron).

The QDs used in this work (InAs/GaAs QDs) are conventional Stranski-

Krastanov QDs, which are elongated in the plane, hence have a similar behavior as QWs. The heterostructure confinement and the presence of the compressive strain which creates an anisotropic deformation of the lattice pushes the light holes toward lower energies.

The lowest-energy transition from the conduction to the valance level therefore involves heavy-hole states. Due to the spatial distribution of the wave function of the heavy hole, for the transition probability from an electronic state to the heavy hole state we have [186]

$$\langle \phi_{hh}^* | z | \phi_e \rangle = 0,$$

where z is the growth direction and ϕ_{hh} and ϕ_e are the wave functions of the heavy hole and the electron, respectively.

The emission from the InAs/GaAs QDs used in the work is therefore strongly TE polarized (electric field in the same plane as the growth plane).

6.2.2 Fine-structure splitting in single quantum dots

In order to present the solution used in this work to suppress the scattering of the resonant laser, we first look into the fine-structure splitting of QDs.

The fundamental excitation in a QD brings an electron from the valence band to the conduction band, leaving behind a hole in the valence band. The holes can be introduced as quasiparticles with spin and charge opposite to that of electrons. This picture depicts the excited electron as system of two particles consisting of an electron and a hole. But this picture does not capture the whole physics involved. In order to complete this picture we have to introduce the interaction between holes and electrons. This interaction describes the formation of a new quasiparticle called exciton.

So far in describing excitonic structure we have not considered their fermionic nature. Electrons and holes are fermions meaning that they have half-integer spins and they obey Pauli's principle. This characteristic of fermions creates an additional interaction between electrons and holes called exchange interaction.

When an exchange of the coordinates occur between two identical particles, the situation remains identical and the system has exchange degeneracy. In the case of Fermions we have anti-symmetric solutions for the system's wave-function and therefore the Coulomb interaction Hamiltonian between electrons and holes will have the terms called exchange terms in the following form [187]:

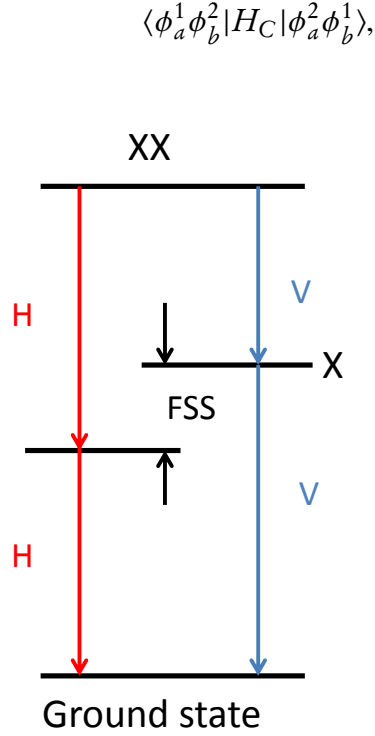


Figure 6.2: Schematic of the fine structure splitting of a QD. The bi-exciton can have two different decay paths.

where H_C indicates the Coulomb interaction between the electron and the hole. Due to the low degeneracy in QDs resulting from elongation of the QD along one axis and the strain, this interaction term lifts the degeneracy of the excitonic ground state, resulting in a superposition of two eigenstates of the symmetric QD (with projection of the total angular momentum along the growth direction of $J_z = +1$ and $J_z = -1$) into symmetric and asymmetric eigenstates which couple to V- and H-polarized photons, where V and H indicate the $[1\bar{1}0]$ and $[110]$ axes of the crystal [27]. The resulting energy splitting between the energy levels of H- and V-polarized photons is called fine-structure splitting (FSS) as pictured in figure 6.2. Also the bi-excitonic state can have two different decay paths via H- and V-polarized states which are separated by the FSS. Recently a tremendous amount of attention in literature has been paid to FSS since its elimination enables the generation of photonic entangled states [176, 177].

6.3 Observation of the resonance fluorescence of single InAs/GaAs quantum dots in a ridge waveguide

As it was stated in the introduction, the main obstacle for observing resonance fluorescence in a solid-state system is the strong scattering of the resonant laser which dominates the weak single-photon signal. In this part, we used the polarization of the emission of single QDs to propose a way to suppress the scattering of the resonant laser. The experimental setup is shown in figure 6.3. Due to the

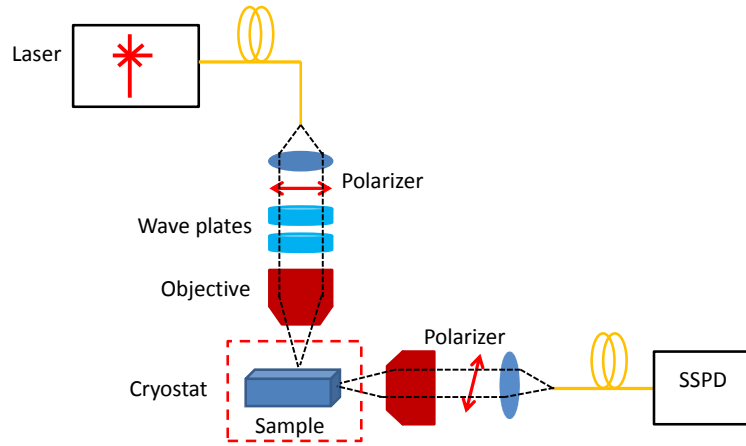


Figure 6.3: Sketch of the experimental setup used, where the QDs are resonantly excited from the top and their resonance fluorescence is collected from the side. Details have been explained in the text.

design of the setup, by sending the resonant laser from the top-excitation arm we can only excite the polarizations in the plane (perpendicular to the growth direction). Due to the fabrication imperfections in our RWGs the collected signal by the side-collection arm will consist of the excited transition of the QD

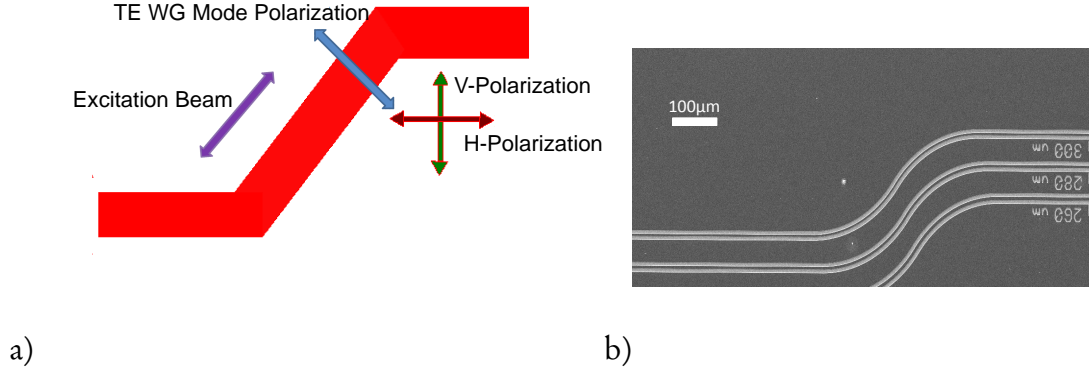


Figure 6.4: (a) Sketch of the method used to suppress the laser scattering in our system using polarization properties of QDs. (b) SEM picture of the fabricated bent RWGs used in the experiment.

and the scattered laser. The polarizer in the side collection arm can only rotate in the plane parallel to the cleaved facet of the RWG which makes the use of the standard cross-polarization schemes in this configuration impossible, since the scattered laser and the signal will be filtered or passed together.

In order to solve the problem we designed bent RWGs (the detail of the fabrication process has been discussed in chapter 2). The mechanism of this solution can be best clarified if we consider the situation depicted in figure 6.4a where the resonant laser is sent from the top with a polarization orthogonal to the polarization of the TE mode of the RWG, so that scattering into the TE mode is strongly suppressed. In the bent region this laser can excite both QD transitions with H- and V-polarizations (split by FFS) which also couple to the TE guided mode. Any residual TM-polarized scattered light is suppressed by a polarizer at the output.

The sample used in these experiments is composed of bent RWGs fabricated from a wafer composed of a 320 nm GaAs layer over a 1.5 μm AlGaAs layer, with InAs QDs embedded in the middle of GaAs layer. The width of the RWG is 4 μm and the GaAs layer is etched around 220 nm in two sides of the RWG to make the trenches (A SEM picture of the devices is shown in figure 6.4b). In order to demonstrate the observation of resonance fluorescence in a RWG, the sample has been cooled down to 15 K in our experimental setup, where

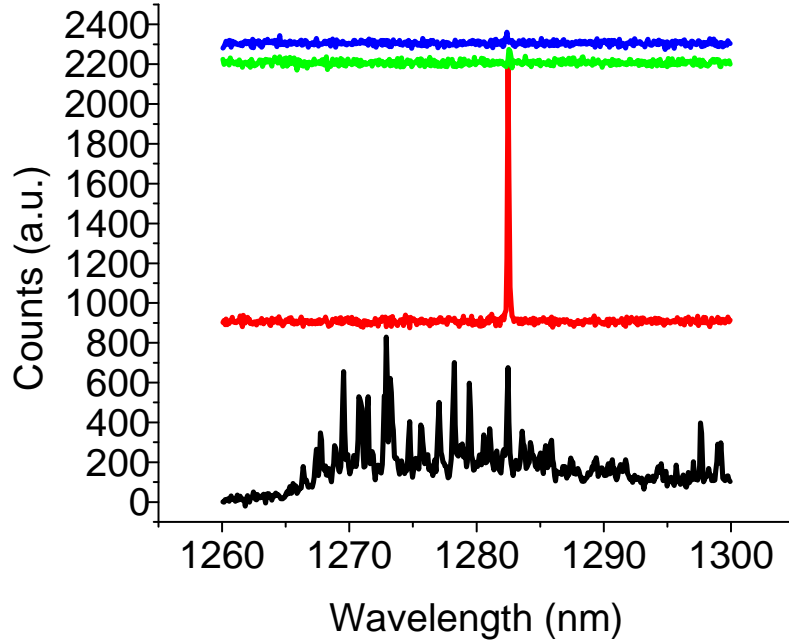


Figure 6.5: Microphotoluminescence of the QDs excited from the top and collected from the side. Black: when excited non-resonantly (by 780 nm laser with $0.5 \mu\text{W}$ excitation power and 30 seconds acquisition time) from the top and collected from the side. Red: excited resonantly with $100 \mu\text{W}$ excitation power and 30 seconds acquisition time. Green: when resonant pump (same power and acquisition time as the red plot) is detuned $+0.15 \text{ nm}$ from the QD wavelength. Blue: when resonant pump (same power and acquisition time as the red plot) is detuned -0.15 nm from the QD wavelength. Offset is for clarity.

we have access to the optical emission from top and side. In the first series of the measurements, the non-resonant PL of the QDs by exciting them from the top (with a 780 nm laser, 500 nW power and 30 seconds acquisition time) and collecting the resulting PL from the side has been obtained as depicted in figure 6.5. By applying a tunable CW resonant laser in resonance with the QD (with $100 \mu\text{W}$ power and 30 seconds acquisition time) indicated in the figure and collecting the resonant-PL from the side we observe a strong increase in the emission of the QD. When the laser is detuned from the QD wavelength by a small amount ($\sim 0.15 \text{ nm}$) we see an almost complete suppression of the

resonant-PL. This is a strong indication of the resonance fluorescence in our QD.

In the next series of measurements we selected another QD and used our CW resonant laser (excitation from the top and collection from the side) to measure the linewidth of the QD by sweeping the laser wavelength through the QD wavelength with a resolution of around $3 \mu\text{eV}$. The obtained emission has been sent to a SSPD for detection. During this measurement we applied a very weak (60 nW) non-resonant (780 nm laser) in order to create the optical gating effect for the efficient extraction of resonance fluorescence [188]. The plot of the resonance fluorescence intensity versus the detuning has been shown in figure 6.6. Here two lines with widths (FWHM) of 41 and $32 \mu\text{eV}$ can be observed that indicate the two different polarizations of the QD along $[\bar{1}\bar{1}0]$ and $[110]$ axes of the crystal. These two lines are separated by $64 \mu\text{eV}$ which is the amount of FSS in this QD.

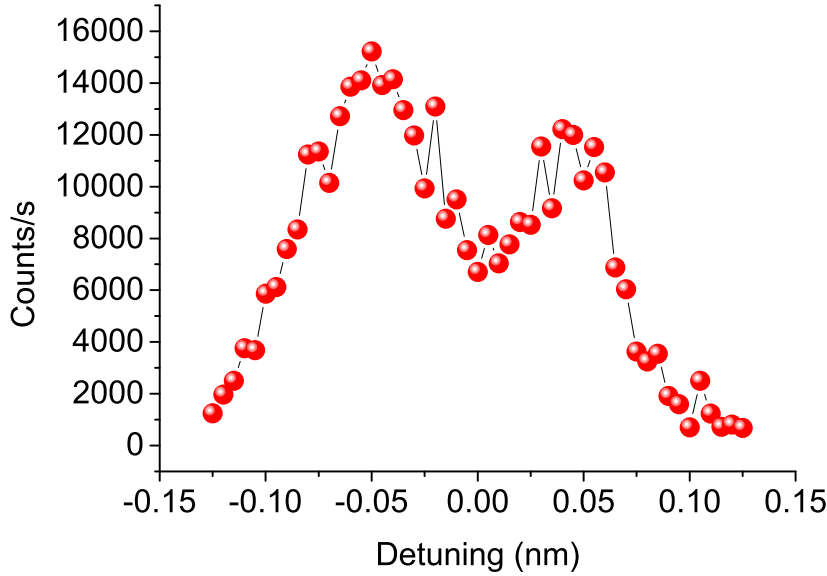


Figure 6.6: Integrated resonance fluorescence intensity of the QD excited from the top (with $200 \mu\text{W}$ power) and collected from the side as a function of the detuning of the top resonant exciting laser where the FSS doublet can be observed.

The interaction of the QD and the CW resonant laser can be described by using optical Bloch equations [52] for a two-level system. By treating the field

semi-classically and using the rotating wave approximation we have:

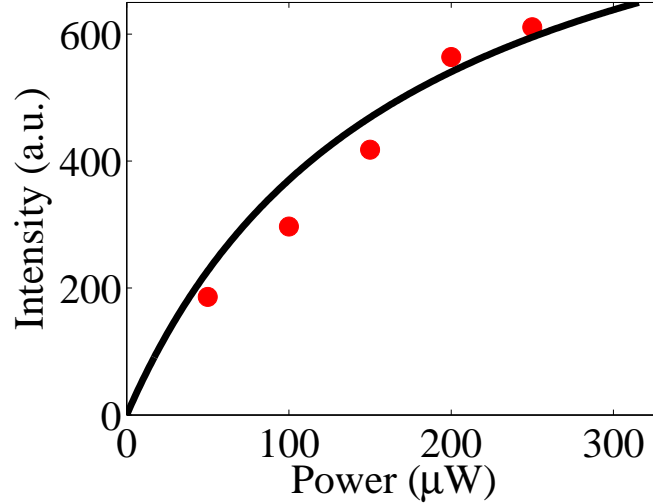


Figure 6.7: Resonance peak intensity versus the applied power of the resonant laser. The solid line is the fit obtained by using the equation 6.6.

$$\dot{b} = -i\frac{\Omega}{2}(c - c^*) - \frac{b}{T_1} \quad (6.1)$$

$$\dot{c} = -i\frac{\Omega}{2}(b - a) + ic\Delta\omega - \frac{c}{T_2}. \quad (6.2)$$

Here $a = Tr(\rho A)$, $b = Tr(\rho B)$ are the populations of the two states, where $A = |1\rangle\langle 1|$ and $B = |2\rangle\langle 2|$, and $c = Tr(\rho C)$ is the coherence of the two-level system, where $C = |1\rangle\langle 2|$ ($|1\rangle$ and $|2\rangle$ indicated the ground and the excited state of the QD) and $\Delta\omega$ is the detuning between the laser frequency and the two-level system frequency. $\Omega = \mu E$ indicates the Rabi frequency where E is the driving amplitude of the resonant CW laser and μ is the dipole moment of the two-level system. T_1 and T_2 denote the lifetime of the excited state population and the decoherence time of the QD which are related via the formula:

$$\frac{1}{T_2} = \frac{1}{2T_1} + \frac{1}{T_\gamma}, \quad (6.3)$$

where T_γ is the pure dephasing time of the QD.

Solving equations (6.1) and (6.2) for the steady state yields:

$$b(\Delta\omega) = \frac{1}{2} \frac{\Omega^2 T_1 / T_2}{\Omega^2 T_1 / T_2 + T_2^{-2} + \Delta\omega^2} \quad (6.4)$$

$$c(\Delta\omega) = -i \frac{\Omega}{2} \frac{1/T_2 + i\Delta\omega}{\Omega^2 T_1 / T_2 + T_2^{-2} + \Delta\omega^2}. \quad (6.5)$$

These formulas can be simplified for the resonance case as follows [52]:

$$I \propto \frac{\Omega^2 T_1 T_2}{\Omega^2 T_1 T_2 + 1} \propto \frac{P}{P_{sat} + P} \quad (6.6)$$

$$\delta_L = \frac{2\hbar}{T_2} \sqrt{\frac{P}{P_{sat}} + 1}, \quad (6.7)$$

where δ_L is the linewidth of the two-level system under resonant excitation and I is the intensity of the RF signal.

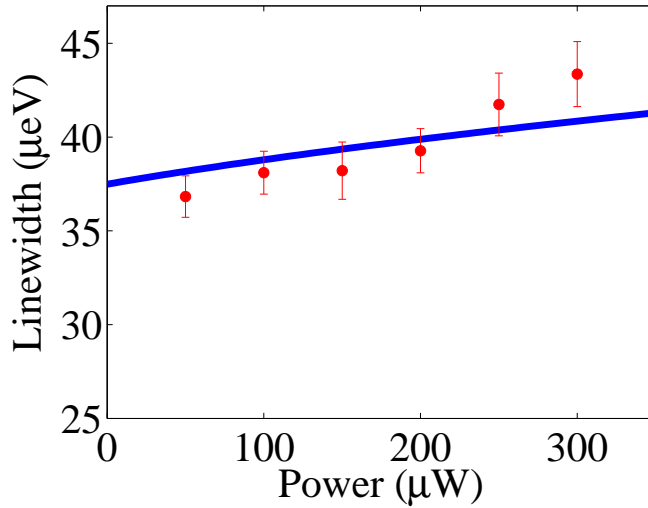


Figure 6.8: Linewidth of the QD versus the applied power of the resonant laser. The solid line is the fit obtained by using the equation 6.8.

From these formulas it can be deduced that the population of the QD saturates at high intensities of the laser and the linewidth of the QD has a zero-intensity limit of $\delta_0 = \frac{2\hbar}{T_2}$ and broadens with increasing power, a phenomenon known as power broadening [189].

In the last series of our measurements we recorded the peak intensity of the resonance fluorescence and the linewidth of the one of the polarizations of the QD versus the applied power of the resonance laser. The the peak intensity of the resonance emission of the QD versus the applied power (figure 6.7) can be nicely fit with equation 6.6 with the parameter $P_{sat} = 160 \mu\text{W}$. In order to incorporate the effect of spectral diffusion in our system we note that the linewidth of the QD is the result of the convolution of the Gaussian profile resulting from the spectral diffusion and the Lorentzian profile originated from the power broadening mechanism [190, 191]. This results in the so called Voigt line shape where the FWHM of the QD is given by:

$$\delta \approx A\delta_L + \sqrt{(1-A)^2\delta_L^2 + \delta_d^2}, \quad (6.8)$$

where δ_d indicates the linewidth of the QD originated by spectral diffusion and $A = 0.5346$ is a parameter which is empirically determined [190]. Fitting the measured linewidth (figure 6.8) with this formula results in $\delta_0 \approx 8 \mu\text{eV}$ and $\delta_d \approx 33 \mu\text{eV}$. The value of the zero-intensity-limit for the coherence time can be attributed to the relatively high temperature (15 K) where the experiment was performed [181]. In order to further prove the highly single-photon nature of the emission we need to perform anti-correlation measurements which would be very demanding in this case due to the low β -factor of the RWGs and the instability of the optical setup for long integration times.

6.4 Conclusion

In this section, a new technique based on the polarization properties of the InAs/GaAs QDs has been proposed to suppress the scattering of the resonant laser and detection of the resonance fluorescence of the QDs in RWGs. The obtained resonance fluorescence data is in good agreement with theoretical formalism describing the interaction of a resonant laser with a two-level system.

Conclusions and Outlook

Semiconductor quantum dots are one of the best candidates for generation of single photons at telecommunication wavelengths for quantum information purposes. The possibility of integrating them in solid state circuits have made them very appealing for practical applications. In this thesis new fabrication methods for efficient extraction of single photon emission of semiconductor quantum dots (QDs) inside a quantum photonic integrated circuit (QPIC) have been implemented and the properties of the emission of QDs at the single photon level in different excitation regimes inside the semiconductor waveguides have been investigated. The main results achieved during the course of this work can be summarised as follows:

- A fabrication method for efficient coupling of a light between a photonic crystal waveguide (PhCWG) and a ridge waveguide (RWG) has been designed and implemented. By using a novel etching method it was possible to perform the fabrication in a single lithographic step. The devices obtained with this method showed 70% transmission between PhCWG and RWG. The single photon nature of the emission of QDs under non-resonant excitation has been demonstrated and single-photon funnelling rates around 3.5 MHz from the PhCWG to RWG have been demonstrated. This represents the first demonstration of efficient funnelling of single photons in a RWG.
- By exploiting the polarization properties of the emission of QDs used in this work, a new method based on k-vector and polarization filtering has been proposed for the filtering of the resonant laser scattering and extraction of the

resonance fluorescence of the QDs inside RWGs. Power-dependent resonance fluorescence of the QDs and the phenomenon of power broadening have been observed.

- A theoretical investigation of the nonlinear phenomena of dipole-induced reflection (DIR) and single-photon stimulated emission based on the Master equation approach has been performed and the feasibility of the observation of these phenomena in our experimental system has been discussed. While devices with suitable transmission for observation of DIR have been fabricated, the progress has been hampered by the typical linewidths of the available QDs, which make the observation of DIR very improbable in our system. On the other hand the demonstration of the resonant driving of the QD by filtering the scattering of the resonant laser makes the observation of single-photon stimulated emission feasible in the near future.

There are many ways in which the results obtained in this thesis can be improved. The coupling of the photonic crystal cavity (PhCC) to PhCWG can be improved by improved electron-beam lithography (EBL) and etching, and better coupled PhCC-PhCWG system design, such as tilted-cavity or side-coupling schemes. The PhCC-PhCWG-RWG system can be used as an on-chip filter and it can also be realized with double membrane structures for achieving a tunable on-chip filter. This together with control over the frequency of the cavity mode and QD will constitute an important component of future QIPCs where experiments like on-chip single-photon interference would be possible. Furthermore the polarization properties of the structures with higher β -factors like PhCs [192, 193] can be exploited to design and realize devices where the resonance fluorescence of the QDs can be extracted more efficiently.

For the observation of the dipole-induced reflection effect, better fabrication of the PhCC can help increasing of Purcell factor and improvements in growth conditions can lead to narrower linewidth of the QDs, which all facilitate the observation of this effect. The DIR can further be used for the realization of the optical switches. With more theoretical efforts the possibility of the realization of optical gates based on single-photon nonlinearity can be explored and the aforementioned effect can play the central role in this realization.

The operation of a fully on-chip integrated quantum device such as a quantum gate requires efficient coupling to on-chip detectors and to optical fibers for long distance communications. This is a prerequisite for a quantum network or systems like quantum internet [12]. The present thesis contributes to

this field by the demonstration of efficient injection and extraction of photons into a waveguide and undertakes first steps towards the integration of nonlinear elements such as QDs in waveguide-coupled PhCCs. The possibility of the extraction of resonance fluorescence emission from QDs embedded into RWGs, demonstrated in this thesis, paves the way for on-demand on-chip generation of the single photons at telecommunication wavelength with significantly enhanced indistinguishability [167] which is a requirement for the demonstration of on-chip entanglement of QD spins and photons [194, 195] as a first step towards more advanced quantum communication and computation functionalities such as quantum state transfer [196].

Bibliography

- [1] G. E. Moore. Cramming more components into integrated circuits. *Electronics*, 38:114, 1965.
- [2] T. L. Koch and K. Uziel. Semiconductor photonic integrated circuits. *IEEE Journal of Quantum Electronics*, 27:641, 1991.
- [3] J. J. G. M. van der Tol, R. Zhang, J. Pello, F. Bordas, G. C. Roelkens, H. P. M. M. Ambrosius, P. J. A. Thijs, F. Karouta, and M. K. Smit. Photonic integration in indium-phosphide membrane on silicon. *IET Optoelectronics*, 5:218, 2011.
- [4] M. K. Smit and C. Van Dam. PHASAR-based WDM-devices: Principles, design and applications. *IEEE Journal of Selected Topics in Quantum Electronics*, 2:236, 1996.
- [5] Y. Miyazaki, H. Tada, T. Aoyagi, T. Nishimura, and Y. Mitsuri. Extremely small-chirp electroabsorption-modulator integrated distributed feedback laser diode with a shallow quantum-well absorption layer. *IEEE Journal of Quantum Electronics*, 38:1075, 2002.
- [6] J. L. O'Brien, A. Furusawa, and J. Vuckovic. Photonic quantum technologies. *Nature Photonics*, 3:687, 2009.
- [7] A. Einstein. Über einen die erzeugung und verwandlung des lichtes betreffenden heuristischen gesichtspunkt. *Annalen der Physik*, 17:172, 1905.

- [8] G. N. Lewis. The conservation of photons. *Nature*, 118:874, 1926.
- [9] J. L. O'Brien. Optical quantum computing. *Science*, 318:1567, 2007.
- [10] M. A. Nielsen and I. L. Chuang. *Quantum computation and quantum information*. Cambridge University Press, 2000.
- [11] T. D. Ladd, F. Jelezko, R. Laflamme, Y. Nakamura, C. Monroe, and J. L. O'Brien. Quantum computers. *Nature*, 464:45, 2010.
- [12] H. J. Kimble. The quantum internet. *Nature*, 453:1023, 2008.
- [13] S. J. Wiesner. Conjugate coding. *SIGAT news*, 15:78, 1983.
- [14] C. H. Bennett and G. Brassard. Quantum cryptography: Public key distribution and coin tossing. In *Proceedings of IEEE International Conference on Computers, Systems and Signal Processing*, volume 175, page 8, 1984.
- [15] G. Brassard, N. Lutkenhaus, T. Mor, and B. C. Sanders. Limitations on practical quantum cryptography. *Physical Review Letters*, 85:1330, 2000.
- [16] H. Takesue, S. W. Nam, Q. Zhang, R. H. Hadfield, T. Honjo, K. Tamaki, and Y. Yamamoto. Quantum key distribution over a 40dB channel loss using superconducting single photon detectors. *Nature Photonics*, 1:343, 2007.
- [17] H. Shibata, K. Shimizu, H. Takesue, and Y. Tokura. Superconducting nanowire single-photon detector with ultralow dark count rate using cold optical filters. *Applied Physics Express*, 6:072801, 2013.
- [18] R. P. Feynman. Simulating physics with computers. *International Journal of Theoretical Physics*, 21:467, 1982.
- [19] A. Aspuru-Guzik and P. Walther. Photonic quantum simulators. *Nature Physics*, 8:285, 2012.
- [20] B. J. Metcalf, N. Thomas-Peter, J. B. Spring, D. Kundys, M. A. Broome, P. C. Humphreys, X. M. Jin, M. Barbieri, W. S. Kolthammer, J. C. Gates, B. J. Smith, N. K. Langford, P. G. Smith, and I. A. Walmsley. Multi-photon quantum interference in a multiport integrated photonic device. *Nature Communications*, 4:1356, 2013.

- [21] A. Politi, M. J. Cryan, J. G. Rarity, S. Yu, and J. L. O'Brien. Silica-on-silicon waveguide quantum circuits. *Science*, 320:646, 2008.
- [22] A. Peruzzo, M. Lobino, J. C. Matthews, N. Matsuda, A. Politi, K. Poulios, X. Q. Zhou, Y. Lahini, N. Ismail, K. Worhoff, Y. Bromberg, Y. Silberberg, M. G. Thompson, and J. L. O'Brien. Quantum walks of correlated photons. *Science*, 329:5998, 2010.
- [23] T. B. Hoang, J. Beetz, M. Lerner, L. Midolo, M. Kamp, S. Höfling, and A. Fiore. Widely tunable, efficient on-chip single photon sources at telecommunication wavelengths. *Optics Express*, 20:21758, 2012.
- [24] D. Englund, A. Faraon, B. Zhang, Y. Yamamoto, and J. Vuckovic. Generation and transfer of single photons on a photonic crystal chip. *Optics Express*, 15:5550, 2007.
- [25] A. Schwagmann, S. Kalliakos, J. D. P. Ellis, I. Farrer, J. P. Griffiths, G. A. C. Jones, D. A. Ritchie, and A. J. Shields. In-plane single-photon emission from a L3 cavity coupled to a photonic crystal waveguide. *Optics Express*, 20:28614, 2012.
- [26] A. Laucht, S. Putz, T. Gunthner, N. Hauke, R. Saive, S. Frederik, M. Bichler, M. C. Amann, A. W. Holleitner, M. Kaniber, and J. J. Finley. A waveguide-coupled on-chip single-photon source. *Physical Review X*, 2:011014, 2012.
- [27] A. J. Shields. Semiconductor quantum light sources. *Nature Photonics*, 1:215, 2007.
- [28] G. N. Golt'sman, O. Okunev, G. Chalkove, A. Lipatov, A. Semenov, K. Smirnov, B. Voronov, A. Dzardanov, C. Williams, and R. Sobolevski. Picosecond superconducting single-photon optical detector. *Applied Physics Letters*, 79:705, 2001.
- [29] J. P. Sprengers, A. Gaggero, D. Sahin, S. Jahanmirinejad, G. Frucci, F. Mattioli, R. Leoni, J. Beetz, M. Lerner, M. Kamp, S. Höfling, S. Sanjines, and A. Fiore. Waveguide superconducting single-photon detectors for integrated quantum photonic circuits. *Applied Physics Letters*, 99:181110, 2011.

- [30] T. Gerrits, N. Thomas-Peter, J. C. Gates, A. E. Lita, B. J. Metcalf, B. Calkins, N. A. Tomlin, A. E. Fox, A. L. Linares, J. B. Sprengers, N. K. Langford, R. P. Mirin, P. G. R. Smith, I. A. Walmsley, and S. W. Nam. On-chip photon-number-resolving telecommunication band detectors for scalable photonic information processing. *Physical Review A*, 84:060301, 2011.
- [31] G. Reitmaier, S. Lichtmanneker, T. Reichert, P. Hasch, K. Muller, M. Bichler, R. Gross, and J. J. Finley. On-chip time resolved detection of quantum dot emission using integrated superconducting single photon detectors. *Scientific Reports*, 3:1901, 2013.
- [32] M. Bayer and A. Forchel. Temperature dependence of the homogeneous linewidth in InGaAs/GaAs self-assembled quantum dots. *Physical Review B*, 65:041308, 2002.
- [33] E. Yablonovitch. Inhibited spontaneous emission in solid-state physics and electronics. *Physical Review Letters*, 58:2059, 1987.
- [34] E. Yablonovitch, T. J. Gmitter, and K. M. Leung. Photonic band structure: The face-centered-cubic case employing nonspherical atoms. *Physical Review Letters*, 67:2295, 1991.
- [35] T. F. Krauss, R. M. De la Rue, and S. Brand. Two-dimensional photonic-bandgap structures operating at near-infrared wavelengths. *Nature*, 383:699, 1996.
- [36] S. H. Fan, S. G. Johnson, J. D. Joannopoulos, C. Manolatou, and H. A. Haus. Waveguide branches in photonic crystals. *Journal of Optical Society of America B*, 18:162, 2001.
- [37] M. Bayindir, B. Temelkuran, and E. Ozbay. Photonic-crystal-based beam splitters. *Applied Physics Letters*, 77:3902, 2000.
- [38] S. H. Fan, P. R. Villeneuve, J. D. Joannopoulos, M. J. Khan, C. Manolatou, and H. A. Haus. Theoretical analysis of channel drop tunneling processes. *Physical Review B*, 59:15882, 1999.
- [39] S. H. Fan, P. R. Villeneuve, J. D. Joannopoulos, and H. A. Haus. Channel drop filters in photonic crystals. *Optics Express*, 3:4, 1998.

- [40] P. R. Villeneuve, S. H. Fan, and J. D. Joannopoulos. Microcavities in photonic crystals: Mode symmetry, tunability, and coupling efficiency. *Physical Review B*, 54:7837, 1996.
- [41] K. Srinivasan, P. E. Barclay, O. Painter, J. Chen, A. Y. Cho, and C. Gmachl. Experimental demonstration of a high quality factor photonic crystal microcavity. *Applied Physics Letters*, 83:1915, 2003.
- [42] M. Pelton, C. Santori, J. Vuckovic, B. Zhang, G. S. Solomon, J. Plant, and Y. Yamamoto. Efficient source of single photons: A single quantum dot in a micropost microcavity. *Physical Review Letters*, 89:233602, 2002.
- [43] P. B. Deotare, M. W. McCutcheon, I. W. Frank, M. Khan, and M. Loncar. High quality factor photonic crystal nanobeam cavities. *Applied Physics Letters*, 94:121106, 2009.
- [44] K. Rivoire, A. Faraon, and J. Vuckovic. Gallium phosphide photonic crystal nanocavities in the visible. *Applied Physics Letters*, 93:063103, 2008.
- [45] K. Aoki, D. Guimard, M. Nishioka, M. Nomura, S. Iwamoto, and Y. Arakawa. Coupling of quantum dot light emission with a three-dimensional photonic crystal nanocavity. *Nature Photonics*, 2:688, 2008.
- [46] J. D. Joannopoulos, S. G. Johnson, J. N. Winn, and R. D. Meade. *Photonic crystals: Molding the flow of light*. Princeton University Press, 2008.
- [47] N. W. Ashcroft and N. D. Mermin. *Solid state physics*. Brooks/Cole, 1976.
- [48] P. Lodahl, S. Mahmoodian, and S. Stobbe. Interfacing single photons and single quantum dots with photonic nanostructures. *Arxiv*, 1312.1079, 2013.
- [49] E. Jaynes and F. Cummings. Comparison of quantum and semiclassical radiation theories with application to the beam maser. *Proceedings of the IEEE*, 51:89, 1963.
- [50] H. P. Breuer and F. Petruccione. *The theory of open quantum systems*. Oxford University Press, 2002.

- [51] S. Haroche and J. Raimond. *Exploring the quantum: Atoms, cavities and photons*. Oxford University Press, 2013.
- [52] C. Cohen-Tannoudji, J. Dupont-Roc, and G. Grynberg. *Atom-photon interactions: basic processes and applications*. John Wiley & Sons, Inc., 1992.
- [53] E. M. Purcell. Spontaneous emission probabilities at radio frequencies. *Physical Review*, 69:681, 1946.
- [54] J. M. Gerard, J. M. Rard, B. Sermage, B. Gayral, B. Legrand, E. Costard, and V. Thierry-Mieg. Enhanced spontaneous emission by quantum boxes in a monolithic optical microcavity. *Physical Review Letters*, 81:1110, 1998.
- [55] J. P. Reithmaier, G. Sęk, A. Löffler, C. Hofmann, S. Kuhn, S. Reitzenstein, L. V. Keldysh, V. D. Kulakovskii, T. L. Reinecke, and A. Forchel. Strong coupling in a single quantum dot-semiconductor microcavity system. *Nature*, 432:197, 2004.
- [56] Q. A. Turchette, C. J. Hood, W. Lange, H. Mabuchi, and H. J. Kimble. Measurement of conditional phase shifts for quantum logic. *Physical Review Letters*, 75:4710, 1995.
- [57] I. Fushman, D. Englund, A. Faraon, N. Stoltz, P. Petroff, and J. Vuckovic. Controlled phase shifts with a single quantum dot. *Science*, 320:769, 2008.
- [58] J. Clarke and F. K. Wilhelm. Superconducting quantum bits. *Nature*, 453:1031, 2008.
- [59] M. Saffman, T. G. Walker, and K. Molmer. Quantum information with Rydberg atoms. *Review of Modern Physics*, 82:2313, 2010.
- [60] C. Barthel, D. J. Reilly, C. M. Marcus, M. P. Hanson, and A. C. Gossard. Rapid single-shot measurement of a singlet-triplet qubit. *Physical Review Letters*, 103:160503, 2009.
- [61] P. Kok, W. J. Munro, K. Nemoto, T. C. Ralph, J. P. Dowling, and G. J. Milburn. Linear optical quantum computing with photonic qubits. *Review of Modern Physics*, 79:135, 2007.

- [62] N. Imoto, H. A. Haus, and Y. Yamamoto. Quantum nondemolition measurement of the photon number via the optical kerr effect. *Physical Review A*, 32:2287, 1985.
- [63] J. C. Howell and J. A. Yeazell. Quantum computation through entangling single photons in multipath interferometers. *Physical Review Letters*, 85:198, 2000.
- [64] G. J. Milburn. Quantum optical Fredkin gate. *Physical Review Letters*, 62:2124, 1989.
- [65] I. L. Chuang and Y. Yamamoto. Simple quantum computer. *Physical Review A*, 52:3489, 1995.
- [66] H. Schmidt and A. Imamoglu. Giant Kerr nonlinearities obtained by electromagnetically induced transparency. *Optics Letters*, 21:1936, 1996.
- [67] S. E. Harris, J. E. Field, and A. Imamoglu. Nonlinear optical processes using electromagnetically induced transparency. *Physical Review Letters*, 64:1107, 1990.
- [68] A. Auffeves-Garnier, C. Simon, J. M. Gerard, and J. P. Poizat. Giant optical nonlinearity by a single two-level system interacting with a cavity in the Purcell regime. *Physical Review A*, 75:053823, 2007.
- [69] L. M. Duan and H. J. Kimble. Scalable photonic quantum computation through cavity-assisted interactions. *Physical Review Letters*, 92:127902, 2004.
- [70] H. F. Hofmann, K. Kojima, S. Takeuchi, and K. Sasaki. Optimized phase switching using a single-atom nonlinearity. *Journal of Optics B*, 5:218, 2003.
- [71] C. Bonato, F. Haupt, S. S. R. Oemrawsingh, J. Gudat, D. Ding, M. P. van Exter, and D. Bouwmeester. CNOT and Bell-state analysis in the weak-coupling cavity QED regime. *Physical Review Letters*, 104:160503, 2010.
- [72] W. Chen, K. M. Beck, V. Bucker, M. Gullans, M. D. Lukin, H. Tanjisuze, and V. Vuletic. All-optical switch and transistor gated by one stored photon. *Science*, 341:768, 2013.

- [73] T. Peyronel, O. Firstenberg, Q. Liang, S. Hofferberth, A. Gorshkov, T. Pohl, M. D. Lukin, and V. Vuletic. Quantum nonlinear optics with single photons enabled by strongly interacting atoms. *Nature*, 488:57, 2012.
- [74] D. Englund, D. Fattal, E. Waks, G. Solomon, B. Zhang, T. Nakaoka, Y. Arakawa, Y. Yamamoto, and J. Vuckovic. Controlling the spontaneous emission rate of single quantum dots in a two-dimensional photonic crystal. *Physical Review Letters*, 95:013904, 2005.
- [75] R. Bose, D. Sridharan, H. Kim, G. S. Solomon, and E. Waks. Low-photon-number optical switching with a single quantum dot coupled to a photonic crystal cavity. *Physical Review Letters*, 108:227402, 2012.
- [76] T. Volz, A. Reinhard, M. Winger, A. Badolato, K. J. Hennessy, E. L. Hu, and A. Imamoglu. Ultrafast all-optical switching by single photons. *Nature Photonics*, 6:605, 2012.
- [77] A. Reinhard, T. Volz, M. Winger, A. Badolato, K. J. Hennessy, E. L. Hu, and A. Imamoglu. Strongly correlated photons on a chip. *Nature Photonics*, 6:93, 2012.
- [78] D. Englund, A. Majumdar, M. Bajcsy, A. Faraon, P. Petroff, and J. Vuckovic. Ultrafast photon-photon interactions in a strongly coupled quantum dot-cavity system. *Physical Review Letters*, 108:093604, 2012.
- [79] E. Waks and J. Vuckovic. Dispersive properties and large Kerr nonlinearities using dipole-induced transparency in a single-sided cavity. *Physical Review A*, 73:041803(R), 2006.
- [80] E. Waks and J. Vuckovic. Dipole induced transparency in drop-filter cavity-waveguide systems. *Physical Review Letters*, 96:153601, 2006.
- [81] D. Valente, S. Portolan, G. Nogues, J. P. Poizat, M. Richard, J. M. Gerard, M. F. Santos, and A. Auffeves-Garnier. Monitoring stimulated emission at the single-photon level in one-dimensional atoms. *Physical Review A*, 85:023811, 2012.
- [82] D. Valente, Y. Li, J. P. Poizat, J. M. Gerard, L. C. Kwek, M. F. Santos, and A. Auffeves-Garnier. Optimal irreversible stimulated emission. *New Journal of Physics*, 14:083029, 2012.

- [83] D. Valente, Y. Li, J. P. Poizat, J. M. Gerard, L. C. Kwek, M. F. Santos, and A. Auffeves-Garnier. Universal optimal broadband photon cloning and entanglement creation in one-dimensional atoms. *Physical Review A*, 86:022333, 2012.
- [84] E. Rephaeli and S. Fan. Stimulated emission from a single excited atom in a waveguide. *Physical Review Letters*, 108:143602, 2012.
- [85] J. H. Shapiro. Single-photon Kerr nonlinearities do not help quantum computation. *Physical Review A*, 73:062305, 2006.
- [86] S. A. Campbell. *The science and engineering of microelectronic fabrication*. Oxford University Press, 2001.
- [87] Z. Cui. *Nanofabrication: Principles, Capabilities and Limits*. Springer, 2008.
- [88] S. Bellucci. *Self-Assembly of Nanostructures: The INFN Lectures, Vol. III: 3 (Lecture Notes in Nanoscale Science and Technology)*. Springer, 2012.
- [89] L. H. Li, N. Chauvin, G. Patriarche, B. Alloing, and A. Fiore. Growth-interruption-induced low-density InAs quantum dots on GaAs. *Journal of Applied Physics*, 104:083508, 2008.
- [90] Raith GmbH. *Raith NanoSuite Software Reference Manual 6.0*, 2010.
- [91] W. Ying, H. Weihua, Y. Xiang, Z. Renping, Z. Yang, and Y. Fuhua. An efficient dose compensation method for proximity effect correction. *Journal of Semiconductors*, 31:086001, 2010.
- [92] R. Wuest, P. Strasser, M. Jungo, F. Robin, D. Erni, and H. Jackel. An efficient proximity-effect correction method for electron-beam patterning of photonic crystal devices. *Microelectronic Engineering*, 67:182, 2003.
- [93] J. Leclercq, R. Ribas, J. Karam, and P. Viktorovitch. III-V micromachined devices for microsystems. *Microelectronics Journal*, 29:613, 1998.
- [94] M. A. Dundar, E. C. I. Ryckebosch, R. Notzel, F. Karouta, L. J. van Ijzen-doorn, and R. W. van der Heijden. Sensitivities of InGaAsP photonic crystal membrane nanocavities to hole refractive index. *Optics Express*, 18:4049, 2010.

- [95] ISA Jobin Yvon/Spex. *Guide for Spectroscopy*, 1994.
- [96] SCONTEL. *TCOPRS-001 Operation manual*, 2008.
- [97] M. Wahl. *Time-correlated single photon counting*. PicoQuant GmbH, 2009.
- [98] E. Knill, R. Laflamme, and G. J. Milburn. A scheme for efficient quantum computation with linear optics. *Nature*, 409:46, 2001.
- [99] M. Brune, F. Schmidt-kaler, A. Maali, J. Dreyer, E. Hagley, J. M. Raimond, and S. Haroche. Quantum rabi oscillation: A direct test of field quantization in a cavity. *Physical Review Letters*, 76:1800, 1996.
- [100] K. M. Birnbaum, A. Boca, I. Miller, D. Boozer, T. E. Northup, and H. J. Kimble. Photon blockade in an optical cavity with one trapped atom. *Nature*, 436:87, 2005.
- [101] R. J. Thompson, G. Rempe, and H. J. Kimble. Observation of normal-mode splitting for an atom in an optical cavity. *Physical Review Letters*, 68:1132, 1992.
- [102] A. Wallraff, D. I. Schuster, A. Blais, L. Frunzio, R. S. Huang, J. Majer, S. Kumar, S. M. Girvin, and R. J. Schoelkopf. Strong coupling of a single photon to a superconducting qubit using circuit quantum electrodynamics. *Nature*, 431:162, 2004.
- [103] K. Srinivasan and O. Painter. Linear and nonlinear optical spectroscopy of a strongly coupled microdisk-quantum dot system. *Nature*, 450:862, 2007.
- [104] S. M. Tan. A computational toolbox for quantum and atomic optics. *Journal of Optics B: Quantum and Semiclassical Optics*, 1:424, 1999.
- [105] E. Waks, C. Santori, and Y. Yamamoto. Security aspects of quantum key distribution with sub-poissonian light. *Physical Review A*, 66:042315, 2002.
- [106] D. Englund, A. Faraon, I. Fushman, N. Stoltz, P. Petroff, and J. Vuckovic. Controlling cavity reflectivity with a single quantum dot. *Nature*, 450:857, 2007.

- [107] A. Faraon, I. Fushman, D. Englund, N. Stoltz, P. Petroff, and J. Vuckovic. Coherent generation of non-classical light on a chip via photon-induced tunnelling and blockade. *Nature Physics*, 4:859, 2008.
- [108] V. Loo, C. Arnold, O. Gazzano, A. Lemaitre, I. Sagnes, O. Krebs, P. Voisin, P. Snellart, and L. Lanco. Optical nonlinearity for few-photon pulses on a quantum dot-pillar cavity device. *Physical Review Letters*, 109:166806, 2012.
- [109] G. Lindblad. On the generators of quantum dynamical semigroups. *Communications of Mathematical Physics*, 48:119, 1976.
- [110] A. Einstein. Zur quantentheorie der strahlung. *Physikalische Zeitschrift*, 18:121, 1917.
- [111] A. E. Siegman. *Lasers*. Mill Valley, CA: University Science Books, 1986.
- [112] J. Hwang, M. Pototschnig, R. Lettow, G. Zumofen, A. Renn, S. Gotzinger, and V. Sandoghdar. A single-molecule optical transistor. *Nature*, 460:76, 2009.
- [113] K. Kojima, H. F. Hofmann, S. Takeuchi, and K. Sasaki. Efficiencies for the single-mode operation of a quantum optical nonlinear shift gate. *Physical Review A*, 70:013810, 2004.
- [114] S. Fasel, N. Gisin, G. Ribordy, V. Scarani, and H. Zbinden. Quantum cloning with an optical fiber amplifier. *Physical Review Letters*, 89:107901, 2002.
- [115] C. Simon, G. Weihs, and A. Zeilinger. Optimal quantum cloning via stimulated emission. *Physical Review Letters*, 84:2993, 2000.
- [116] A. Lamas-Linares, J. C. Howell, and D. Bouwmeester. Stimulated emission of polarization-entangled photons. *Nature*, 412:887, 2001.
- [117] D. J. Bergman and M. I. Stockman. Surface plasmons amplified by stimulated emission of radiation: quantum generation of coherent surface plasmons in nanosystems. *Physical Review Letters*, 90:027402, 2003.
- [118] O. V. Astafiev, A. A. Abdumalikov, A. M. Zagoskin, Y. A. Pashkin, Y. Nakamura, and J. S. Tsai. Ultimate on-chip quantum amplifier. *Physical Review Letters*, 104:183603, 2010.

- [119] H. Benisty, C. Weisbuch, D. Labilloy, M. Rattier, C. J. M. Smith, T. F. Krauss, R. M. De La Rue, R. Houdre, U. Oesterle, C. Jouanin, and D. Cassagne. Optical and confinement properties of two-dimensional photonic crystals. *IEEE Journal of Lightwave Technology*, 17:2063, 1999.
- [120] M. Loncar, T. Doll, J. Vuckovic, and A. Scherer. Design and fabrication of silicon photonic crystal optical waveguides. *IEEE Journal of Lightwave Technology*, 18:1402, 2000.
- [121] S. G. Johnson, P. Bienstman, M. A. Skorobogatiy, M. Ibanescu, E. Lidorikis, and J. D. Joannopoulos. Adiabatic theorem and continuous coupled-mode theory for efficient taper transitions in photonic crystals. *Physical Review E*, 66:066608, 2002.
- [122] P. Bienstman, S. Assefa, S. G. Johnson, J. D. Joannopoulos, G. S. Petrich, and L. A. Kolodziejski. Taper structures for coupling into photonic crystal slab waveguides. *Journal of Optical Society of America B*, 20:1817, 2003.
- [123] M. Askari and A. Adibi. High efficiency coupling of light from a ridge to a photonic crystal waveguide. *Applied Optics*, 10:5803, 2013.
- [124] L. Rosa, S. Selleri, and F. Poli. Design of photonic-crystal and wire waveguide interface. *Journal of Lightwave Technology*, 23:2740, 2005.
- [125] C. Manolatou, M. J. Khan, S. Fan, P. R. Villeneuve, H. A. Haus, and J. D. Joannopoulos. Coupling of modes analysis of resonant channel add-drop filters. *IEEE Journal of Quantum Electronics*, 35:1322, 1999.
- [126] Y. Xu, Y. Li, R. K. Lee, and A. Yariv. Scattering-theory analysis of waveguide-resonator coupling. *Physical Review E*, 62:7389, 2000.
- [127] M. Notomi, A. Shinya, S. Mitsugi, E. Kuramochi, and H. Ryu. Waveguides, resonators and their coupled elements in photonic crystal slabs. *Optics Express*, 12:1551, 2004.
- [128] H. Takano, Y. Akahane, T. Asano, and S. Noda. In-plane-type channel drop filter in a two-dimensional photonic crystal slab. *Applied Physics Letters*, 84:2226, 2004.

- [129] J. Moosburger, M. Kamp, A. Forchel, U. Oesterle, and R. Houdre. Transmission spectroscopy of photonic crystal based waveguides with resonant cavities. *Journal of Applied Physics*, 91:4791, 2002.
- [130] A. R. A. Chalcraft, S. Lam, D. O'Brien, T. F. Krauss, M. Sahin, D. Szymanski, D. Sanvitto, R. Oulton, M. S. Skolnick, M. A. Fox, D. M. Whittaker, H. Y. Liu, and M. Hopkinson. Mode structure of the L3 photonic crystal cavity. *Applied Physics Letters*, 90:241117, 2007.
- [131] J. F. P. Schouwenberg. *Bachelor thesis*. Eindhoven University of Technology, 2012.
- [132] J. Salzman, R. J. Hawkins, C. E. Zah, S. Menocal, and T. P. Lee. The tilted waveguide semiconductor laser amplifier. *Journal of Applied Physics*, 64:2240, 1988.
- [133] D. Marcuse. Reflection loss of laser mode from tilted end mirror. *IEEE Journal of Lightwave Technology*, 7:336, 1989.
- [134] J. Salzman, R. J. Hawkins, and T. P. Lee. Modal coupling in tilted-mirror waveguide lasers and amplifiers. *Optics Letters*, 13:455, 1988.
- [135] E. Hecht. *Optics*. Addison Wesley, 1997.
- [136] B. E. A. Saleh and M. C. Teich. *Fundamentals of Photonics*. John Wiley & Sons, Inc., 2007.
- [137] D. Taillaert, W. Bogaerts, P. Bienstman, T. F. Krauss, P. Van Daele, I. Moerman, S. Verstuyft, K. De Mesel, and R. Baets. An out-of-plane grating coupler for efficient butt-coupling between compact planar waveguides and single-mode fibers. *IEEE Journal of Quantum Electronics*, 38:949, 2002.
- [138] N. Eriksson, M. Hagberg, and A. Larsson. Highly directional grating outcouplers with tailorable radiation characteristics. *IEEE Journal of Quantum Electronics*, 32:1038, 1996.
- [139] W. Kuang, C. Kim, A. Stapleton, and J. D. O'Brien. Grating-assisted coupling of optical fibers and photonic crystal waveguides. *Optics Letters*, 27:1604, 2002.

- [140] S. Hughes, L. Ramunno, J. F. Young, and J. E. Sipe. Extrinsic optical scattering loss in photonic crystal waveguides: Role of fabrication disorder and photon group velocity. *Physical Review Letters*, 94:033903, 2005.
- [141] E. Kuramochi, M. Notomi, S. Hughes, A. Shinya, T. Watanabe, and L. Ramunno. Disorder-induced scattering loss of line-defect waveguides in photonic crystal slabs. *Physical Review B*, 72:161318, 2005.
- [142] S. Fattah poor, T. B. Hoang, L. Midolo, C. P. Dietrich, L. H. Li, E. H. Linfield, J. F. P. Schouwenberg, T. Xia, F. M. Pagliano, F. W. M. van Otten, and A. Fiore. Efficient coupling of single photons to ridge-waveguide photonic integrated circuits. *Applied Physics Letters*, 102:131105, 2013.
- [143] A. Badolato, K. Hennessy, M. Atature, J. Dreiser, P. M. Petroff, and A. Imamoglu. Deterministic coupling of single quantum dots to single nanocavity modes. *Science*, 308:1158, 2005.
- [144] L. Balet, M. Francardi, A. Gerardino, N. Chauvin, B. Alloing, C. Zinoni, C. Monat, L. H. Li, N. Le Thomas, R. Houdre, and A. Fiore. Enhanced spontaneous emission rate from single InAs quantum dots in a photonic crystal nanocavity at telecom wavelengths. *Applied Physics Letters*, 91:123115, 2007.
- [145] V. S. Rao and S. Hughes. Single quantum dot spontaneous emission in a finite-size photonic crystal waveguide: Proposal for an efficient "on chip" single photon gun. *Physical Review Letters*, 99:193901, 2007.
- [146] T. Lund-Hansen, S. Stobbe, B. Julsgaard, H. Thyrrestrup, T. Sunner, M. Kamp, A. Forchel, and P. Lodahl. Experimental realization of highly efficient broadband coupling of single quantum dots to a photonic crystal waveguide. *Physical Review Letters*, 101:113903, 2008.
- [147] T. B. Hoang, J. Beetz, L. Midolo, M. Skacel, M. Lermer, M. Kamp, S. Höfling, L. Balet, N. Chauvin, and A. Fiore. Enhanced spontaneous emission from quantum dots in short photonic crystal waveguides. *Applied Physics Letters*, 100:061122, 2012.
- [148] A. Enderlin, Y. Ota, R. Ohta, N. Kumagi, S. Ishida, S. Iwamoto, and Y. Arakawa. High guided mode-cavity mode coupling for an efficient extraction of spontaneous emission of a single quantum dot embedded in a photonic crystal nanobeam cavity. *Physical Review B*, 86:075314, 2012.

- [149] L. Midolo, F. Pagliano, T. B. Hoang, T. Xia, F. W. M. van Otten, L. H. Li, E. H. Linfield, M. Lerner, S. Höfling, and A. Fiore. Spontaneous emission control of single quantum dots by electromechanical tuning of a photonic crystal cavity. *Applied Physics Letters*, 101:091106, 2012.
- [150] R. B. Patel, A. J. Bennett, I. Farrer, C. A. Nicoll, and A. J. Shields. Two-photon interference of the emission from electrically tunable remote quantum dots. *Nature Photonics*, 4:632, 2010.
- [151] I. Hiroaki, K. Hiruma, K. Ishida, T. Asai, and H. Matsumura. Low loss GaAs optical waveguides. *IEEE Transactions on Electron Devices*, 32:2226, 1985.
- [152] C. Baker, C. Belacel, A. Andronic, P. Snellart, A. Lemaitre, E. Galopin, S. Ducci, G. Leo, and I. Favero. Critical optical coupling between a GaAs disk and a nanowaveguide suspended on the chip. *Applied Physics Letters*, 99:151117, 2011.
- [153] A. Talneau, K. H. Lee, S. Guilet, and I. Sagnes. Efficient coupling to W1 photonic crystal waveguide on InP membrane through suspended access guides. *Applied Physics Letters*, 92:061105, 2008.
- [154] M. G. Banaee, A. G. Pattantyus-Abraham, M. W. McCutcheon, G. W. Rieger, and J. Y. Young. Efficient coupling of photonic crystal micro-cavity modes to a ridge waveguide. *Applied Physics Letters*, 90:193106, 2007.
- [155] A. De Rossi, V. Ortiz, M. Calligaro, L. Lanco, S. Ducci, V. Berger, and I. Sagnes. Measuring propagation loss in a multimode semiconductor waveguide. *Journal of Applied Physics*, 97:073105, 2005.
- [156] N. Chauvin, C. Zinoni, M. Francardi, A. Gerardino, L. Balet, B. Alloing, L. H. Li, and A. Fiore. Controlling the charge environment of single quantum dots in a photonic-crystal cavity. *Physical Review B*, 80:241306(R), 2009.
- [157] M. Winger, T. Volz, G. Tarel, S. Portolan, A. Badolato, K. J. Hennessy, E. L. Hu, A. Beveratos, J. J. Finley, V. Savona, and A. Imamoglu. Explanation of photon correlations in the far-off-resonance optical emission from a quantum dot-cavity system. *Physical Review Letters*, 103:207403, 2009.

- [158] C. Zinoni, B. Alloing, C. Monat, V. Zwiller, L. H. Li, A. Fiore, L. Lunghi, A. Gerardino, H. de Riedmatten, H. Zbinden, and N. Gisin. Time-resolved and antibunching experiments on single quantum dots at 1300 nm. *Applied Physics Letters*, 88:131102, 2006.
- [159] B. R. Mollow. Power spectrum of light scattered by two-level systems. *Physical Review*, 188:1969, 1969.
- [160] H. J. Kimble and L. Mandel. Theory of resonance fluorescence. *Physical Review A*, 13:2123, 1976.
- [161] H. J. Kimble, M. Dagenais, and L. Mandel. Photon antibunching in resonance fluorescence. *Physical Review Letters*, 39:691, 1977.
- [162] E. B. Flagg, A. Muller, J. W. Robertson, S. Founta, D. G. Deppe, M. Xiao, W. Ma, G. J. Salamo, and C. K. Shih. Resonantly driven coherent oscillations in a solid-state quantum emitter. *Nature Physics*, 5:203, 2009.
- [163] O. Astafiev, A. M. Zagoskin, A. A. Abdumalikov, Y. A. Pashkin, T. Yamamoto, K. Inomata, Y. Nakamura, and J. S. Tsai. Resonance fluorescence of a single artificial atom. *Science*, 327:840, 2010.
- [164] W. Heitler. *The quantum theory of radiation*. Clarendon Press, Oxford, 1954.
- [165] J. T. Hoffges, H. W. Baldauf, T. Eichler, S. R. Helmfrid, and H. Walther. Heterodyne measurement of the fluorescent radiation of a single trapped ion. *Optics Communications*, 133:170, 1997.
- [166] C. Matthiesen, A. N. Vamivakas, and M. Atatüre. Subnatural linewidth single photons from a quantum dot. *Physical Review Letters*, 108:093602, 2012.
- [167] Y-M. He, Y. He, Y-J. Wei, D. Wu, M. Atatüre, C. Schneider, S. Höfling, M. Kamp, C-Y. Lu, and J-W. Pan. On-demand semiconductor single-photon source with near-unity indistinguishability. *Nature Nanotechnology*, 8:213, 2013.
- [168] H. Kamada, H. Gotoh, J. Temmyo, T. Takagahara, and H. Ando. Exciton rabi oscillation in a single quantum dot. *Physical Review Letters*, 87:246401, 2001.

- [169] T. H. Stievater, X. Li, D. G. Steel, D. Gammon, D. S. Katzer, D. Park, C. Piermarocchi, and L. J. Sham. Rabi oscillations of excitons in single quantum dots. *Physical Review Letters*, 87:133603, 2001.
- [170] H. Htoon, T. Takagahara, D. Kulik, O. Baklenov, A. L. Holmes, and C. K. Shih. Interplay of rabi oscillations and quantum interference in semiconductor quantum dots. *Physical Review Letters*, 88:087401, 2002.
- [171] A. Zrenner, E. Beham, S. Stuffer, F. Findeis, M. Bichler, and G. Abstreiter. Coherent properties of a two-level system based on a quantum-dot photodiode. *Nature*, 418:612, 2002.
- [172] T. Yoshie, A. Scherer, J. Hendrickson, G. Khitrova, H. M. Gibbs, G. Rupper, C. Ell, O. B. Shchekin, and D. G. Deppe. Vacuum rabi splitting with a single quantum dot in a photonic crystal nanocavity. *Nature*, 432:200, 2004.
- [173] P. Michler, A. Kiraz, C. Becher, W. V. Schoenfeld, P. M. Petroff, L. Zhang, E. Hu, and A. Imamoglu. A quantum dot single-photon turnstile device. *Science*, 290:2282, 2000.
- [174] C. Santori, D. Fattal, J. Vuckovic, G. S. Solomon, and Y. Yamamoto. Indistinguishable photons from a single-photon device. *Nature*, 419:594, 2002.
- [175] S. Ates, S. M. Ulrich, S. Reitzenstein, A. Löffler, A. Forchel, and P. Michler. Post-selected indistinguishable photons from the resonance fluorescence of a single quantum dot in a microcavity. *Physical Review Letters*, 103:167402, 2009.
- [176] N. Akopian, N. H. Lindner, E. Poem, Y. Berlatzky, J. Avron, D. Gershoni, B. D. Gerardot, and P. M. Petroff. Entangled photon pairs from semiconductor quantum dots. *Physical Review Letters*, 96:130501, 2006.
- [177] R. M. Stevenson, R. J. Young, P. Atkinson, K. Cooper, D. A. Ritchie, and A. J. Shields. A semiconductor source of triggered entangled photon pairs. *Nature*, 439:179, 2006.
- [178] A. Hoge, S. Seidl, M. Kroner, K. Karrai, R. Warburton, B. D. Gerardot, and P. M. Petroff. Voltage-controlled optics of a quantum dot. *Physical Review Letters*, 93:217401, 2004.

- [179] P. Borri, W. Langbein, S. Schneider, U. Woggon, R. L. Sellin, D. Ouyang, and D. Bimberg. Ultralong dephasing time in InGaAs quantum dots. *Physical Review Letters*, 87:157401, 2001.
- [180] T. Unold, K. Mueller, C. Lienau, T. Elsaesser, and A. D. Wieck. Optical stark effect in a quantum dot: ultrafast control of single exciton polarizations. *Physical Review Letters*, 92:157401, 2004.
- [181] A. Muller, E. B. Flagg, P. Bianucci, X. Y. Wang, D. G. Deppe, W. Ma, J. Zhang, G. J. Salamo, M. Xiao, and C. K. Shih. Resonance fluorescence from a coherently driven semiconductor quantum dot in a cavity. *Physical Review Letters*, 99:187402, 2007.
- [182] J. W. Robertson, S. Founta, M. Hughes, M. Hopkinson, A. J. Ramsay, M. S. Skolnick, and Shih. Polarization-resolved resonant fluorescence of a single semiconductor quantum dot. *Applied Physics Letters*, 101:251118, 2012.
- [183] A. N. Vamivakas, Y. Zhao, C. Lu, and M. Atature. Spin-resolved quantum-dot resonance fluorescence. *Nature Physics*, 5:925, 2009.
- [184] H. S. Nguyen, G. Sallen, C. Voisin, P. Roussignol, C. Diederichs, and G. Cassaboïs. Ultra-coherent single photon source. *Applied Physics Letters*, 99:261904, 2011.
- [185] E. Rosencher and B. Vinter. *Optoelectronics*. Cambridge University Press, 2004.
- [186] G. Bastard. *Wave mechanics applied to semiconductor heterostructures*. les eclitions de physique, 1992.
- [187] J. J. Sakurai. *Modern quantum mechanics*. Addison Wesley, 1993.
- [188] H. S. Nguyen, G. Sallen, C. Voisin, P. Roussignol, C. Diederichs, and G. Cassaboïs. Optically gated resonant emission of single quantum dots. *Physical Review Letters*, 108:057401, 2012.
- [189] A. Majumdar, A. Faraon, E. D. Kim, D. Englund, H. Kim, P. M. Petroff, and J. Vuckovic. Linewidth broadening of a quantum dot coupled to an off-resonant cavity. *Physical Review B*, 82:045306, 2010.

- [190] A. Majumdar, E. D. Kim, and J. Vuckovic. Effect of photogenerated carriers on the spectral diffusion of a quantum dot coupled to a photonic crystal cavity. *Physical Review B*, 84:195304, 2011.
- [191] H. Kamada and T. Kutsuwa. Broadening of single quantum dot exciton luminescence spectra due to interaction with randomly fluctuating environmental charges. *Physical Review B*, 78:155324, 2008.
- [192] M. Burresi, R. J. P. Engelen, A. Opheij, D. van Oosten, D. Mori, T. Baba, and L. Kuipers. Observation of polarization singularities at the nanoscale. *Physical Review Letters*, 102:033902, 2009.
- [193] S. J. Dewhurst, D. Granados, D. J. P. Ellis, A. J. Bennett, R. B. Patel, I. Farrer, D. Anderson, G. A. C. Jones, D. A. Ritchie, and A. J. Shields. Slow-light-enhanced single quantum dot emission in a unidirectional photonic crystal waveguide. *Applied Physics Letters*, 96:031109, 2010.
- [194] W. B. Gao, P. Fallahi, E. Togan, J. Miguel-Sanchez, and A. Imamoglu. Observation of entanglement between a quantum dot spin and a single photon. *Nature*, 491:426, 2012.
- [195] K. De Greve, L. Yu, P. L. McMahon, J. S. Pelc, C. M. Natarajan, N. Y. Kim, E. Abe, S. Maier, C. Schneider, M. Kamp, S. Höfling, R. H. Hadfield, A. Forchel, M. M. Fejer, and Y. Yamamoto. Quantum-dot spin-photon entanglement via frequency downconversion to telecom wavelength. *Nature*, 491:421, 2012.
- [196] M. Christandl, N. Datta, A. Ekert, and J. Landahl. Perfect state transfer in quantum spin networks. *Physical Review Letters*, 92:187902, 2004.

Investigation of Single-Photon Emission from Quantum Dots in Semiconductor Waveguides under Non-resonant and Resonant Excitation

Single photons are one of the most promising candidates for applications in quantum information and computation. The possibility of integration inside a semiconductor integrated circuit has made semiconductor quantum dots (QDs) a suitable candidate for use as a single-photon source inside a quantum photonic integrated circuit. In this thesis several experimental steps toward the extraction of the single-photon emission of QDs integrated inside semiconductor waveguides have been demonstrated.

In chapter 1, the main applications of photons for quantum information processing, including the concept of quantum photonic integrated circuit, are reviewed. Semiconductor QDs and photonic crystals (PhCs) (as an environment for controlling the emission of QDs) are introduced. Finally, after a short introduction to cavity quantum electrodynamics, the state-of-the-art of using single-photon nonlinearities for quantum information purposes are reviewed.

In chapter 2, the experimental methods used during the course of this work are introduced. The equipment and recipes used for fabricating PhCs, ridge waveguides (RWGs) and coupled RWG-PhC systems are discussed. In the second part of the chapter the optical setups used for optical measurements are introduced.

In chapter 3, the two single-photon nonlinear phenomena of dipole-induced reflection and single-photon stimulated emission are investigated based on a

Master equation approach and the possible experimental configurations for observing them in our system are discussed.

Chapter 4 describes the designs and structures used to couple light efficiently to and from a photonic crystal. These include the design for efficient coupling of light from a photonic crystal waveguide (PhCWG) to a RWG. By using an adiabatic tapering a theoretical transmission of 98% has been obtained. Next, an in-line L3 cavity used as an on-chip filter has been realized and filtering of single QD lines has been demonstrated. To suppress Fabry-Perot oscillations generated by reflections of light at the two cleaved facets of a RWG, a thin layer of SiN has been deposited as an antireflection coating and the reduction of the fringe contrast has been experimentally observed. Finally, circular grating couplers for coupling light from the top into a PhCWG have been realized and coupling efficiencies around 1% from the center of PhCWG to the top collection fiber (via an objective) have been achieved.

Chapter 5 includes the demonstration of efficient coupling of single photon into RWGs. By using the tapering design in chapter 4, transmission values around 70% between RWG and PhCWG and single-photon funnelling rates around 3.5 MHz from a PhCC into a RWG have been demonstrated. In the last section of the chapter the feasibility of the dipole-induced reflection measurements in our system is discussed and it is shown that with the current QDs the observation of this phenomenon is very improbable.

Chapter 6 introduces the novel combined k-vector and polarization filtering method that has been proposed during this work for extraction of resonance fluorescence of QDs inside a RWG. It has been shown that by this method the scattering of the resonant laser driving QDs can be suppressed and the resonant emission of the QDs can be extracted. By changing the power of the resonant driving laser the peak emission intensity and the linewidth of QDs have been measured and fitted with a model based on optical Bloch equations for a two level system.

Finally, in chapter 7 the main results obtained in this thesis are summarised and future directions for research activities based on these results are proposed.

Acknowledgements

Completion of the work presented in this thesis would have not been possible without the contributions of many other people who kindly provided me their support. In the next few lines I wish to express my gratitude for their helps.

First I want to thank my first promoter and daily supervisor prof.dr. Andrea Fiore for providing me the opportunity of doing a PhD and getting acquainted with the ups and downs of doing scientific research and his availability during my PhD time.

I also wish to express my gratitude to prof.dr.ir. Meint Smit for being my second promoter and providing valuable advise about my thesis work. I would also like to thank the members of my defence committee: prof.dr. Martin Kamp, dr. Grzegorz Şek, dr. Jos van der Tol and prof.dr. Jaime Gómez-Rivas for evaluating my thesis and providing valuable feedback.

I thank the scientific staff of the PSN group for their inspirations and interesting discussions: prof.dr. Paul Koenrad, prof.dr. Erik Bakkers, dr. Jos Haverkort, dr. Andrei Silov and dr. Rob van der Heijden.

The help of dr. Lianhe Li and prof.dr. Edmund Linfield from the university of Leeds in the growth of quantum dots was indispensable for achieving the results in this thesis. I also want to thank our growth experts in the group for providing me samples: Yongjin, Frank and Tian.

I want to thank technicians of PSN group for their support: Jos van Ruijven, Rene van Veldhoven, Rian Hamhuijs, Martine van Vlokhoven, Peter Nouwens and Jos Bremmers for providing helium. A special thanks to the nanolab@TU/e management and technicians: Huub Ambrosius, Erik Jan Geluk, Jeroen Bolk,

Barry Smalbrugge, Beatriz Barcones Campo and Tjibbe de Vries. I appreciate the help from Tjibbe for the realization of antireflection coatings and interesting chats during the Borrel.

I would also like to thank the academic staff and members of PhI group with whom I had nice discussions: Dima (special thanks for your help with RWG mask design), Josselin, Saeed, Rui, Yuqing, Shahram, Hadi, Srivathsa and Emil. Special thanks to dr. Xaveer Leijtens for fruitful discussions and providing the C++ mask design code.

I like to thank the secretaries of PSN group in the past: Margriet and Annebee and present: Thérèse-Ann and Simone for their valuable help and support during my PhD.

Many thanks to the past and present members of the PSN group for the nice times we had during these years: Mehmet, Bowen, Murat, Adam, Joost, Juanita, Erwin, Steven, Sebastian, Diana, Ikaros, Simone, Anthony, Jia, Thuy, Salman, Yingchao, Alessandro, Davide, Rianne, Ang, Luca, Milo and Christian.

I want to thank the present and past members of single-photon subgroup of PSN and wish them success for the rest of their careers: Zili, Dondu, Tian, Zarko, Michele, Giulia, Maurangelo, Sybren, Ivan, Koen, Arjan and Saeedeh. During my PhD project I had the chance to work with Jeroen, who did his bachelor thesis in our group. I wish him the best for his future.

I wish to thank the following colleagues and friends for their great help during my time at the work and outside of the work: Thang (Master Thang) for being a good friend and teacher and a source of help inside the lab. Matthias for numerous interesting discussions about different topics and excursions to places with Iranian restaurant! Giulia (another one) and Enrico for nice times we had together. Francesco for being always helpful and available. Robert for a lot of interesting discussions about quantum physics and insights he gave me during my research. He is always helpful and full of nice ideas! Christof for his helps and friendship. Chaoyuan for always being available to provide help and insight. Ilaria and Leonhard for providing their valuable help and support. Leonardo for numerous helps he provided me inside the cleanroom and with numerical simulations and outside the work together with Katia for pleasant times we spent together.

Finally I wish to express my deepest gratitude toward my family. I thank my lovely siblings for providing me their support. I want to specially thank my parents for all the sacrifices they made for me during my life. Thank you for teaching me the meaning of working hard and having hope in every situation.

And last but not least I want to deeply thank my girlfriend Rosalinda for

providing encouragement and constructive opinion in every tough situation. Your love and support helped me to pass the difficult part of my PhD. Grazie infinite!

List of Publications

Journal publications:

S. Fattah poor, T. B. Hoang, L. Midolo, C. P. Dietrich, L. H. Li, E. H. Linfield, J. F. P. Schouwenberg, T. Xia, F. Pagliano, F. W. M. van Otten, and A. Fiore, Efficient coupling of single photons to ridge-waveguide photonic integrated circuits, *Appl. Phys. Lett.*, 102, 131105, (2013).

M. Skacel, F. Pagliano, T. B. Hoang, L. Midolo, S. Fattah poor, L. H. Li, E. H. Linfield, and A. Fiore, Low temperature scanning near-field optical microscopy of quantum dots in photonic crystals, *Phys. Rev. B.*, 88, 035416, (2013).

S. Fattah poor, I. Agafonov, F. M. Pagliano, C. P. Dietrich, L. H. Li, E. H. Linfield and A. Fiore, Observation of the resonance fluorescence from single quantum dots inside a ridge-waveguide, Under preparation, (2014).

Conference presentations:

Funneling single photons into ridge-waveguide photonic integrated circuits. SPIE Photonics West, San Francisco CA, USA, IN Proceedings of SPIE , 8632028 PP., (2013).

Funneling single photons into ridge-waveguide photonic integrated circuits.

Poster presentation- Physics@FOM, Veldhoven, The Netherlands (2013).

Curriculum Vitae

Sartoon Fattah poor was born on 31-05-1982 in Sanandaj, Iran. He obtained the high school diploma from the high school of National Organization for Development of Exceptional Talents in Rasht, Iran. He received a bachelor degree in applied physics from Sharif University of Technology in Tehran, Iran and in 2007 he was accepted for Master program in nanoscale science and technology in the department of microtechnology and nanoscience in Chalmers University of Technology, Gothenburg, Sweden, where he received his master degree in applied physics in 2009. From 2010 to 2014 he worked toward a PhD degree in applied physics in the group of Photonics and Semiconductor Nanophysics (PSN), Eindhoven University of Technology, the Netherlands. The result of this work has been published in this thesis.